Fabrication of Plasmon Enhanced Amorphous Silicon Solar Cells Using RF Magnetron Sputtering

Sandile Kumalo

A Dissertation submitted to the Faculty of Science,University of
the Witwatersrand, Johannesburg, in fulfilment of the
requirements for the degree of Masters of Science.
May 2019

Declaration

I, Sandile Kumalo (545710), declare that this dissertation titled, ”Fabrication of Plasmon Enhanced Amorphous Silicon Solar Cells Using RF Magnetron Sputtering” and the work presented in it are my own work. The work was done mainly in candidature for an MSc degree at the University of the Witwatersrand. I confirm that this work has not been submitted at the University of the Witwatersrand or any other institution. I have consulted with the work of others, also quoted their work and all the sources of help have been acknowledged with complete references.

Name: Sandile Kumalo

Signed:

Date:

Place: University of the Witwatersrand

Acknowledgement

I would like to take this opportunity to express my gratitude to those who have aided me with different aspects of conducting this research and writing of the dissertation.

First and foremost, my supervisors, Prof. Alexander Quandt and Prof. Daniel Wamwangi for their guidance and their constant support in this project, also helping me with the writing of this dissertation. The discussions I had with them regarding the project were really helpful and also encouraged me to carry out this work. Special thanks to Center of Excellence for Strong Materials (CoE-SM) for their generous funding that enabled me to do this work and for also paying my fees. To iThemba LABS and Anthony Miller for providing the infrastructure which helped me with the implantation. Appreciation also goes to the School of Physics, Microscopy and Microanalysis Unit (MMU) and Wits University for giving me this wonderful opportunity to do my research by providing facilities and resources.

I would also like to thank Miss Nhluvuko Mayimele and Dr. Francis Otieno for helping me in the lab by introducing me to some of the lab equipment and analysis. To the group, led by Prof. Alexander Quandt for the helpful group critics and discussions. More specially to Dr. Robert Warmbier and Materials for Energy Research Group (MERG). Finally, I would like to thank my family, Jonathan Cook, Tshene Wedi and the Wilkins family, Niall, Ilana, Max and Ivy for their support.

Dedication

This dissertation is dedicated to the late Bafana ”Scara” Mazibuko, my late grandmother, Thembi Eva Kumalo and my mother, Constance Jabulisile Kumalo.

Abstract

Renewable energy continues to attract intensive interest as a possible alternative to fossil fuel based energy sources due to its merits which are abundance, clean and geographically unlimited natural resources. The increased concerns of the harmful effects to the environment by fossil fuels has prompted a massive drive for photovoltaic based energy solutions. The current available solar technologies, thin film solar cells, have the potential of reducing production costs. However, the low photo conversion efficiency slows their rapid integration into the energy mix. In this work, we explore sophisticated light management strategies of silicon based thin film solar cells to enhance their photo conversion efficiency. These strategies ensure the enhancement of absorption of the complete solar spectrum, also reduced materials costs and a strongly reduced emission of greenhouse gases. The work involved fabricating and designing three significant layers of a hydrogenated amorphous silicon (a-Si:H) solar cell device, and integrating plasmonic nanoparticles in the commercial a-Si device to enhance optical absorption through Surface Plasmon Resonance (SPR). The project also involved several strategies to increase the conversion efficiency of a commercial a-Si standard device for comparative studies.

Recent approaches in the improvement of light absorption in solar cells were due to the use of plasmonic nanoparticles. It is well known theoretically as well as experimentally that metallic nanostructures have a strong interaction with light. This interaction allows remarkable control of the trapping and propagation of the photons in the intrinsic layer of thin film devices. For such a plasmon enhanced device to be economically viable and commercialised, the nanoparticles must be silver (Ag) and gold (Au), and the method used for the deposition must be carried out at temperatures lower than the ones used for the fabrication of a-Si:H layers.

Thus the RF magnetron sputtering technique in combination with ion implantation of each a-Si layers to form n and p-type a-Si was used to fabricate the three layers of an a-Si:H device. The architecture of the device is in a n-i-p or p-i-n sequence of doped semiconductor layers and each layer is fabricated using sputtering. Then Ag and Au nanoparticles were integrated into the commercial a-Si reference device. The devices are characterized for power conversion efficiency and I-V characteristics.

Contents

List of Figures

List of Tables

Chapter 1

1 Introduction

1.1 Renewable Energy Roadmap

The need for energy is increasing because of the ever growing human population and the demands unleashed by the world economy. This pressure on the energy supply is likely to be felt in the rapid developing economies, the key of which lie in sub-saharan Africa, Asia and South America. This means that fossil fuels are bound to run out because of the demands of producing energy[1]. The projected growth in the demand of world energy is continuously rising at a near exponential rate as depicted by Figure 1.1. Among the energy options available, fossil fuel based alternatives have over the years been heavily utilized. The enormous pressure on these sources is bound to drive them to depletion. Besides their exigent negative consequences and effects on the environment continues to spur the drive for alternative non fossil fuel based energy resources.

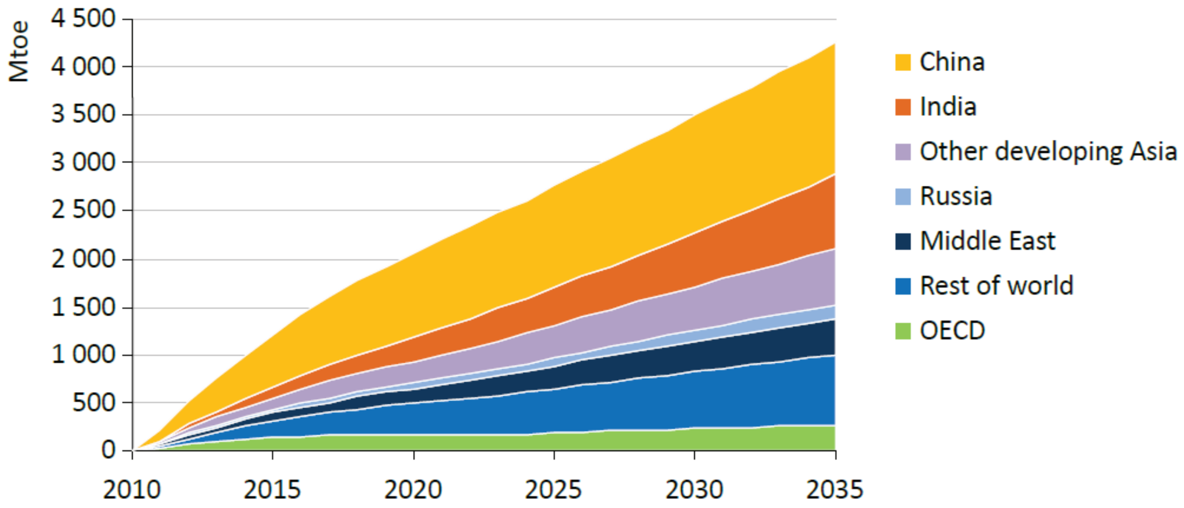

Figure 1.1: An image showing growth in the world energy demands. The image shows the increasing one million tonne of oil equivalent (Mtoe) with the increasing number of years [2]

.

Coupled to the high demand is the associated high production costs for energy generation. The fossil fuels are found only in certain countries, and this has led to other alternatives of energy like hydroelectric, biomass , wind, geothermal and solar[3]. Solar energy is expected to rise by 30% in the next 25 years, making it the second fastest growing renewable energy source compared to wind energy, as shown by Figure 1.2. Most of the energy that is used today is often produced in certain regions of the world, transported over a thousand kilometers and it is imported at great peril[4]. Renewable energy is one of the safest, cheapest and practically unlimited energy solution that can be used[5]. One of the cheapest, affordable and environmentally friendly way to solve the energy crisis around the world for now and in the future is to use the energy from the sun. This is done by converting solar energy into electrical energy.

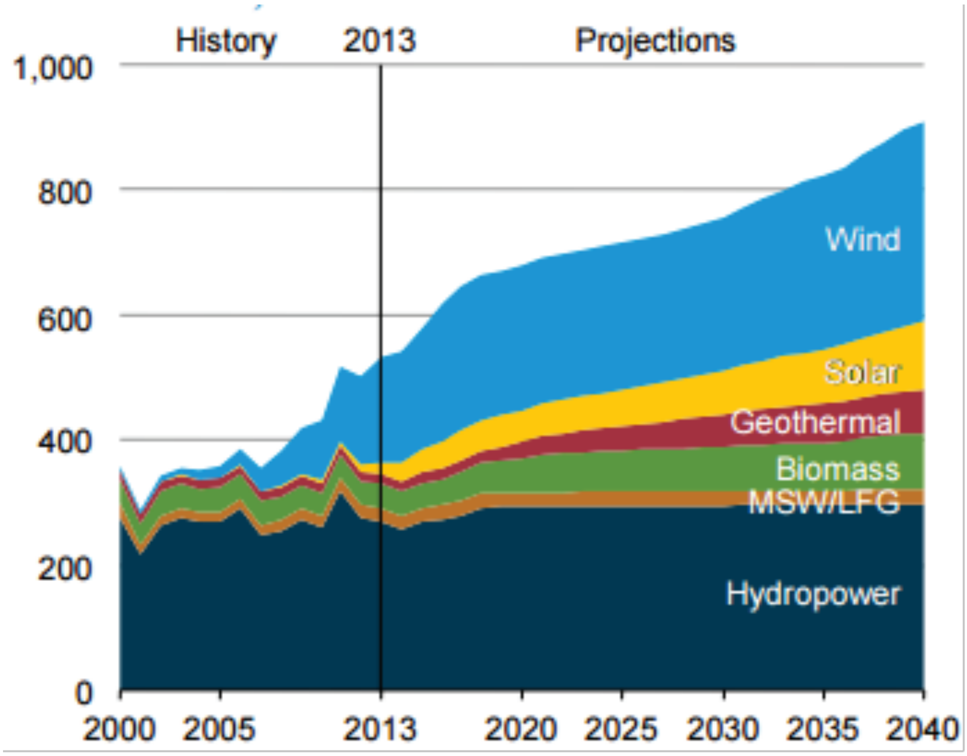

Figure 1.2: An image showing the projected growth in solar energy as an alternative source of energy compared to other renewable energy sources.[6]

Solar cells also known as Photovoltaics (PV) cells are the building blocks of solar modules. These modules are put together to larger units known as solar panels. Photovoltaics cells are devices that absorb sunlight and convert it into electricity. The device can be considered as a form of photoelectric cell, whose electrical characteristics such as current, resistance and voltage vary when exposed to sunlight. The difference between solar cells and battery cells is that the cells in solar panels are made to generate electricity by capturing sunlight and the battery cells generate electricity from chemical reactions[7].

At the moment, a fascinating approach of designing photovoltaic devices is established by the fabrication of the amorphous silicon (a-Si) solar cells in thin film format (nanometer thickness) onto a given substrate[8]. The rationale for using Si in solar cells are[9, 10, 11, 12, 13, 14, 15]:

- Si is the second most abundant element on the earth's crust.
- Si is the most common semiconductor material.
- Si PV plants are capable of reaching tera watts (TW) scales.
- Si is non-toxic.
- Si has a passivating oxide layer.
- Si has a low surface recombination rate.
- Si has an effective diffusion barrier for metal contacts, such as silver.

- The Si wafer technology is established because it has been applied in other areas of industry.

- The hydrated variant a-Si:H has a direct band gap ($\sim$1.7 $-$ 1.8 eV) with high absorption coefficient.

The thin film technology is based on the use of hydrogenated amorphous silicon (a-Si:H)[16] which grants a large reduction in semiconductor thickness due to its capacity to absorb approximately 100 times more light than crystalline silicon in the visible part of the solar spectrum[17]. This means that 1 μm thick a-Si:H is able to absorb 90% of the solar energy. Additionally, the thin film solar cell technology provides immense potential in cost reduction. This is based on the easiness to manufacture vigorous, enormous and rigid modules[18]. Nonetheless, because of the low conversion efficiency of a-Si:H thin film solar cells compared to regular wafer-based silicon devices, there is a lot of current research going into the enhancement of photo-conversion efficiency of all thin film solar cells, especially a-Si:H solar cells.

1.2 Solar Energy Abundance

The sun is the most important source of energy, which is able to support energy demands that are at a scale of (Terawatts) TW. The power radiated by the sun per unit area is 6.25×10^7 W/m^2 and the average power arriving at the surface of the earth's outer atmosphere is 1366 W/m^2[19]. Solar energy has the potential to cover the world's energy consumption, provided that the efficiency is higher than 70% [20, 21]. The human energy use around the world is approximated to be at 4×10^{14} $kWh/year$, which is an average power of 50 TW. The solar resource power on the earth's surface is at an average of 1.7×10^5 TW (1.5×10^{18} $kWh/year$). The amount of solar energy available that can be accessed is 5.5×10^{17} $kWh/year$ (3.6×10^4 TW_{ave}) and it is greater than the amount for the wind energy resource base, which is at 6×10^{14} $kWh/year$ (72 TW_{ave})[22, 19].

The energy from the sun is reduced as it approaches the earth's surface, because some of it is absorbed and reflected by atmospheric gases and water as shown in Figure 1.3. Despite these losses, the solar emission spectrum depicted by Figure 1.4 provides sufficient energy to power the world. The solar emission spectrum covers the ultraviolet, visible and infrared regions of the electromagnetic spectrum. The irradiance of the sun's energy is greatest at visible wavelengths, 300 - 800 nm, whereas the absorption of sunlight by water and atmospheric gases mainly occurs in the infrared region[24].

Solar energy already dominates the renewable energy sector when compared to other alternative sources of energy, such as wind, hydropower, geothermal and biomass combined. It also exceeds the known reserves of fossil fuels worldwide, including oil, unconventional shale gas and methane[26].

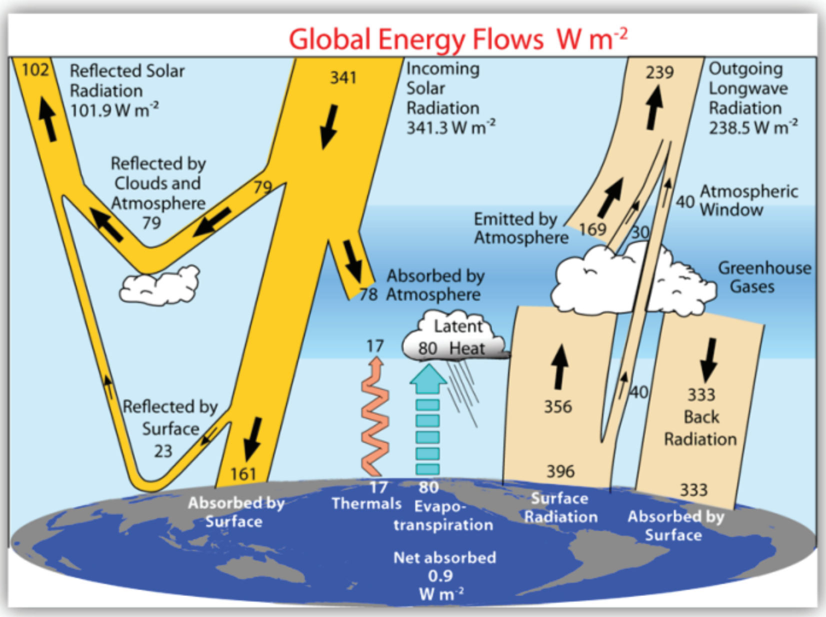

Figure 1.3: An image showing the schematic flow of energy in proportion to their importance[23].

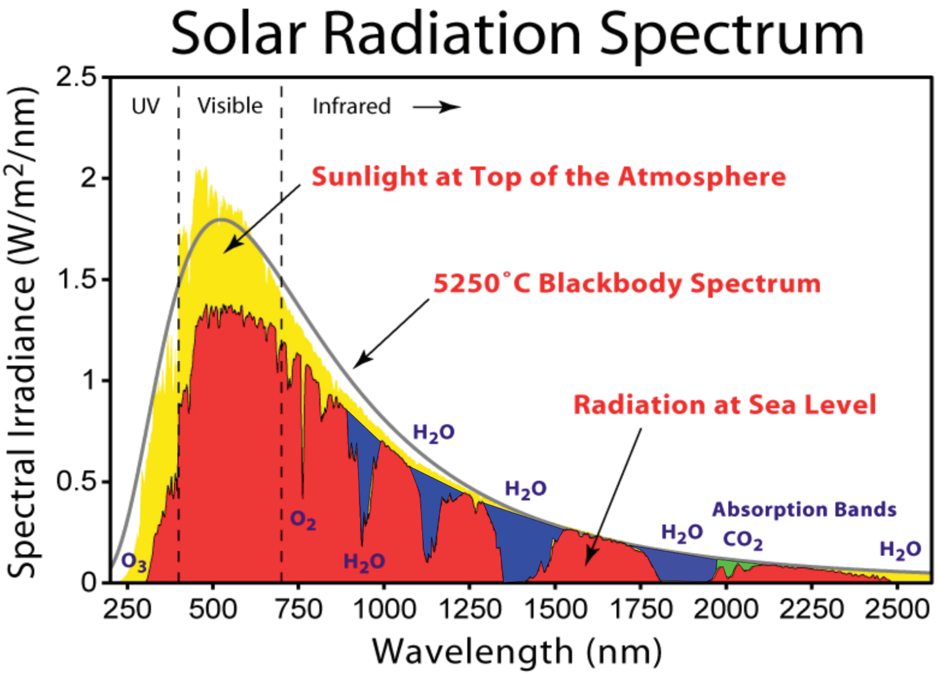

Figure 1.4: An image showing a solar emission spectrum[25].

1.3 Historical Development of Photovoltaic Technology

The photovoltaic effect was first discovered in 1839 by a French physicist, Edmond Becquerel. He noticed that the flow of electrical currents originates from certain photon/light induced chemical reactions. The theoretical elucidation for the photoelectric effect was later given by Albert Einstein in 1905[27]. In 1877, the discovery of photocurrents in selenium-metal junctions led to the application of photoelectric effect in a solid system, the photovoltaic effect in thin films that are at a sub *mm* scale in 1883 and the evolution of doped semiconductors for solid state photovoltaic devices in 1927[28, 29, 30]. In 1954, the first embodiment of what is considered as a modern solar cell came to existence and was reported by the Bell Laboratories in the USA, this was driven by the optimized growth of single-crystal Si and the fabrication of the first p/n junctions. The first Si based solar cells had an efficiency of 6% and this spurred interest in the field of renewable energy, because at the time, 6% was higher than any previous energy device and people could see the potential of this technology to revolutionalize the energy sector. The first cell produced at the Bell Laboratories was also used to power the transmission of voices over telephone wires[31].

Solar cell technologies are conventionally categorized into three generations. The first generation of this technology is based on thick crystalline Si wafers and they currently dominate the commercial market, because of their high efficiency compared to other generations of solar cells. The highest efficiency of these solar cells record to date is between 20 - 25 %, but they require a lot of energy for large scale industrial production.[32]. The second generation of solar cells were developed to reduce the costs of production associated with thick films by trying to make them thinner. The efficiency of these devices are low compared to their first generation counterparts. The efficiency of the second generation solar cells ranges from 10 - 15 % and their cheaper production costs is a motivation for trying to enhance their efficiency. Third generation PV technology uses organic materials, such as polymers or small molecules. These organic materials display photovoltaic properties which are high optical absorption and low production costs. Organic photovoltaics (OPVs) have the short lifetimes and lowest power conversion efficiency, which are the critical factors hindering their application. The efficiency of these solar cells is above 10%, reaching close to 12% and it is predicted that the combination of these organic and inorganic materials will lead to the fourth generation of solar cells, which are estimated to have an efficiency of up to 41%[33, 34, 35, 36, 37].

In 1970, solar panels were produced for a lot of applications, especially in countries where electricity was unavailable or expensive. Researchers started looking for different ways to make the production of the cells to be less expensive compared to commercialised cells, which is based on crystalline silicon (c-Si). The less expensive solar cells have a lower efficiency compared to c-Si and they are made from a-Si:H, which can easily be deposited as thin films[38]. The first experimental fabrication of a-Si:H solar cell was performed by David Carlson and Christopher Wronski at the Radio Corporation of America (RCA) Laboratories in 1976. They reported an efficiency of 2.4% when the single p-i-n a-Si:H solar cell was deposited on a glass substrate and aluminium was used as a back contact. The reason behind the layout as a stacked solar cell was to increase the output voltage of an a-Si:H solar cell. These solar cells were commercialised by electronic companies such as Fuji Electric and Sanyo in 1976, because of their application in consumer electronics such as calculators and watches[39, 40, 41].

In 1980, the a-Si:H based alloys were studied in more detail and the conversion efficiency in the lab was found to be 9% and the efficiency of the commercialised stacked solar cells was 5%. Recent approaches have shown even further cost reduction in the production of a-Si:H solar cells compared to the preferred c-Si solar cells. Light trapping is the standard technique for improving the a-Si:H solar cell efficiencies and for harvesting the spectrum of incoming sunlight. The efficiency of a-Si:H solar cells has been increasing over the years, the highest efficiency recorded to date is 11.3% − 15% [42, 43, 44].

1.4 Motivation for Thin Film Solar Cells

The most developed thin film solar cells are amorphous based silicon thin film solar cells, because they can be deposited continuously on a standard glass substrate using different techniques and this will cut down production costs. Amorphous Si solar cells have higher optical absorption it is easier to incorporate Plasmon based light management schemes on the devices. Improving the efficiencies of the current a-Si:H solar cells, while not sacrificing the production cost remains the crucial driving force in the sustainability and commercial viability of solar cell based devices. Flexible PV is only a niche area. Large scale PV plants must be based on rigid and robust panels, and this will dominate the market for photovoltaics worldwide. Thin film solar cells are easier to produce than c-Si solar cells, and used for multiple applications or generally in situations where the space available for photovoltaics is very small.

1.5 Problem Statement

The problem about a-Si:H solar cells is their low conversion efficiency compared to c-Si solar cells. However their low cost enables them to be a superior potential solar cell devices that can remedy the exigent energy challenges around the world, especially in South Africa, since there is a shortage and rationalization of the electricity usage that has led to load shedding which has far reaching implications to industries and the country's economy. The advancements of smart grid technologies allow for higher levels of renewable penetration, especially solar energy into the grid and are improving the grid's efficiency, energy security and resilience. A lot of techniques have been studied in the literature, but the efficiency has been increasing rather modestly. For the a-Si:H solar cells to surpass the efficiency of the preferred c-Si solar cells, new strategies to light absorption capabilities have to be developed. These strategies have to be implemented during the fabrication processes used, improving the architecture of the device and understanding the optical properties in the active layer.

1.6 Aims and Objectives

The aims of this project are to evaluate the possible fabrication of silicon based photovoltaics with existing infrastructure and to increase the efficiency of these solar cells using plasmonic nanoparticles. These modifications will enhance the short-circuit current density (J_{sc}) and in turn improve the efficiency of the photovoltaics.

The objectives of this project are:

(i) To grow high quality hydrogenated a-Si layers by sputtering.

(ii) To dope a-Si layers using Al and P as dopants.

(iii) To fabricate a working silicon photovoltaic p-i-n architecture as a reference solar cell.

(iv) Investigating the p-i-n junction silicon based solar cells.

(v) Investigating the optoelectronic properties of silicon based photovoltaics after implanting plasmonic nanoparticles at various layers in the device.

(vi) Incorporation of Au and Ag nanoparticles the commercial a-Si device.

(vii) Enhancing the commercial a-Si device with $ZnO : Tb^{3+}$ as a down-conversion layer.

1.7 Structure of the Dissertation

This dissertation consists of six chapters and the structure of the dissertation is as follows:

Chapter 1: Describes the importance of increasing the efficiency of photovoltaic devices or solar cells and also gives the motivation for this study by looking at the current trends in solar energy technologies. The low production cost of a-Si:H solar cells and its advantages are presented as well.

Chapter 2: Presents a literature review on the working principles of solar cells in general and explores on previously published studies concerning the efficiency enhancement strategies of photovoltaic devices.

Chapter 3: Serves as the theoretical background to describe the plasmonic resonance of metal particles. The absorption mechanisms in a-Si:H solar cells are discussed when plasmonic nanoparticle are used and different applications of surface plasmons.

Chapter 4: Deals with various experimental techniques used in this work, such as equipment and a brief overview of each equipment. The equipment can be categorized into two types. The first part describes the working principles of experimental setups to deposit different layers of the solar cells and the synthesis of the plasmonic nanoparticles. Secondly, the equipment for the characterization of the nanoparticles, the layers in the device and the fully functional device is described in some detail.

Chapter 5: Discusses the results and the analysis obtained from the techniques applied in the experiments. This also includes the analysis of the I-V and J-V chracterization of the functional solar cell devices, the bare nanoparticles and nanoparticles incorporated in the working device.

Chapter 6: Gives a summary of the experimental results. The dissertation is concluded and possible recommendations will also be given for future improvements.

Chapter 2

2 Literature Review

2.1 Working Principles of Photovoltaic Devices

The operation of solar cells is based on the photovoltaic effect, which is the conversion of light energy to electrical energy[45]. The light from the sun is composed of very small energy packets called photons. Some of these photons are absorbed by the semiconductor, however photons of energy less than the bandgap are transmitted through the device without being absorbed, leading to losses[46]. The photovoltaic effect that underlies the generation of electric current in doped semiconductors appears at the interface between two doped semiconductors , i.e p-type and n-type Si. When light strikes the semiconductor material, the photons will first of all be reflected, transmitted or absorbed by the material and close to the interface, electrons and holes are produced due to different mobilities of majority charge carriers on the p and n side of the junction, electrons and holes are separated and collected at the electrodes to generate electric current. The production of electron-hole pairs can be explained by the energy band diagrams illustrated in Figure 2.1. It shows two energy levels, a valence band as the lowest occupied energy level and a conduction band which is the highest energy level. The valence band contains the highest unoccupied energy levels of the electrons known as valence electrons, which are bounded to their parent atoms. In order for an electron to be removed from the atom, an energy greater than the energy bandgap separating the two energy levels is required and there will be free electrons located in the higher conduction band. Each electron that migrates to the conduction band leaves behind a quasi particle known as a hole and this excitation creates an electron-hole pair. In the case of Si, the electron-hole pair is weakly bound and it gives rise to a hydrogen-like state referred to as the Wannier exciton. Note that the n-type semiconductor contains free electrons in the conduction band because of the ease of ionization of the donor atoms and the p-type semiconductor contains holes due to the incomplete covalent bond around each donor atom[47]

At the interface, electrons (negatively charged) gather around the n-type semiconductor and the holes (positively charged) gather around the p-type semiconductor. Electricity (flow of electrons) is created when the two electrode are connected together using an electrical wire as depicted by Figure 2.2. The carriers will flow under the driving force of diffusion up to the chemical potential which plays a major role in driving the charge carriers, resulting in the Fermi level to be the same in the p-type and n-type semiconductors. A considerable amount of available sunlight will thus lead to a quite substantial flow of free charge carriers. The amount of light incident on the cell is therefore proportional to the amount of current flowing inside the cell[49].

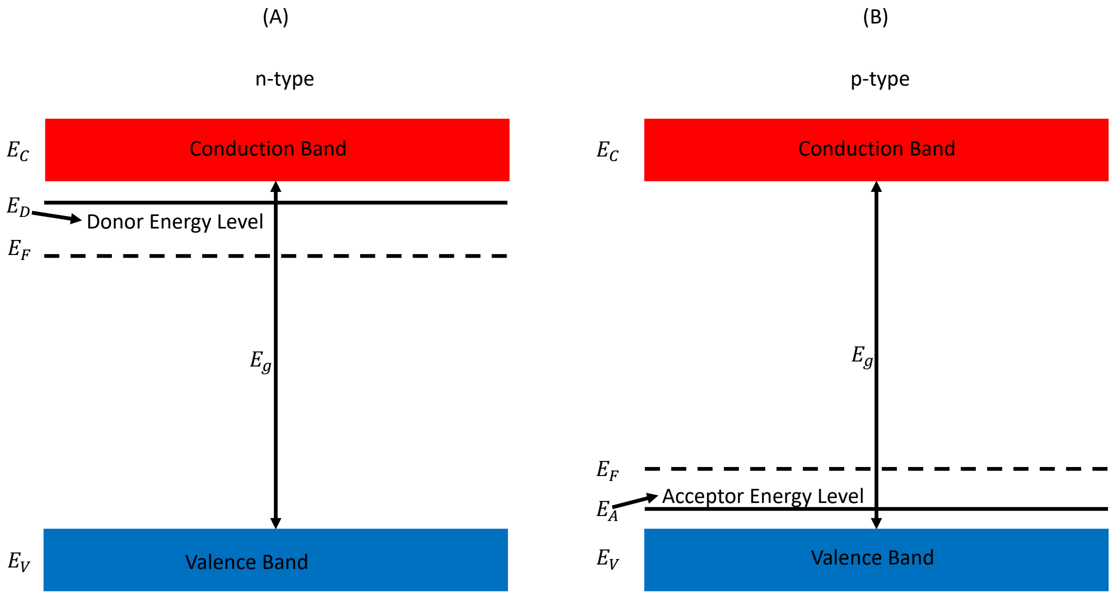

Figure 2.1: An image showing band diagrams of p-type and n-type semiconductor materials[48].

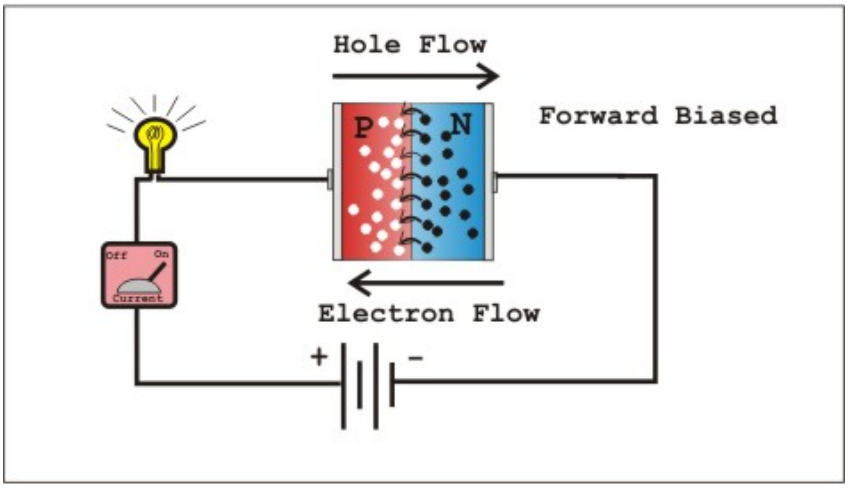

Figure 2.2: A p-n junction showing the flow of electrons and holes to create electricity[48].

2.1.1 P-I-N Junction

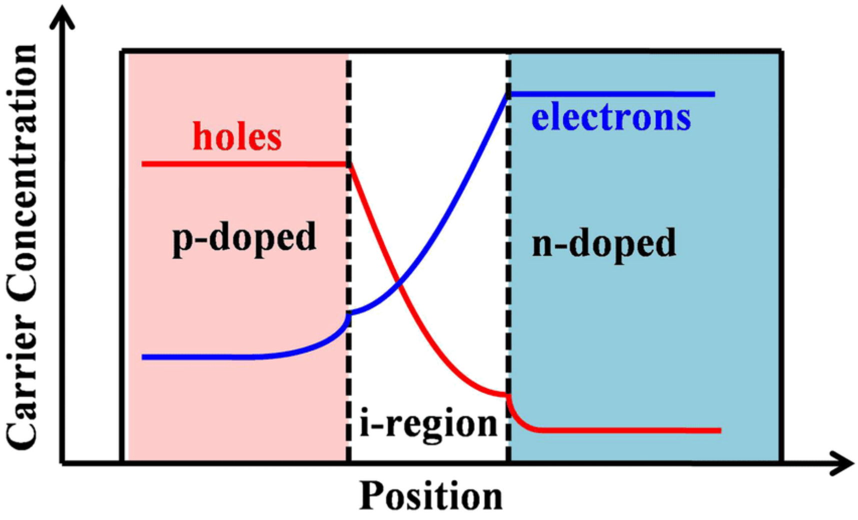

Figure 2.3: An image showing a schematic diagram of a p-i-n junction[50].

The p-i-n junction design is similar to the p-n junction, the only difference is that there is an absorbing layer of intrinsic semiconductor between the p-type and n-type layers. The photocarriers in a p-i-n structure are collected by drift instead of diffusion. This intrinsic semiconductor region sandwiched between the two doped regions results in a larger energy bandgap and leads to a large potential difference bounded by vastly different hole and electron conductivities. The intrinsic layer is essential to extend the thickness of the depletion layer, so that the photons can be absorbed effectively and the electric field is able to extend over a wider region, as shown in Figure 2.3. The electron-hole pairs generated in the i-layer are driven in the direction of the contacts by the electric field, so that the trapping or recombination of charge carriers can be avoided in the doped regions[51].

2.1.2 Organic Solar Cells

Organic solar cells are devices that are based on active organic materials in the form of polymers, dendrimers and small organic molecules to convert light energy into electrical energy. The organic materials used in these photovoltaic devices are based on conjugated π electron systems[52]. Delocalised orbitals such as π and π^* partially controls charge transport and optical absorption in these conjugated systems. The semi-conductive organic molecules have the capability to absorb light and to generate the transport of electrical charges between the conduction band of the absorber to the conduction band of the acceptor[53, 54].

The working principles of organic solar cells is one of the most researched topics in photovoltaics, because of their fascinating electrical and optical properties due to the conjugated systems in organic compounds[55, 56]. The photons absorbed by the solar cell produces an electrostatically bound electron-hole pairs known as Frenkel excitons, rather than the free charges produced in inorganic solar cells. The energy variation between the Highest Occupied Molecular Orbital (HOMO) of the acceptor material and the Lowest Unoccupied Molecular Orbital (LUMO) of the donor material provides the sufficient energy for the separation of Frenkel excitons when light is absorbed. Inorganic systems have the valence band at the top and the conduction band at the bottom instead of HOMO and LUMO energy levels. There is a difference in stability (lifetime) and localization properties of Frenkel excitons as compared to Warnier excitons, which has to do with the nature of the chemical bond in organic systems. The generated excitons move within the polymer chain leading to chain deformation in order for the supplemental unstable energy to be minimized. The design and performance of organic photovoltaics is influenced by the diffusion length of the excitons, which is restricted to a range of 10 *nm*. The electrostatically coupled electron hole pair is separated into free charges within the range of 10 *nm*. This dissociation of excitons takes place at the donor and acceptor interfaces. The dissociation of excitons is controlled by the disparity in the LUMO energy levels of the donor and acceptor materials. In order for ample charge separation to occur, the exciton binding energy should be less than the difference in LUMO energy levels and this energy difference should be around $0.19 - 0.3\ eV$[57, 58, 59, 60].

The energy difference can be expressed as follows[52]:

$$Exciton_{BE} < \Delta(LUMO_D - LUMO_A) \tag{2.1}$$

The free charges generated from the charge separation process will travel through materials, such as an Indium Tin Oxide (ITO) and a poly(3, 4- ethylenedioxithiophene) doped with poly(styrene sulfonic acid), commonly known as PEDOT:PSS which is a conductive conjugate polymer that acts as an anode buffer layer. The charges will be collected by electrodes, such as Aluminium and Calcium, as shown in Figure 2.4. The current flow is influenced by the use of electrodes with different work functions. The electrode used as an anode has to be a material with a high work function and the cathode material has to have a low work function. This allows the holes to travel to the anode material with a high work function and the electrons to the low work function cathode material. This situation is similar to the case of inorganic materials. Connecting the electrodes to an external circuit will produce electricity[61].

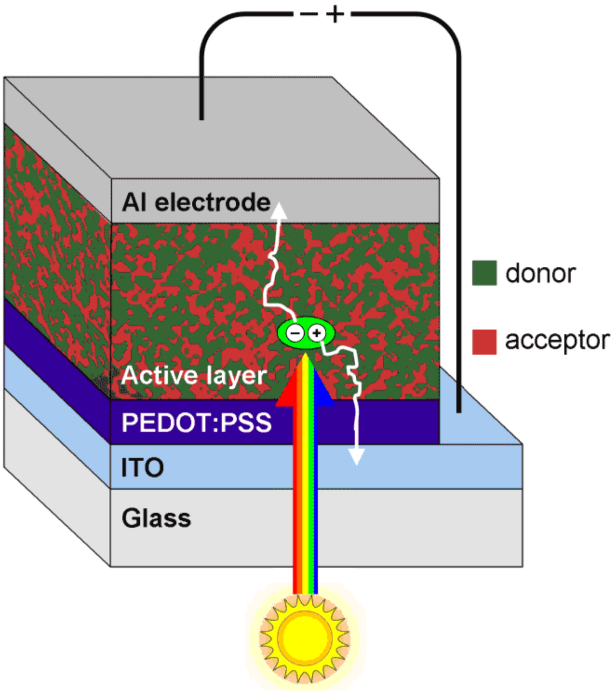

Figure 2.4: An image showing the structure of standard organic cell [62].

2.1.3 Silicon Solar Cells

Silicon is the most prominently used semiconductor material to manufacture inorganic photovoltaic cells. The Si atom has four valence electrons and each Si atom allocates each of its four valence electrons to the nearest Si atom, this creates a covalent bond between the two Si atoms and this gives Si a tetrahedral lattice structure. Si can be converted into two types, which are either n-type or p-type. The reason for the conversion of Si into types is because Si is a poor conductor at room temperature and its conduction can be increased by adding impurities to the intrinsic Si semiconductor. The addition of impurities mainly influences the electronic structure of the semiconductor[63, 64]. The Fermi level, which is the average work done to remove an electron from the material, in an intrinsic Si semiconductor is positioned close to the center of the band gap. This is because the concentration of thermally activated holes and electrons in an intrinsic semiconductor is equal. The process of adding impurities in the semiconductor is known as doping and the impurities are called dopants[65]. The position of the Fermi level will be shifted from the center of the band gap in the direction of either the valence band or conduction band depending on the dopant used. Atoms with an extra valence electron than Si are used to make an n-type semiconductor and the one with less valence electron are used to make a p-type semiconductor[66]. The n-type materials are made from group V elements (P, As or Sb) in the periodic table. Their atoms have five valence electrons and these electrons can form covalent bonds with the Si valence bonds, since the Si atom have four valence bonds. The four valence electrons from each atom form a covalent bond around the Si atoms and thus, an extra valence electron will be available for conduction. After doping, a lot of electrons will be added to the conduction band and this will increase the number of free electrons available for conduction. The p-type materials are fabricated using group III elements (B, Ga or In) in the periodic table. They have one valence electrons less than Si. A hole will be formed, because the electrons available are not adequate to form four covalent bonds around the atoms. In a p-type material, there are electrons constrained to the bonds and this results to an increasing number of holes[67, 38].

A potential barrier is always created when the p-type and n-type materials are connected to each other and this barrier is crucial to the working principles of inorganic solar cells[68]. The electrons and holes will be distributed equally closer to the junction by a process known as diffusion, if there is no applied electric field. The electrons in the n-type material diffuse to the side of the p-type material and leaves positively charged pentavalent ions near the junction in the n-type material. The holes in the p-type material move across the n-type region and leaves negatively charged trivalent ions closer to the junction in the p-type region. This movement of electrons and holes generates a built in electric field[38]. The absorption of photons can take place anywhere in the device, but it is preferred to be closer to the p-n junction, so that a lot of electron-pairs can be created. The device can absorb visible photons to excite the electrons above the bandgap, where they have a chance of being collected. The thickness of the absorbing layer is proportional to the layer's optical depth and the best absorption can be achieved with a layer of few tens or hundred microns. The photons originally absorbed by the generation of electron-hole pairs are used up while the electrons power the external circuit and equilibrium is conserved. Electron-hole pairs will be continually generated by the light incident on the cell and this creates a charge imbalance. The electric field reduces the charge imbalance by giving up electrons in performing work[69].

2.1.3.1 a-Si:H Photovoltaics

The a-Si:H solar cells have three layers that are deposited using gases in either the p-i-n or the n-i-p sequence, as shown in Figure 2.5. This is different from the usual p-n sequence in c-Si solar cells. The structure of the a-Si:H PVs is a result of inadequate carrier transport, needing drift to aid with carrier collection. The undoped intrinsic (i) layer is placed between the p and n layer, because it keeps the doping atoms out of the absorbing layers (p and n). The three layers are very thin, the thicknesses of the undoped layers are typically around $300-500\ nm$, $10-20\ nm$ for the p-type layer and $20-30\ nm$ for the n-type layer[41, 38]. This rationale for the thicknesses is to maximise the absorption of photons in the i-layer and minimise the photoabsorption in the p and n layers in order to enhance the efficiency of a-Si:H photovoltaics[38].

The photons incident on the solar cell enters the device through the p-type layer, which is transparent. These incident photons are predominantly absorbed by the intrinsic layer and all the three layers absorb about 2.5 times more energy than the conventional c-Si[71]. The working principles of p-i-n and p-n junctions are similar. The carrier transport in a p-i-n junction is influenced by the midgap defects which lead to generation and recombination processes. The other defects that occurs in a-Si are known as deep midgap states and they are caused by the film defects when the deposition process is taking place. These states are also caused by the missing valence bonds called dangling bonds[72]. The electric field is produced in the intrinsic layer to collect and separate the generated electron-hole pairs and the minority diffusion length carrier is around $0.1\ \mu m$. The thickness of the intrinsic layer should be less than the width of the depletion layer so that the built in electric field, which is more than $10^4\ V/cm$, is across the whole of the intrinsic layer[41]. Amorphous Si has a short range atomic order and this makes each Si atom only an average of four bonds with four atomic neighbours also causing the bonds

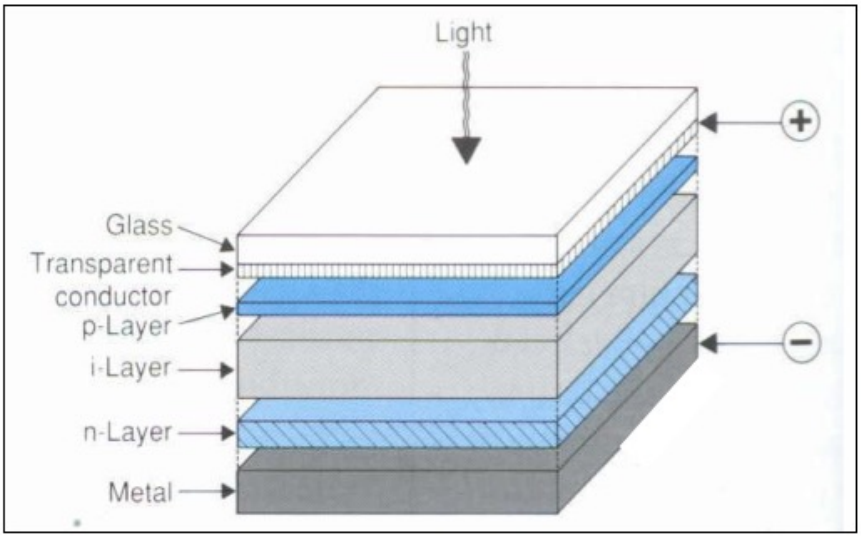

Figure 2.5: An image showing the structure of an a-Si:H standard solar cell[70].

not to be uniform[43].

2.2 Efficiency Enhancement Strategies

The efficiency in thin film based solar cells is currently researched at numerous institutions around the world. Despite their potential for remarkably lower production cost, thin film solar cells have low efficiency compared to the preferred c-Si photovoltaics. The reason for the low efficiency is because of the weak absorption by the photons with long wavelengths[73]. In order for the efficiency of any photovoltaics to increase, the absorption of photons by the device has to be improved. Light trapping is a customary method for improving the efficiency of thin film photovoltaics and for harvesting the spectrum of the incoming photons[74]. Most semiconductor materials, including a-Si have a high refractive index in the visible range of the electromagnetic spectrum and substantial amount of the photons are reflected from the top surface of the film.

The performance of a-Si:H solar cells is also strongly dependent on the characteristics of its layers. It is imperative that the thicknesses of each layer, the overall ideal structure and its functions be understood when fabricating it. Embedding metallic nanoparticles inside a-Si:H photovoltaics is one of the most commonly used light trapping techniques to improve the efficiency of a-Si:H solar cells. Other methods used for light absorption in thin film devices are spectral conversion (up and down) methods and using photonic crystals as back reflectors[75, 76].

2.2.1 Plasmonic Nanostructures

Plasmonic nanostructures are metallic resonant structures that mediate the interaction of free charges and light. These nanostructures absorb photons at a nanoscale by means of the collective oscillations of the free electron gas through the excitation of the surface plasmon resonance (SPR) as illustrated in Figure 2.6 . Excitations of the SPR will lead to the decaying of plasmons by radiating their energy which will result in the scattering of light or they can decay non-radiatively by locating the acquired energy to electrons in the conduction band of the material that produces hot electrons or converting absorbed photons into heat [77, 78]. A lot of work has been done to quantify the effects of plasmonic resonances of metallic nanoparticles on the enhancement of light trapping in solar cell devices, where the investigation of different parameters such as size, shape, interaction of particles, properties of materials and the dielectric properties of the surrounding medium have been considered. It turns out that plasmon resonance strongly depends on the shape, size, and density of the NPs. The condition that limits the localized behaviour of plasmon resonances is the physical contact between the adjacent NPs. The NPs in contact with each other will resonate at lower frequencies due to hybridization effects[79].

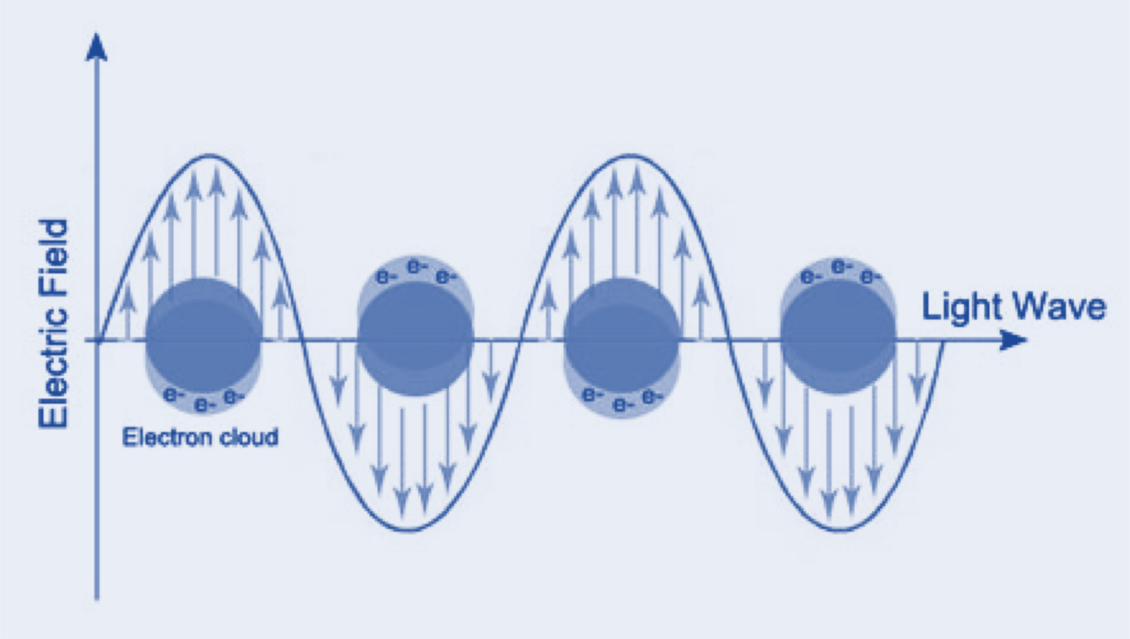

Figure 2.6: An image showing the SPR when the free electrons in the metal are propelled into oscillation.

The fundamental work that illustrated experimentally the prospective of increasing light absorption in Si thin film PVs was done by Derkacs et al., 2006[80]. In his work it was discovered that gold NPs deposited on the surface of the solar cell increases the short-circuit photocurrent generation by 8.1%. This observation was supported by the simulations due to Lim et al., 2007[81]. The work done by Ferry et al., 2010[82] followed by investigating the fabrication, design and the measurement of a-Si:H solar cells embedded with gold plasmonic structures at the back contact. This method increased the short-circuit current response of the device by 50% when it is compared to the device without the nanoparticles at the back end.

Thin film solar cells, such as a-Si:H, have three layers. This means that the plasmonic nanostructures can be implanted in one of the layers, including the absorber layer (i-layer). This was demonstrated by Atwater et al., 2010[83]. Depositing the plasmonic nanostructures inside the i-layer drops the efficiency and the short-circuit current of the device. These parameters of the PV device decrease regardless whether the size of the nanoparticles is increased or decreased. One of reasons for the drop in efficiency when plasmonic nanostructures are embedded in the absorber layer is the density of defects, mainly around the metallic NPs[84]. The occupancy of these defects increases optical losses and this also increases the recombination rate. The recombination rate is considered to be 100 times higher compared to the value when there are no nanoparticles[85].

Defects can occur in one of the three layers in a p-i-n structure of an a-Si:H PV when the plasmonic NPs are embedded, but the defects are lower in highly doped layers (p and n) compared to the absorber layer. This is because most of the incoming photons are absorbed by the p-layer before approaching the depletion region and the probability of generating free electron-hole pairs outside the depletion region increases which leads to the increase of the recombination rate[86, 87]. In order for electron-hole pairs to be created inside the depletion layer, the photons must propagate in a longer path in the device. Thus, the efficiency will be higher when the plasmonic nanostructures are deposited at the rear end of the absorber layer[88]. The highest efficiency in a p-i-n structure is obtained when the metallic nanostructures are located at the rear end of the absorber layer. This is because at the rear end of the absorber layer, the weakly absorbed photons can be scattered back into the absorber layer[89].

These effects are well established on the basis of a standard theory of light scattering by a spherical particle that was established by G. Mie in 1908[90, 91]. The scattering cross-section of a particle with a radius R much smaller than the wavelength λ of light depends on R^6 and its absorption cross-section depends on R^3. Thus, absorption is of great significance for extremely small particles and scattering is important for particles with a circumference comparable to the wavelength of light[92].

The metallic NPs can also be embedded simultaneously in the two doped regions, but the size of the particles has to be controlled. Large nanoparticles around the size of 200 - 300 nm can be placed at the bottom of the absorber layer to improve reflection and the small NPs around the size of 30-40 nm can be located at the p-layer to allow some of the optical energy to be absorbed by the device. The rationale for the exploitation of the size of the metallic nanostructures is because large metallic NPs resonate at low frequencies and smaller nanoparticles resonate at high frequencies. Thus large NPs contributes to the scattering of incident photons and small nanoparticles contributes to the absorption of light[93].

2.3 Spectral Conversions

The solar spectrum incident on a PV device comprises a wide range of photons, consisting of different wavelengths varying from 250 - 2500 nm. The conversion of the solar spectrum accessible in the atmosphere is defined as the ability of utilising the solar cell device in order for it to complement the solar spectrum better. The photons absorbed by a single junction PV are the photons with equal or greater energy as the bandgap energy of the solar cell's material. The higher energy photons will lose their excess energy due to thermalisation. Photons with less energy than the bandgap energy are not absorbed by the device and these photons cannot generate an electron-hole pair[94, 95]. The losses due to an inferior response for UV and IR photons can be minimised by shifting or changing the spectral light photons from an energy level to another by producing more, less or equal number of photons and this process is known as spectral conversion. This process can be achieved in practice by using luminescence up and down conversion layers[96].

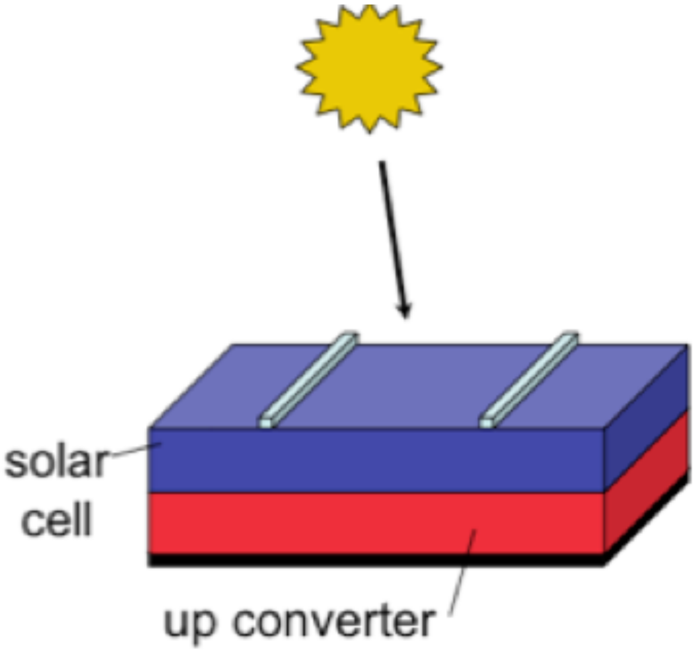

(a) Structure of a solar cell fitted with an up-conversion layer and a back reflector.

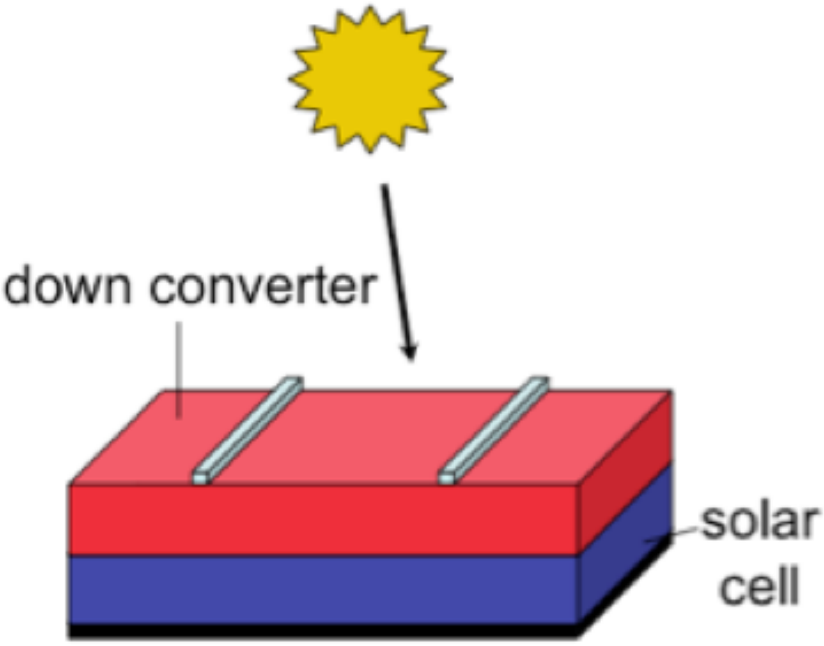

(b) Structure of a solar cell fitted with a down-conversion layer and a back reflector.

Figure 2.7: Images of an up conversion layer placed at the back of the PV cell (a) and of a down conversion layer placed at the top of the PV cell (b)[95]. A detailed description of each luminescence process is presented in the subsequent sections.

2.3.1 Up-Conversion

Up-conversion (UC) is an optical process whereby two photons with lower energy are combined to produce a photon with a higher energy[97, 98]. This process was first suggested in the late 1950s by Bloembergen et al., 1959[99], which led to the development of infrared detectors (IR) by detecting IR through sequential absorption. UC materials were first applied in solar cells by Saxena et al., 1983[100]. The layer for UC is placed at the back of the PV device with a back reflector, as shown in Figure 2.7a, so that it can utilise the transferred solar spectrum through the PV device[101]. The materials for UC layers contain active ions that have the proper energy scheme level for absorption which are embedded in one host material. Lanthanide ions, such as in Er^{3+}, Yb^{3+} and Ho^{3+} have so far extensively been used as active ions in UC layers, also in host materials such as $NaYF_4$, $Gd_2(MoO_4)_3$ and $TeO_2 - PbF_2$ [102, 103, 104, 105, 106, 107]. The highest solar cell efficiencies reported to date have been obtained from $NaYF_4$ implanted with Er^{3+} and Yb^{3+} as active ions in UC layer materials. The up-conversion layer $NaYF_4$ doped with either Er^{3+} or Yb^{3+} on top of a GaAs cell showed an efficiency increase of 2.5%[108].

Amorphous Si is known to have a wider energy bandgap compared to c-Si, and a-Si:H solar cells have bandgap energies of up to ~ 2 eV. The first application of a UC layer to an a-Si:H PV cell was done by De Wild et al., 2010[109], using $\beta - NaF_2 : Yb^{3+}, Yb^{3+}$ as a UC layer material with a thickness of 200 - 300 μm. They continued the work in 2010 by using a UC layer with the same host material, but different concentrations of the dopant ions, which are $Yb^{3+}(18\%), Yb^{3+}(2\%)$ and this increased the efficiency of the device by 0.03%. This was followed by the work of Liu et al., 2011[110], where they coupled $Y_3Al_5O_{12} : Yb^{3+}, Er^{3+}$ transparent ceramics with dye-sensitized solar cells and this increased the $J_{sc} = 0.2\, mA/cm^2$ by one order of magnitude. De Wild et al., 2013[111], improved the solar response of an a-Si:H PV by using Gd_2O_2S as a host material and the dopant ions, $Yb^{3+}$and Er^{3+}. A high transparency is also a critical factor for the effective performance of UC layers in a-Si:H solar cells[112, 113]. This key factor can be manipulated by preparing different concentrations of $Er^{3+} - Yb^{3+}$ and co-doping it with $TeO_2 - PbF_2$ oxyfluoride tellurite glasses. This technique can increase the efficiency of an a-Si:H device by 0.45% [114, 115]. Other UC materials that have been extensively studied as a potential replacement of current host materials are bromide ($Cs_3Lu_2Br_9$), fluoride ($LiYF_4$), chloride ($Cs_3Lu_2Cl_9$) and oxide ($YAlO_3$) compounds doped in Er^{3+}, Ho^{3+}, Dy^{3+}, Nd^{3+}, Tm^{3+} and Pr^{3+}[116, 117, 118, 119, 120, 121, 122]. The lanthanides are stable in their trivalent form and consist of a partly filled 4f inner shell that is the source of optical and magnetic properties in these materials. All the combinations of the lanthanides can have a very complex spectrum of energy levels, as depicted by Figure 2.8. The logic for doping transparent glassy materials with rare earth ions is because of their optically active 4f orbital being well protected from the host material by the outer filled 5s and 5p orbitals but the surrounding crystal field will still give rise to the splitting of the energy levels[98, 123].

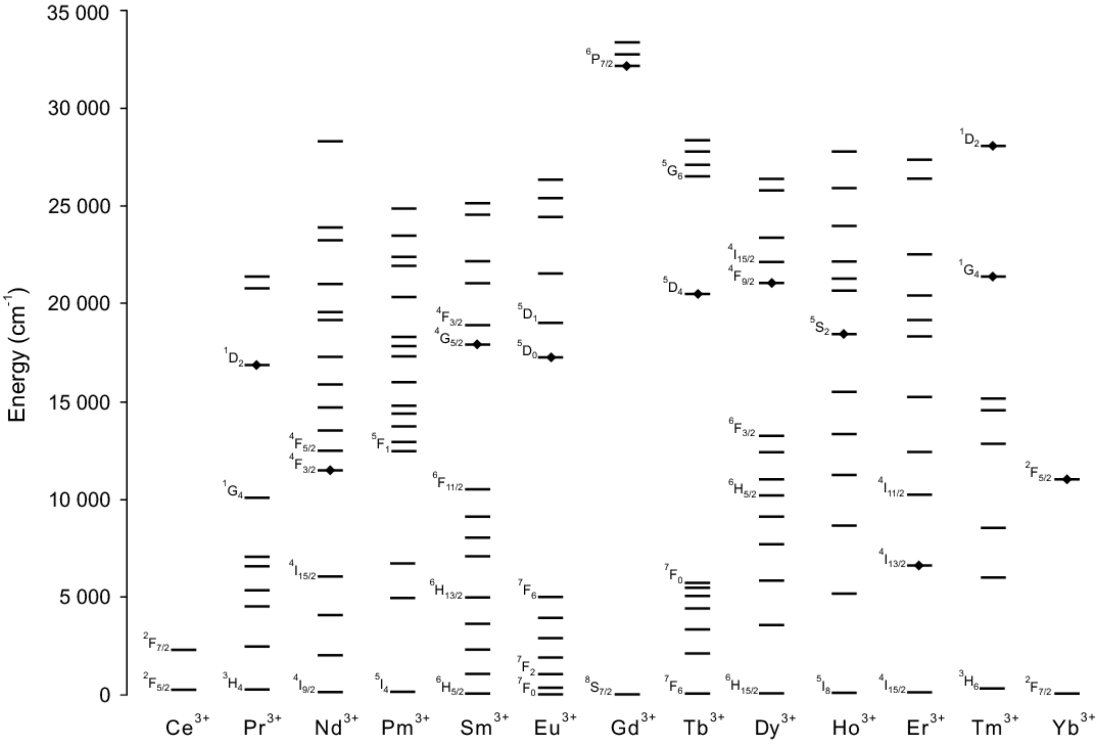

Figure 2.8: A diagram of the energy levels of trivalent lanthanide ions[124].

2.3.2 Down-Conversion / Downshifting

Energy transfer and down-conversion (DC) is the converse process to UC, whereby a material absorbs high energy photons and generates lower energy photons[125]. This process, like UC, was also theoretically proposed for the first time in the late 1950's by Dexter et al., 1957[126]. The theory was experimentally proven independently in 1974 by Piper et al[127] and Sommerdijk et al[128] using Pr^{3+} as a lanthanide and YF_3 as a host material. The first theoretical description of DC for solar cells was by Trupke et al., 2002[129] and an efficiency of 30.9% was predicted for solar cells with $E_g = 1.1$ eV. This was followed by a first experimental demonstration of DC on solar cells in 2004, which involved the coupling of $Tb^{3+} - Yb^{3+}$ through cooperative energy transfer from Tb^{3+} to two Yb^{3+} ions[130]. The material layer of DC is placed at the top of the solar cell as shown by Figure 2.7b and the material layer is also made from two coupled active ions, one of the two ions always being Yb^{3+} embedded inside a host material. The lanthanides ions and host materials in DC are different from the ones used in UC. Higher efficiencies have been obtained by using coupled ions, such as $Tb^{3+}-Yb^{3+}$, $Tm^{3+}-Yb^{3+}$ and $Pr^{3+}-Yb^{3+}$ within different host materials, such as YF_3, $LiGdF_4$ and $(Y, Yb)PO_4$[106]. The application of the DC process in solar cells shows the potential efficiency enhancement only for solar cells with narrow bandgaps, such as c-Si PV cells. For wider bandgap solar cells, such as a-Si:H PV cells, active ions like Ho^{3+}, Er^{3+} and Nd^{3+} coupled with Yb^{3+} can be used as down converters with different host materials, because these systems reside in the energy range of 2.56-2.64 eV[131].

Chapter 3

3 Theoretical Framework

3.1 Metal-Semicondutor Contacts

One of the earliest practical investigations on semiconductor devices was the metal-semiconductor contact applied in a point-contact rectifier, which exhibited the dependence of the total resistance on the surface conditions and on the polarity of the applied voltage. This device led to a lot of applications since 1904. In 1938, W. Schottky established a theory for the rectifying behaviour of the device by introducing a principal notion known as a Schottky barrier, as shown in Figure 3.1. This energy barrier is formed at the interface of the metal-semiconductor junction. When a metal makes contact with a semiconductor, a linear characteristic can also be observed and this is because of the contact having a small resistance despite the polarity of the applied voltage. This contact is known as an ohmic contact and in electronic systems, ohmic contacts are indispensable to all semiconductor devices, including integrated circuits in order to make connections to other devices[132, 86, 133, 134].

3.1.1 Work Function

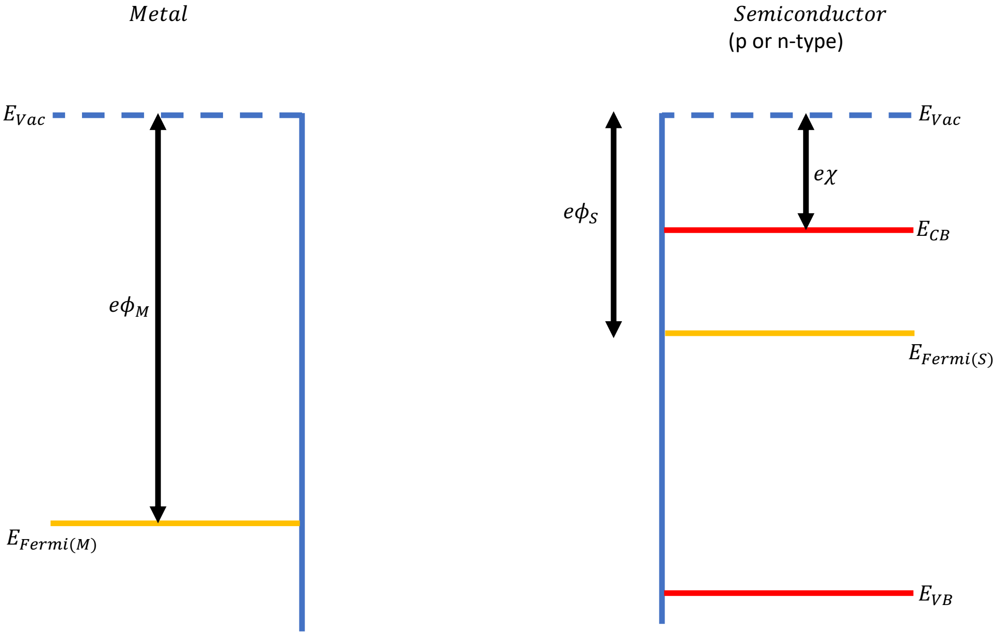

Figure 3.1: Schematic energy band diagram showing an isolated metal next to an isolated semiconductor (p or n-type).

Figure 3.1 illustrates the separated band diagrams of a metal and a semiconductor (p or n-type) next to each other. The band diagram of a metal is partially filled with electrons and this positions the Fermi energy (E_{Fermi}) at the top of the highest occupied level in a metal which lies above the conduction band. E_{Fermi} is the Fermi energy with subscripts M and S for metal and semiconductor, respectively. A parameter of great significance for the metal is the work function $e\phi_M$, which is defined as the work needed to remove the least tightly bound electron from a Fermi level to the vacuum level (E_{Vac}), i.e outside the material. A semiconductor is characterized by two parameters, which are the work function $e\phi_S$ and the electron affinity $e\chi$. The work function $e\phi_S$, is defined as the work required to extract an electron or hole from a p or n-type semiconductor, respectively. In metals, the work function is always equal to the electron affinity and in semiconductors, $e\phi_S$ is controlled by the type of doping. This is because the location of the Fermi level is dependent on the type of doping, i.e. the work function of an n-type doped semiconductor is smaller than a p-typed doped semiconductor[135, 136, 24].

The key parameters of the energy bands can be expressed as follows[86]:

$$e\phi_M = E_{Vac} - E_{Fermi(M)} \tag{3.1}$$

$$e\phi_S = E_{Vac} - E_{Fermi(S)} \tag{3.2}$$

$$e\chi = E_{Vac} - E_{CB} \tag{3.3}$$

E_{Vac} is constant for both materials, $E_{Fermi(S)} > E_{Fermi(M)}$ and this is true if $e\phi_M > e\phi_S$ before contact.

3.1.2 Schottky Barriers

After bringing the metal and the n-type semiconductor in contact with each other, as shown in Figure 3.2 (A), electrons will move in both directions because of their higher electrostatic potential energy and the metal will be negatively charged, creating a boundary known as the depletion region within the semiconductor [137]. Between the two materials (n-type semiconductor and metal), a barrier which averts the flow of electrons will be formed and it is known as the Schottky barrier $e\phi_{Bn}$. Assuming that an electron in a metal can be raised from the E_{Fermi} energy level to the conduction band (E_{CB}) energy level in the semiconductor, then it can also relocate from the metal into the semiconductor. From Eq (3.1), (3.2) and (3.3), the Schottky barrier corresponding to an n-type semiconductor in contact to a metal is given by:

$$e\phi_{Bn} = e(\phi_M - \chi) \tag{3.4}$$

When a metal and a p-type semiconductor are brought together as demonstrated by Figure 3.2 (B), the holes from the semiconductor will move to the metal. These holes will create a positive charge inside the metal, leaving behind ionized acceptor atoms. In this scenario, the Schottky barrier is defined as the barrier that prevents the flow of holes from the metal into the p-type semiconductor. In order for the hole in the metal to relocate to

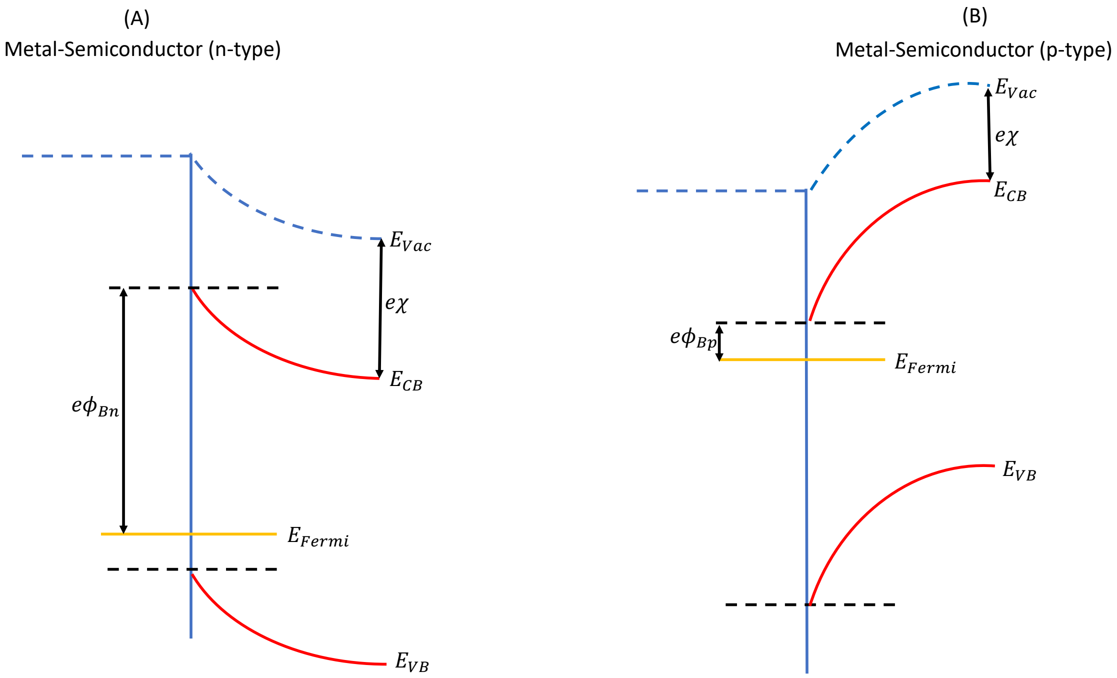

Figure 3.2: Schematic diagrams showing the formation of the Schottky barrier after the metal and the semiconductor are brought in contact with each other. (A) and (B) shows the resulting energy band diagrams of a metal-semiconductor (n-type) and metal-semiconductor (p-type), respectively after contact.

the semiconductor, it must increase its energy level from $E_{Femi(M)}$ to E_{VB}. Taking the E_{Vac} as a reference point, $E_{Femi(M)}$ is located at a distance that is the same as $e\phi_M$ and the distance of E_{VB} is the same as $e\chi + E_G$, where E_G is described as the energy band gap of the semiconductor. Therefore, the Schottky barrier for a p-type semiconductor in contact with a metal is given by the following equation[138, 139] :

$$e\phi_{Bp} = E_G + e\chi - e\phi_M \tag{3.5}$$

Thus:

$$e\phi_{Bp} = E_G - e(\chi - \phi_M) \tag{3.6}$$

Merging (3.4) and (3.6), we acquire the sum of the barrier heights for n-type and p-type which is approximately equal the band gap energy (E_g) and it is expressed as follows:

$$e(\phi_{Bn} + \phi_{Bp}) \approx E_g \tag{3.7}$$

ϕ_{Bn} is the Schottky barrier height for the electrons.

ϕ_{Bp} is the Schottky barrier height for the holes.

Eq (3.7) determines the conductivity between the metal and the semiconductor (p-type and n-type).

3.1.3 Current-Voltage (I-V) Characteristics

The I-V characteristics curves are the electrical response of a device and they are utilized to extract device electrical parameters and predict the performance of the device[140]. One of the parameters that can be obtained from the I-V curves is the Schottky barrier height of the metal-semiconductor junction, which is the barrier that the electrons or holes from the metal must overcome in order to flow easily to the semiconductor. To extract the Schottky barrier from the I-V curves, thermionic emission theory must be applied since it best describes carrier injection for low voltages. This phenomenon was reported in 1873 and it assumes that $e\phi >> kT$, which means that thermal equilibrium is entrenched at the plane that determines emission and this equilibrium is not influenced by the presence of the net current flow[141, 86].

For moderately doped semiconductors, the I-V characteristic of a metal-semiconductor under thermionic emission in the forward bias is given by the following equation:

$$J = J_s \left(\exp\left(\frac{eV}{k_B T}\right) - 1 \right) \tag{3.8}$$

J is the current density,

e is the magnitude of the electric charge,

V is the applied voltage,

k_B is the Boltzmann constant,

T is the operating temperature at which the I-V characteristics were carried out.

The saturation current density (J_s) is given by the expression:

$$J_s \approx A^* T^2 \exp\left(-\frac{e\phi_B}{k_B T}\right) \tag{3.9}$$

J_s is dependent on A^*, which is the effective Richardson constant. A^* is expressed as:

$$A^* = \frac{4\pi m^* k_B^2}{h^3} \tag{3.10}$$

with m^* as the effective mass of an electron or hole,

h is the Planck's constant.

Merging (3.8) and (3.9), we get:

$$J = A^* T^2 \exp\left(-\frac{e\phi_B}{k_B T}\right) \left[\exp\left(\frac{eV}{k_B T}\right) - 1 \right] \tag{3.11}$$

Under thermionic emission conditions and by deducing the forward bias condition in the I-V curve, then J_s can be approximated by a linear expression as $V \to 0$. Similarly through linearization of Eq (3.12), the barrier can be extracted. Starting from:

$$J = J_s \approx A^* T^2 \exp\left(-\frac{e\phi_B}{k_B T}\right) \tag{3.12}$$

and solving for ϕ_B using Eq (3.12), we obtain the barrier height:

$$\phi_B = -\frac{k_B T}{e} \ln\left(\frac{J}{A^* T^2}\right) \tag{3.13}$$

The barrier width is also known as the depletion layer (also called the space charge limited region). Under the given conditions, the region experiences no/zero net current densities [142]. The size (width) of the depletion layer is calculated using the following equation:

$$w = \sqrt{\frac{2\epsilon_r \epsilon_0 \phi_B}{eN}} \tag{3.14}$$

$\epsilon_r = 11.9$ is the relative permittivity or dielectric constant of Si[143, 144, 86],

ϵ_0 is the permittivity in vacuum,

N is the dopant concentration (electron donors/holes).

Once the size of the depletion layer is obtained, then the electric field (E) between the metal and the semiconductor can be calculated using the following equation:

$$E = \frac{eN}{\epsilon_r \epsilon_0 w} \tag{3.15}$$

Another parameter that can be extracted from the J-V curves is the specific contact resistance. This is a contribution to the total resistance of a system caused by the contact between the metal and the semiconductor. The contact resistance is defined as:

$$R_c = \left[\frac{\partial J}{\partial V}\right]^{-1}_{V=0} \tag{3.16}$$

Therefore,

$$R_c = \frac{k_B}{eA^* T} \exp\left(\frac{e\phi_B}{k_B T}\right) \tag{3.17}$$

The last parameter to be obtained is the sheet resistance (R_s), which can be found by using the Van der Pauw method according to the expression[145]:

$$R_s = \frac{\rho}{t} \tag{3.18}$$

t is the thickness of a homogenous film and ρ is the resistivity, which is calculated using the I-V characteristics by extrapolating values in the linear region of the graph and it is expressed as:

$$\rho = \frac{(\pi)(t)}{\ln(2)} \left(\frac{V}{I}\right) \tag{3.19}$$

For a rectangular/square shape of the film and a collinear arrangement of the contact probes. The general expression has the geometrical factor $f(Q)$, $f(Q) \rightarrow 1$ for films that are homogenous in thickness and

$$Q = \left(\frac{R_2}{R_1}\right)$$

Eq (3.19) is only valid for homogeneous samples. Substituting Eq (3.18) into Eq (3.19), we obtain:

$$R_s = \frac{\pi}{\ln(2)} \left(\frac{V}{I}\right) \tag{3.20}$$

3.2 Plasmonic Nanoparticles

Small scale metal NPs, having a size that is much smaller than the wavelength of light are known to reveal near field optical characteristics, such as Surface Enhanced Raman Scattering (SERS) compared to bulk metals[146]. A plasmon is a quasi-particle, meaning that it can be described by a collection of interacting particles such as free electrons or the Fermi gas. Plasmons occur at the surface of the metal, they are quantized and consist of collective oscillations of the free electron gas[147]. The wavelengths of light incident on the NPs are often larger than the size of the particles, thus for visible light, the wavelength is around 400 - 700 nm and the size of most NPs are below 100 nm. The excitation of an electron cloud by this external (EM) wave distorts the center of mass of the electron cloud leading to SP excitation as shown in Figure 3.3. If it is excited at resonance frequency for a particular configuration, then the absorption of light and the response of the particle will be very strong, but if it is not excited at its resonant frequency, then it will not absorb much light[148].

Optical absorption and scattering characteristics by metal NPs rely heavily on the surface plasmon absorption and this absorption is dependent on the size, shape and the

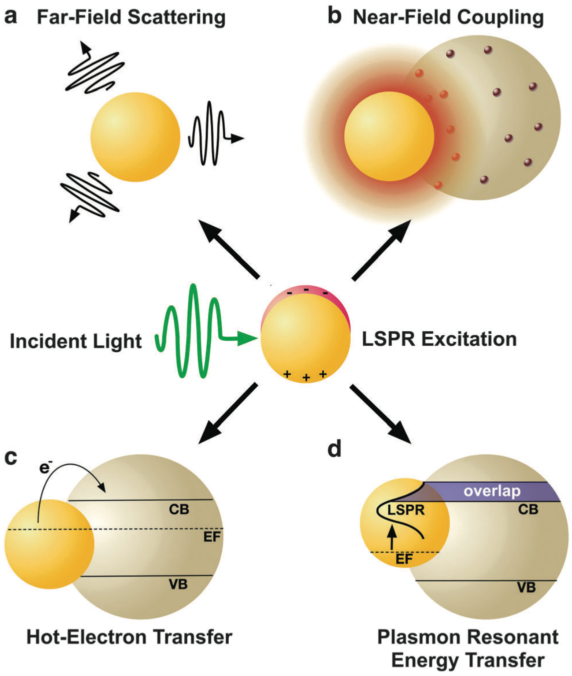

Figure 3.3: Schematic diagram showing the mechanisms of the enhanced optical near field around a plasmonic nanoparticle[149].

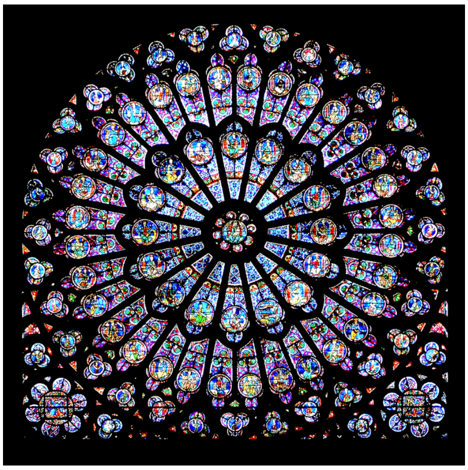

Figure 3.4: A picture of the Gothic stained glass window containing small amount of gold nanoparticles, exhibiting this unusual optical characteristic[150].

free electron density which is dependent on the metal used. The application of plasmonic NPs have been used for hundreds of years as represented by Figure 3.4. People used metal salts, like gold and silver, and mix them with molten glass and once they are in the glass, the metal particles will coagulate into small NPs. When you get the right size and the right mixture of these nanoparticles, there will be resonances at certain colours. For example, gold will produce bright red glass and silver will produce yellow glass, depending on the angle that the light hits the glass[151]. The first scientific elucidation of these phenomena was in 1908, when Gustav Mie proposed a theoretical explanation on the optical properties of metallic colloids[152]. The surface plasmons can be excited by the metallic NPs and this allows them to increase the optical path length in layers of thin film PVs to increase photoabsorption.

3.2.1 Surface Plasmon Polaritons

Surface plasmon polaritons (SPPs) occur when the surface and volume charge density oscillations are sustained by the metal's free electron gas at certain optical frequencies. The polaritons are due to the pairing of electromagnetic radiation and electron plasma excitations moving along the interface, and this only occurs when the wave vectors of the SPPs and incident electromagnetic wave are equal and have the same frequency, ω and momentum, $\vec{k}$. A free space photon will have less momentum compared to the SPP because of their distinctive dispersion relations as illustrated by Figure 3.5. The interfaces that support these types of collective excitations are between a conductor and an insulator[153].

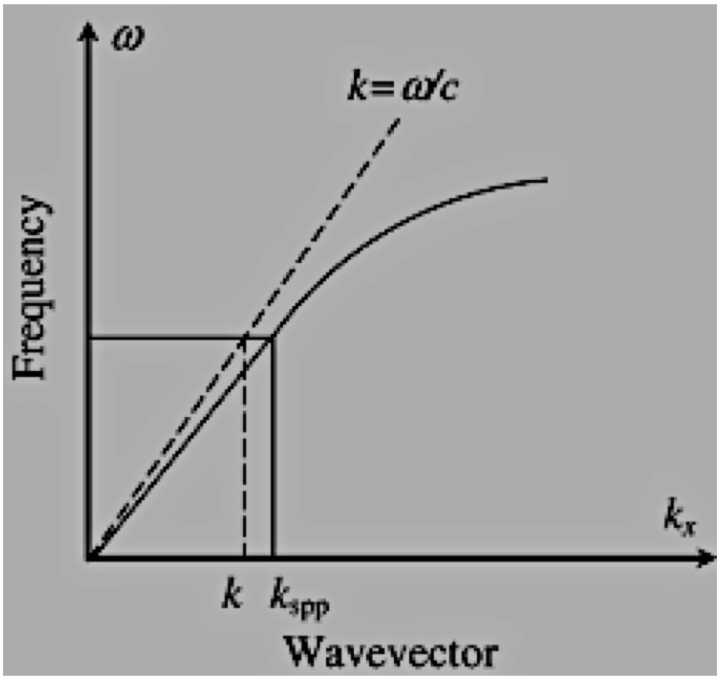

Figure 3.5: An image showing a dispersion curve for SPP[154].

In order to understand this effect, we may use the Drude-Lorentz-Sommerfield model for free electrons, where we have electrons floating around in the lattice and they have some mass, m. We can use one of Maxwell's equations, which contains the electric field[155, 156].

$$\vec{D} = \varepsilon_0 \vec{E} + \vec{P} \tag{3.21}$$

where,

$\vec{D}$ is the dielectric displacement.

ε_0 is the relative permittivity.

$\vec{E}$ is the electric field.

$\vec{P}$ is the electric polarization, which is the net electric dipole per unit volume.

Therefore:

$$\vec{D} = \varepsilon_n(\varepsilon)\vec{E} \tag{3.22}$$

which is the displacement vector for free space.

Writing the equation of motion for a single free electron in free space:

$$m\frac{\partial^2 \vec{x}}{\partial t^2} + m\gamma\frac{\partial \vec{x}}{\partial t} = -e\vec{E} \tag{3.23}$$

The damping term γ is related to the time it takes for the electron to collide with another electron (mean relaxation time) and it is expressed in the following.

$$\gamma = \frac{1}{\tau} \tag{3.24}$$

τ is the mean free time and it can be written as:

$$\tau = \frac{v_F}{l} \tag{3.25}$$

where l is the electron mean free path and v_F is the Fermi velocity.

Assuming that the electron is driven by a periodic force, then we get:

$$\vec{E}(t) = \vec{E_0}e^{-i\omega t} \tag{3.26}$$

Due to the harmonic dependence, we assume a periodic response, i.e.

$$\vec{x}(t) = \vec{x_0}e^{-i\omega t} \tag{3.27}$$

Then, the solution will be.

$$\vec{x}(t) = \frac{e}{m(\omega^2 + i\gamma\omega)}\vec{E}(t) \tag{3.28}$$

e is the electric charge.
ω is the frequency.

Taking the solution of Eq (3.28) and putting it back to the polarization, which can be written as:

$$\vec{P} = -ne\vec{x} \tag{3.29}$$

Thus:

$$\vec{P} = \frac{-ne^2}{m(\omega^2 + i\gamma\omega)}\vec{E}(t) \tag{3.30}$$

From Eq (3.21) and (3.22), we obtain.

$$\vec{D} = \varepsilon_0 \left(1 - \frac{\omega_p^2}{\omega^2 + i\gamma\omega}\right) \vec{E} \tag{3.31}$$

ω_p is the plasma frequency and it gives a scale for the resonance effect. The plasma frequency is represented by the following equation.

$$\omega_p^2 = \frac{ne^2}{\varepsilon_0 m} \tag{3.32}$$

n is the number density of electrons and m is the rest mass of the free electron,

$$\vec{D} = \varepsilon_0 \varepsilon(\omega) \vec{E} \tag{3.33}$$

since, $\varepsilon(\omega)$ is a complex quantity defined in the form,

$$\varepsilon(\omega) = \left(1 - \frac{\omega_p^2}{\omega^2 + i\gamma\omega}\right) \tag{3.34}$$

Then, the permittivity can be expressed in its real and imaginary parts as follows;

$$\varepsilon(\omega) = \varepsilon_1(\omega) + i\varepsilon_2(\omega) \tag{3.35}$$

where the real part is given by,

$$\varepsilon_1 = 1 - \frac{\omega_p^2 \tau^2}{1 + \omega^2 \tau^2} \tag{3.36}$$

while the imaginary term as;

$$\varepsilon_2 = \frac{\omega_p^2 \tau^2}{\omega(1 + \omega^2 \tau^2)} \tag{3.37}$$

The dielectric constant can also be related to the index of refraction in the form,

$$\varepsilon = \tilde{n}^2 \tag{3.38}$$

in which the complex index of refraction is given in its real and imaginary term as,

$$\tilde{n} = n + ik \tag{3.39}$$

where k is the extinction coefficient and n the refractive index. k is mathematically expressed as,

$$k = \frac{\omega}{c} \tag{3.40}$$

c is the speed of light.

The SPPs are obtained from the solution of the electromagnetic wave equation at an interface between a dielectric material having a dielectric constant ε_1 and a conducting material with a dielectric function $\varepsilon(\omega)$. The component of the electric field that is perpendicular to the interface decreases exponentially as the distance from the interface is increased, because of the standard boundary conditions at such an interface. The solution to the wave equation produces the following equation for the dispersion relation for the SPPs[157, 155, 158],

$$\beta = k\sqrt{\frac{\varepsilon(\omega)\varepsilon_1}{\varepsilon(\omega)+\varepsilon_1}} \tag{3.41}$$

β is the component of the wave vector in the direction of propagation of the plasmonic oscillation at the interface. The conditions for the appearance of the SPPs according to Eq (3.41) are that one of the dielectric functions ($\varepsilon(\omega)$ or ε_1) must be negative and greater than the other.

3.3 Localized Surface Plasmonic Resonance

Localized surface plasmonic resonance (LSPR) can be described as non-propagating excitations of the conduction electrons of a metallic nanostructure coupled to an electromagnetic field[157]. When a field incident on a particle interacts with the particle, the atoms inside the particles will oscillate in response to it and in return re-radiate a field that combines with the incident field to produce the scattered field. Some of the energy will be converted into heat and to other forms of energy.

The electrostatic approach can be used to study the properties of localized surface plasmons on metal NPs. This is done by considering a spherical particle with radius a, permittivity $\varepsilon(\omega)$, surrounding dielectric medium with permittivity ε_1 and a uniform electric field $\mathbf{E} = E_0\hat{\mathbf{z}}$ as illustrated in Figure3.6. In order for the extinction in the sphere to be investigated, the electric field in the presence of the particle has to be known. This may be done by solving the Laplace equation for the electric potential Φ inside and outside the sphere. The Laplace equation is given by:

$$\nabla^2\Phi_{in} = 0, r < a \tag{3.42}$$

$$\nabla^2\Phi_{out} = 0, r > a \tag{3.43}$$

The electric field of the sphere will be:

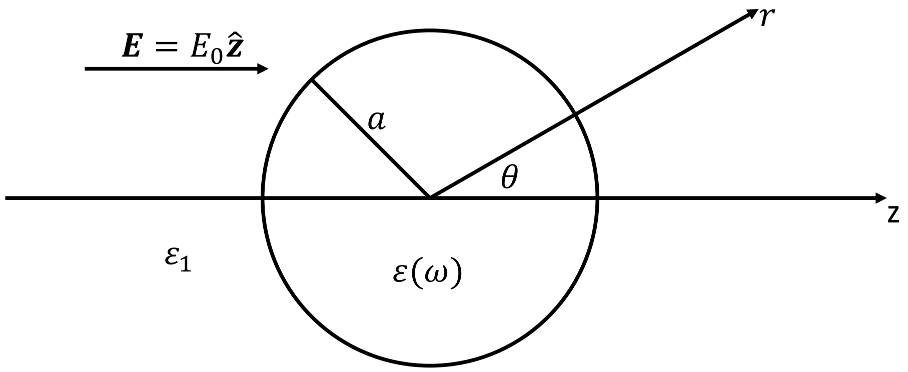

Figure 3.6: A spherical particle of radius a exposed to a uniform electric field **E**.

$$\mathbf{E}_{in} = -\nabla\Phi_{in} \tag{3.44}$$

and,

$$\mathbf{E}_{out} = -\nabla\Phi_{out} \tag{3.45}$$

The Laplace equation inside or outside the sphere may be expressed in spherical coordinates (r, θ, φ) as follows:

$$\nabla^2\Phi(r,\theta,\varphi) = \frac{1}{r^2\sin\theta}\left[\sin\theta\frac{\partial}{\partial r}\left(\frac{r^2\partial}{\partial r}\right) + \frac{\partial}{\partial\theta}\left(\sin\theta\frac{\partial}{\partial\theta +}\right) + \frac{1}{\sin\theta}\frac{\partial^2}{\partial\varphi^2}\right]\Phi(r,\theta,\varphi) = 0 \tag{3.46}$$

Because of the symmetry with respect to the azimuthal angle φ. The solution to Eq (3.46) will be of the form[155, 157],

$$\Phi(r,\theta) = \sum_{0}^{l=\infty}[A_l r^l + B_l r^{-(l+1)}]P_l\cos\theta \tag{3.47}$$

A_l and B_l are real constants. P_l is the Legendre polynomials of lth degree and the potential has to be finite inside the sphere, resulting to the expression:

$$\Phi_{in}(r,\theta) = \sum_{0}^{l=\infty} A_l r^l P_l\cos\theta \tag{3.48}$$

The potential outside the sphere will be,

$$\Phi_{out}(r,\theta) = \sum_{0}^{l=\infty} [A_l r^l + C_l r^{-(l=1)}] P_l \cos\theta \tag{3.49}$$

The three constants A_l, B_l and C_l are determined by the boundary conditions at $r \to \infty$ and at the surface of the sphere $r = a$. Making $\mathbf{E}_{out}(r \to \infty) = \mathbf{E}_0 = -E_0 r\cos\theta$ gives the coefficients $B_l = -E_0$ and $B_l = 0$ for $l \neq 1$[156, 157, 159]. A_l and C_l are described by the boundary conditions at $r = a$. The boundary conditions require the continuity of the tangential components of the electric field and the normal components of the electric displacement field D at the surface of the sphere. They are expressed as:

$$\frac{\partial \Phi_{in}(r=a)}{\partial \theta} = \frac{\partial \Phi_{out}(r=a)}{\partial \theta} \tag{3.50}$$

and

$$\varepsilon(\omega)\frac{\partial \Phi_{in}(r=a)}{\partial r} = \varepsilon_1 \frac{\partial \Phi_{out}(r=a)}{\partial r} \tag{3.51}$$

The application of the boundary conditions to the coefficients A_l and C_l results to $A_l = C_l = 0$ for $l \neq 1$. The remaining coefficients can be calculated by taking into consideration the first two terms in the sum (first order approximation) and the potentials (inside and outside) of the sphere will evaluate to[153, 160],

$$\Phi_{in} = -\frac{3\varepsilon_1}{\varepsilon(\omega) + 2\varepsilon_1} E_0 r \cos\theta \tag{3.52}$$

and

$$\Phi_{out} = -E_0 r\cos\theta + \frac{\varepsilon(\omega) - \varepsilon_1}{\varepsilon(\omega) + 2\varepsilon_1} E_0 a^3 \frac{\cos\theta}{r^2} \tag{3.53}$$

Φ_{out} can be defined as the superposition of the applied field and that of an oscillating dipole field located at the center of the particle. Thus, the dipole moment $\mathbf{p}$ can be introduced into Φ_{out} as follows[156, 157]:

$$\Phi_{out} = -E_0 r\cos\theta + \frac{\mathbf{p}\cdot\mathbf{r}}{4\pi\varepsilon_0\varepsilon_1 r^3} \tag{3.54}$$

and,

$$\mathbf{p} = 4\pi\varepsilon_0\varepsilon_1 a^3 \frac{\varepsilon(\omega) - \varepsilon_1}{\varepsilon(\omega) + 2\varepsilon_1}\mathbf{E} \tag{3.55}$$

Therefore, the applied field induces a dipole moment inside the sphere, proportional to $|\mathbf{E}|$ and the polarizability, denoted by (α), of a metallic sphere is then obtained from Eq (3.53) as[156, 157, 159]:

$$\alpha(\omega) = 4\pi a^3 \frac{\varepsilon(\omega) - \varepsilon_1}{\varepsilon(\omega) + 2\varepsilon_1} \tag{3.56}$$

The distributions of the electric fields are obtained from the electric potentials in Eq (3.44) and (3.45), which gives the electric field inside and outside the sphere as:

$$\mathbf{E}_{in} = \frac{3\varepsilon_1}{\varepsilon(\omega) + 2\varepsilon_1} \mathbf{E}_0 \tag{3.57}$$

and

$$\mathbf{E}_{out} = \mathbf{E}_0 + \frac{3\mathbf{n}(\mathbf{n} \cdot \mathbf{p}) - \mathbf{p}}{4\pi\varepsilon_0\varepsilon_1 r^3} \tag{3.58}$$

n is the unit vector in the direction of point r of interest. The magnetic field for the oscillating fields will amount to[156, 157, 159]:

$$\mathbf{H} = \frac{i\omega}{4\pi}(\mathbf{n} \times \mathbf{p})\frac{1}{r^2} \tag{3.59}$$

The average rate at which electromagnetic energy per unit area is transferred through the surface of a spherical NP is known as the Poynting vector, **S** and it is given by

$$\mathbf{S} = \frac{1}{2}(\mathbf{E} \times \mathbf{H}) \tag{3.60}$$

The boundary conditions applied at the sphere assume that the tangential components of the electric and magnetic field is zero. Thus, the solution for **E** and **H** together with the Poynting vector give the expression for the scattering cross section in the form;

$$\sigma_{sca} = \frac{2\pi}{k^2} \sum_{n=1}^{\infty} (2n+1)(|a_n|^2 + |b_n|^2) \tag{3.61}$$

The coefficients a_n and $b_n$vanishes, since the particles are very small when compared to the wavelength (Rayleigh approximation). Thus,

$$\sigma_{abs} \approx \sigma_{ext} = \frac{k}{\varepsilon_0} \operatorname{Im}[\alpha(\omega)] \tag{3.62}$$

$$\sigma_{sca} = \frac{k^4}{6\pi\varepsilon_0^2} |\alpha(\omega)|^2 \tag{3.63}$$

The effect of particle size, t should determine the relative strength of absorption or scattering cross-sections such that:

for $t >> 0$

$$\sigma_{sca} > \sigma_{abs}$$

and

while for $t \to 0$

$$\sigma_{sca} < \sigma_{abs}$$

Therefore, Eq (3.62) and (3.63) can be expressed as,

$$\sigma_{abs} = 4\pi k a^3 \operatorname{Im}\left(\frac{\varepsilon(\omega) - \varepsilon_1}{\varepsilon(\omega) + 2\varepsilon_1}\right) \tag{3.64}$$

$$\sigma_{sca} = 8\pi k^4 a^6 \left|\frac{\varepsilon(\omega) - \varepsilon_1}{\varepsilon(\omega) + 2\varepsilon_1}\right|^2 \tag{3.65}$$

The scattering cross section can be expressed as follows[156],

$$\sigma_{sca} = \frac{P_{sca}}{I_{inc}} \tag{3.66}$$

where,

P_{sca} is the scattered power.

I_{inc} is the irradiance incidence.

while the absorbed cross section is given as:

$$\sigma_{abs} = \frac{P_{abs}}{I_{inc}} \tag{3.67}$$

where P_{abs} is the absorbed power.

The total energy is the sum of absorption and scattering, which is known as extinction.

Therefore:

$$\sigma_{ext} = \frac{P_{ext}}{I_{inc}} \tag{3.68}$$

The energy of the LSPRs is dependent on the size, type of material used, shape and the dielectric environment.

When taking into account the interband transitions for metallic spherical NPs in the dielectric function for the material of the particle, the optical response of the material (Au/Ag) will have an additional contribution in the dielectric permittivity created by these interband electronic transitions. This additional contribution will be a complex valued interband susceptibility and it is expressed as follows:

$$\chi(\omega) = \chi_1(\omega) + i\chi_2(\omega) \tag{3.69}$$

The susceptibility will modify the optical extinction (absorption and scattering) and contribute to the total dielectric permittivity that is above a definite threshold frequency. $\chi_1(\omega)$ is delocalized on the frequency scale, which widens to zero frequency and the complex term, $\chi_2(\omega)$ is localized to the electron transition frequencies[161].

3.3.1 Size Dependence

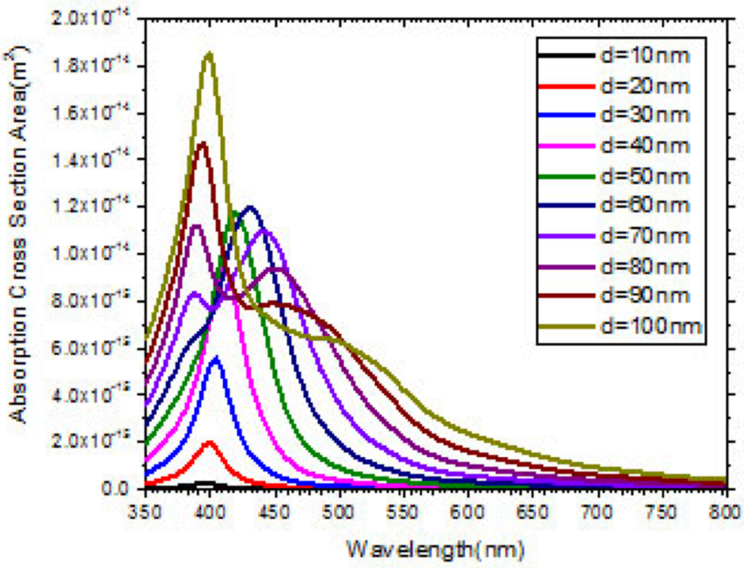

Figure 3.7: An image showing absorption cross section for Ag NPs for varying diameter[162].

Increasing or decreasing the size of the metallic NPs has an influence on the amount of absorption and scattering, which contributes to the amount of extinction. The extinction of large NPs is mostly dominated by scattering while for small NPs, it is dominated by absorption as depicted in Figure 3.7[163, 164]. The effect of the size of NPs have on the extinction can be seen from Eq (3.64) and (3.65). The wave number, k is dependent on the wavelength, λ. Thus,

$$k = \frac{2\pi}{\lambda} \tag{3.70}$$

Therefore,

$\sigma_{sca} \propto \frac{1}{\lambda^4}$ and $\sigma_{abs} \propto \frac{1}{\lambda}$

The change between large and small NPs can be observed by an obvious colour change which depends on the type of NPs. Au and Ag have different absorption bands for the same size. For large NPs, the spectrum for both types of nanoparticles becomes green and for small ones, the red colour is observed[153, 156].

3.3.2 Shape Dependence

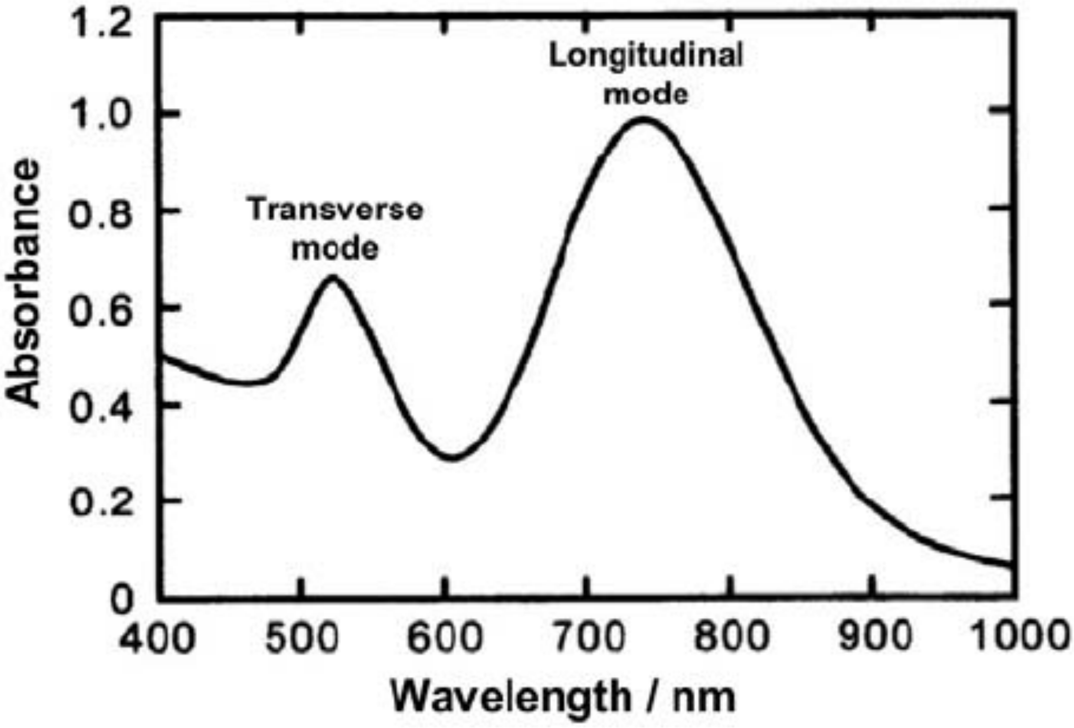

Figure 3.8: An image showing the extinction spectra of Au spheroidal NPs. The 1st peak at 520 nm is the main surface absorption (transverse mode) and the 2nd peak is the longitudinal plasmon resonance mode[165].

The shape of the NP is of great significance for the surface plasmon resonance and it is the basis for the resonance frequency to be redshifted. Different complex shapes have the ability to optimize the localization of the plasmons, accompanied by an enhancement of the field coupled with the LSPRs[163]. The spherical shape for NPs is only limited to reveal a single plasmon resonance, due to its symmetry. Complex shapes often produce multiple plasmon resonances and they can be thought of as the amalgamation of elementary plasmons of simpler shapes[166]. The expressions for scattering and absorption cross sections has to be modified for non-spherical shapes. Multiple resonances exist for different directions of polarization of the incoming field. One of the advantages of having complex shapes of NPs is that the absorption and scattering can occur at different places in the structure. Having shapes that have sharp corners or edges, like triangular or star like shapes, the electromagnetic field intensity is higher in these shapes compared to other simpler shapes[167]. Other non-spherical NPs show remarkable changes, especially elliptical shapes. These shapes exhibit two plasmon resonance absorptions and this modifies Mie's theory to include two contributions of two different dipole polarization modes. The split into two bands is due to the oscillation of electrons perpendicular to a (i) Transverse Mode or along the major (ii) Longitudinal Mode axis of the particle.

The transverse mode exhibits a resonance at about 520 nm (2.4 eV) as shown in Figure 3.8, which coincides with the plasmon band of spherical particles. The other absorption appears to be much stronger due to the longitudinal oscillation of the electrons. The longitudinal mode, which is above 700 nm is red shifted with respect to the transverse plasmon and it depends on the aspect ratio of the NP[168, 165].

3.3.3 Materials of the Plasmonic Nanoparticles

The type of materials used to make NPs also affects the resonance frequency, because different materials resonate at different frequencies. Metals are favourable materials for NPs due to their good properties, such as absorption and scattering. The materials that are most frequently used are gold (Au) and silver (Ag) and recently, the alloying of the two materials is used. Alloying the two materials (Au and Ag) at different quantities will give resonances between the resonances due to pure Ag and Au particles, because Au NPs have a lower resonance frequency than Ag NPs[169, 170]. Resonance absorptions of Au, Ag and Al appear at different places in the EM spectrum. Al plasmonic response is in the UV region, can also extend to NIR region. Ag and Au NPs of different sizes and shapes exhibit good plasmonic response in the visible near infrared region[171, 172]. Au is known to be a good absorber for visible wavelengths, especially for small spherically shaped particles. Absorption of Ag NPs can be enhanced by manipulating their shapes. However, Ag is oxidized easily when it comes in contact with moisture or air. Thus, the probability of an oxide shell forming on the surface of the NP is high and this will decrease optical properties of the particles[173].

3.4 Absorption Mechanisms of Plasmonics

Integrating PV devices with plasmonic NPs leads to the enhancement of electromagnetic energy absorption in semiconductors and also increases the performance of the solar cell. The absorption mechanisms for the improvement of semiconductor devices are based on the following processes:

3.4.1 Electromagnetic field enhancement

The electromagnetic field incident on the NPs, having a frequency ω, will be absorbed by the metallic NPs which act as subwavelength antennas. The fields emitted by the NPs are highly concentrated in the near field of the plasmonic, which is coupled to the active layer of a PV device. Embedding the plasmonic NPs closer or within the active layer leads to higher absorption in the vicinity of the active layer, due to the near field concentration. When the photons travel a longer distance down from the top of the PV cell into the absorbing layer of the PV cell, the attenuation properties of the material will decrease the intensity of the photons. Light usually escapes the Si solar cells before being adequately absorbed and having NPs will help with the absorption, before all the photons are lost to the device[83, 174, 175, 176].

3.4.2 Light scattering into the active layer

The electromagnetic wave that is incident on the device will interact with the NP and the wave that will be transmitted by the NP will have components moving in the tangential direction of the incident wave[174, 177]. Locating the NP close to the active layer will transmit the incident waves at non-normal angles and the incident light will be scattered into the semiconductor, because the semiconductor has a greater permittivity[178]. The photons will be scattered again by the back contact metal, this will happen up to the critical angle of $\approx 16°$ between the Si interface and the absorbing layer. If the transmitted wave impinges at an angle greater than the critical angle of the active layer, the photons will be absorbed. The reflected light from the back contact will be scattered into the active layer[179, 82, 180].

3.4.3 Formation of electron-hole pairs in the NPs

LSPRs on metal NPs can create electron-hole pairs in Si based PV cells by emitting the energy of a plasmon in the directions along the semiconductor. This increases the probability of optical absorption and effective optical path of the light. The electron-hole pair can also be formed from the excitation of the near field of the plasmon and this preserves the conservation of momentum through a resonant energy transfer to the NP[157]. The work function of the NPs must be the same as that of the semiconductor's conduction band and there will be a high probability of the created electron to be transferred to the semiconductor's conduction band[181].

Chapter 4

4 Methodology

This section presents a brief description of methods used to fabricate thin films and the characterization techniques to investigate the film properties. The essential growth technique (Radio Frequency magnetron sputtering) is examined with regards to the deposition of hydrogenated (a-Si:H) and non-hydrogenated (a-Si) thin films on a glass/ITO substrate. The measurement techniques utilized in the optical, structural and electrical characterization are discussed. Commercial a-Si solar cells of size 50 mm by 25 mm were purchased from MR WATT shop based in Italy.

4.1 Radio Frequency (RF) Magnetron Sputtering Technique

Sputtering is a deposition technique that is extensively used in the thin film industry. The sputtering technique is a physical vapour deposition (PVD) that mainly depends on the bombardment of a target by ions in the plasma as depicted in Figures 4.1a and 4.1b. The target is bombarded by energetic ions that are created by the ionization of a working gas (Ar) under an applied voltage. The ionization of the Ar gas leads to plasma ignition, which is the source of Ar^+. When the silicon target is bombarded, it will eject atoms of the silicon target and they will float and condense on the glass substrate.

Compared to other deposition methods, sputtering does not involve chemical interaction between the species. When the silicon target is bombarded with energetic ions, it will release equally energetic atoms that condense on the substrate to form a film. The constant flow of source material deposited promotes film growth and it also improves the film characteristics. The advantage of using sputtering is that it can be used at very low temperatures, even at room temperatures to grow good quality films. Thus the hydrogenated amorphous silicon can be grown at temperatures <500 $°C$, because at temperatures >500 $°C$, the silicon crystallizes. The advantages of depositing silicon are[183]:

1. No toxic or hazardous gasses are involved in the process.
2. The amount of Hydrogen fused into the deposited film can be manipulated.
3. The process temperature can be reduced.
4. The silicon target can be doped before or after it is sputtered.

The sputtering process can be catergorized into DC or RF depending on the type of power supplied. DC sputtering is mainly used to deposit conducting targets and RF is more suitable for semiconductor and insulator targets. The frequencies that are normally used for RF are in the range of 5 to 30 MHz, but the preferred frequency is 13.56 MHz for RF sputtering. The major difference between DC and RF sputtering is that in the RF system, the power supplied to the chamber is less compared to the power supply in the DC system[184, 185].

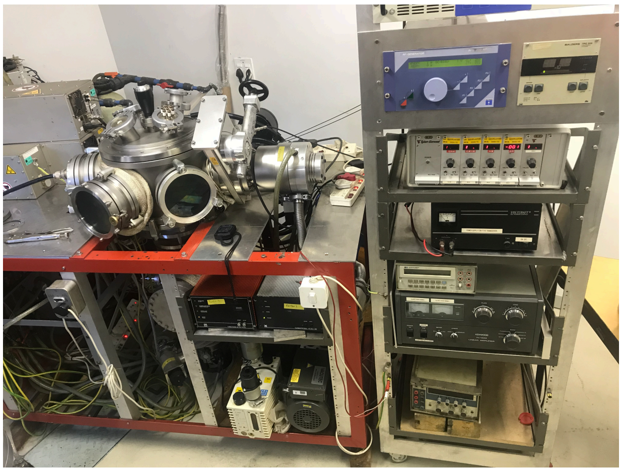

(a) Experimental set-up of the RF Magnetron Sputtering.

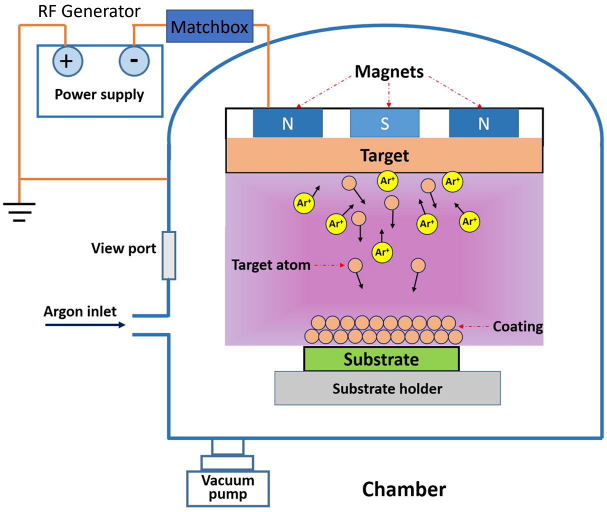

(b) Schematic diagram of RF Sputtering[182].

Figure 4.1: Images showing the experimental set-up (a) and the schematic diagram of the mechanism for the RF magnetron sputtering system (b).

The vacuum chamber is evacuated by a rotary pump to a pressure of 10^{-2} mbar. The turbo pumps are switched on in order to reduce the pressure to 10^{-5} mbar and this is to ensure that the plasma can be ignited in an O_2 free ambient, also to sustain the discharge and to clear any contamination inside the chamber. When the vacuum reaches a specific point, electrically neutral Ar atoms will be introduced into the self-bias chamber. Applying the RF power to the target will lead to the creation of a DC voltage between the substrate and the target. A field will be created by this DC and accelerates free electrons already in the vacuum chamber. Inside the chamber, the Ar atoms will collide with the accelerating electrons and if the collision is inelastic, then the plasma also known as glow discharge will be formed.

The ions created will collide with the surface of the cathode target, which is held at negative voltage. There will be enough energy, due to the collision, to break the bonds of the atoms of the target material (Si) and sputter the Si atoms. The sputtered atoms will move in a straight line perpendicular to the substrate and get scattered by the Ar atoms inside the vacuum chamber. These physically ejected atoms will move some distance before condensing on the substrate to form a film. The damage of the film is minimized by a built in magnetic field that is closer to the Si target which spirals the electrons along the magnetic flux lines next to the target. The location of the magnets being near the target increases the probability of more Ar atoms being ionized. The plasma created will have more ions and this increases the working efficiency of the sputtering system. The sputtering rate is proportional to the deposition rate, the deposition rate increases when the ions are ejected at a faster rate. The deposition rate can be defined as the amount of the material deposited on the substrate at a certain time and it is proportional to the sputter yield, which is defined as the amount of atoms released from the target for every incident Ar ion[186, 187].

4.1.1 Deposition procedure

The glass substrate was cleaned with acetone and dried by using Nitrogen gas. The sputtering chamber was opened, so that the target (Si), which has to be deposited on glass, can be mounted inside the chamber. The magnetic valve was switched on in order to evacuate the chamber followed by the switching on of the rotary pump to ensure the baffle valve that isolates the chamber from the turbo pump is fully open to increase the conductance and efficiency of the pump. The system's pressure decreased to 10^{-2} mbar, which takes about 30 minutes and the pressure was decreased further by switching on the turbo pump until it reached a pressure of 10^{-5} mbar. The gas tanks were open and the pressure in the baffle valve was increased to enhance continuous Ar ionization to sustain glow discharge. This ensures that the electron mean free path is equal to the Ar interparticle/molecule distance. The voltage was adjusted while the sample was away from the target and pre-sputtered for 3 minutes at a power of 100 W. The sample was rotated to face the target and Si was deposited for a certain amount of time and power. After depositing Si, the voltage was slowly reduced and switched off along with the pressure gauge and the two pumps.

4.2 Thermal Evaporation

The thermal evaporation technique is a physical vapour deosition process that involves the heating of a solid material at high temperatures. The evaporated material condenses to form a film on the substrate, which is positioned above the evaporation site. Thermal evaporation was primarily used for the deposition of NPs which has the following advantages[189]:

- The process is the least expensive compared to other PVD processes.
- The material that is evaporated will be deposited in pure solid form on the substrate.
- The deposition rate is easily monitored and controllable.

The thermal evaporation technique uses low pressures (10^{-5} mbar) because the filament can only be excited through an evacuated chamber. The solid is vaporized by heating the material at high temperatures. The material's particles diffuses vertically

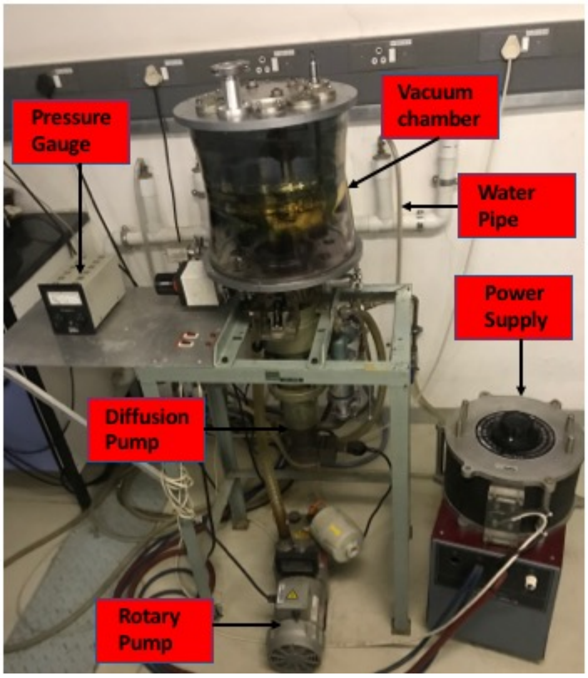

(a) Experimental set-up of the thermal evaporation system.

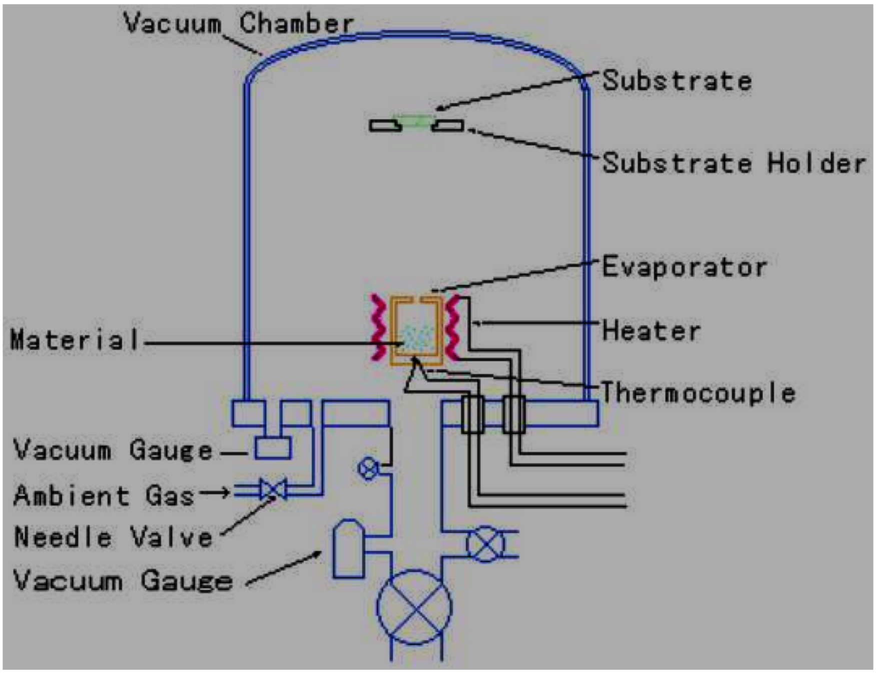

(b) Schematic diagram of the thermal evaporation system[188].

Figure 4.2: Images showing the experimental set-up (a) and the schematic diagram of the mechanism for the thermal evaporation system (b).

upwards from the evaporation source and condenses at a cooler substrate located a distance away above the material. The vaporized molecules should have an average kinetic energy lower than the binding energy of the material. When the atoms reach the surface of the substrate with low energy, the film deposited will be more homogeneous as the particles will be equally distributed. The deposition rate and the thickness of the deposited film are measured by a quartz crystal monitor[190, 191]. The thermal evaporation set-up used in this work is presented in Figures 4.2a and 4.2b.

4.2.1 Deposition procedure

The Bell glass jar of the chamber was cleaned and the substrate mounted in a perpendicular position at 70 mm from the deposition source. The chamber was assembled to ensure that the O-rings of the lid and base is well aligned for a good seal. The vent (angle valve) was closed and the rotary pump to the vacuum chamber was open. The vacuum gauge and rotary pump were turned on to evacuate the chamber for 30 minutes. This ensures that the chamber approaches a roughing pressure of 10^{-2} mbar. The valve between the rotary pump and the vacuum chamber was closed. The pressure took 2 - 3 hours to reach between 10^{-5} and 10^{-6} mbar. When the highest vacuum was reached, the shutter was positioned to block the vapour source, the power supply was turned on and the voltage was slowly adjusted to desired power (V=70 V and I=200 A). The vapour source was unblocked by turning the shutter away and deposition took place for a desired time. After deposition, the shutter was closed and the voltage was slowly dropped before turning off the power supply. The chamber from the diffusion pump was closed and the power of the diffusion pump was turned off. It took 2 hours for the diffusion pump to cool down and the throttle valve between the bottom and the chamber above it, was closed. The vacuum chamber to the rotary pump was opened, the water flow and the rotary pump were turned off. The chamber was vented by the angle valve to atmospheric pressure to remove the sample from the chamber.

4.3 Ion Implantation

In order to control the amounts of dopants into semiconductors, two processes can be used, namely ion implantation and diffusion. The process used here was ion implantation. Ion implantation involves the incorporation of energetic dopant ions into the semiconductor using a high energy ion beam. The ion beam is generated by a filament which emits electrons and they are accelerated to acquire sufficient energy for the implantation. The electrons collide with the atoms or molecules and ionizes them. The ions are extracted and accelerated towards the magnet for mass/charge selection. The magnet will bend the ion beam through a right angle to select the desired species, as shown in Figure 4.3b. The advantages of using ion implantation to dope thin film solar cells are[86]:

- The process can be done at low temperatures (room temperature).
- The process offers high dopant profiles and doses.
- The ions implanted can be patterned.
- The repeatability and uniformity are high in this process.
- Depth sensitivity.

For this work, the plasma source ion implanter illustrated in Figure 4.3a was used. The key parameters used to implant Al, B and P ions in Si are given in Table 4.1

(a) Experimental set-up of the 1.4 MeV Cockcroft-Walton ion implanter.

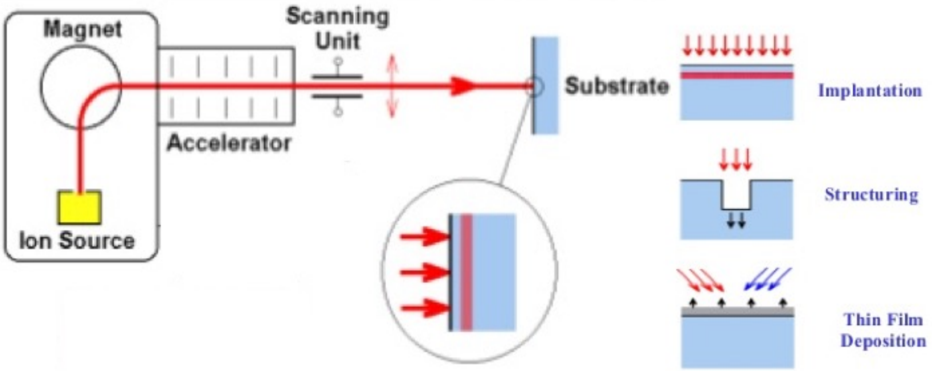

(b) Schematic diagram of the ion implanter.

Figure 4.3: Images showing the experimental set-up (a) and the schematic diagram of the mechanism for ion implantation (b).

Table 4.1: Table showing ion implantation conditions. The implantation was done at room temperature.

Element	Beam Energy (keV)	Fluence ($ions/cm^2$)	Implantation time (hours)
Al	20	3×10^{15}	2
B	20	2.3×10^{14}	1.5
P	20	9×10^{16}	3

The chemical element for doping the Si layer was placed at the ion source and the ions extracted from it. This source can be either in gaseous or solid form. These ions will be deflected as a result of the magnetic field that is dependent on the charge/mass ratio. The ions will then be accelerated and implanted to the target (thin film). They will lose energy by colliding with the nuclei or electrons of the sample. The implant doses and energies used in this process are simulated by Stopping and Range of Ions in Matter (SRIM) computer program. The implant dose is defined as the number of ions implanted per unit area. The amorphization of the layer is dependent on the fixed energy and the ion dose. In order for the doped layers to remain amorphous, the beam energy must be roughly 20 keV and the ion dose must be $\geq 10^{16}$ $ions/cm^2$[192].

4.3.1 SRIM Software

The SRIM computer software was used to perform Transport of Ions in Matter (TRIM) Monte Carlo calculations to predict implant distribution, radiation damage and collision details of the recoil atoms creating implant ions[193]. The SRIM software was also used to simulate the beam energies and the doses for n-type and the p-type Si in a layer thickness of 20 nm. Different thicknesses were compared to different beam energies and the distribution of ions inside the thin film were taken into account by these simulations. The simulations also takes into account the increasing ion dose with the crystal structure dynamic modification.

4.4 Layer Thickness Optimization

The thickness of the sputtered layers can be determined by using three methods. One of the first method is to create a step in the coating by covering a small fraction with a tape and this tape has to be removed from the sample after the deposition is done and a surface profilometer can be used to measure the step edge. The second method for determining the layer thickness is by using a scanning electron microscope (SEM) and the third method is using X-ray reflectometry. In these two methods, different glass pieces with deposited silicon layers are broken in order to generate a cross section for the thickness measurement[194].

The thicknesses for the project of each sputtered layer is determined by using a technique similar to the first method using a profilometer. The conditions for depositing different layers of Si on glass are shown in Table 4.2

Table 4.2: Table showing conditions of sputtered layers.

Process	Power (W)	Ar gas (sccm)	Deposition time (min)	Film Thickness (nm)	Deposition rate (nm/min)
1	100	20	10	288.9	28.89
2	75	20	20	204.3	10.215
3	120	20	20	331.8	16.59
4	100	20	20	340.2	17.01
5	75	25	20	173.9	8.695

The thickness is found by measuring the distance between the two step edges using a surface profilometer. Once the thickness of each of the samples is known, the deposition rate can be calculated from the linearity of the film thickness with deposition time. Therefore, any desired film size can be deposited using any conditions from the five samples. The conditions for process 5 were used to deposit the three layers (p-i-n) of an a-Si:H PV for any desired length. The higher Ar gas flow rate was used to minimize residual stresses in the film which could lead to delamination of the films.

4.5 Architecture of a-Si:H Device

The fundamental device configuration inside a-Si:H cells consist of three layers that are deposited in either the p-i-n or n-i-p sequence. The p and n layers are the doped 20 nm a-Si thin films. The i-layer, which is also known as an intrinsic layer is the active layer for generating photocurrent (electron-hole) in the cell, where excitons are split to form charge carriers. The i-layer is a significant layer in a-S:H solar cells. The p-i-n sequence implies that the p-layer is deposited first, then the i-layer is the second layer deposited and the n-layer is the last one to be deposited on the substrate[41]. The n-i-p configuration is chosen when stainless steel or any other non-transparent material is used as a substrate and the p-i-n deposition sequence is chosen if glass or any other transparent material is used as a substrate[38]. The three layers are very thin, the thicknesses of the p-layer are typically 10 - 20 nm, for the n-layer, they are typically 20 - 30 nm. For

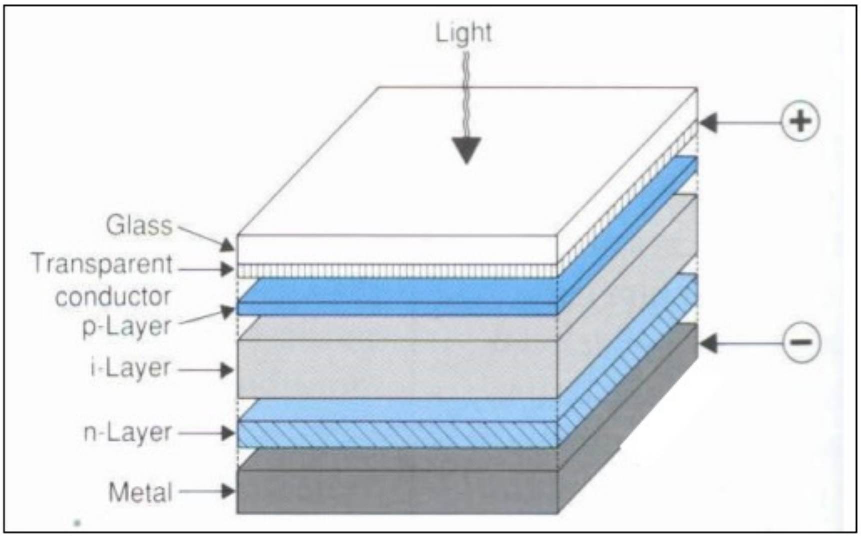

Figure 4.4: An image showing the structure of a standard a-Si:H solar cell[41]

the intrinsic layer, the thickness is bigger compared to the two layers, which is typically 300 - 500 nm[195]. The rationale for the large value of film thickness of the i-layer is to collect the maximum number of electron-hole pairs generated by photoabsorption because this process is dependent on the film thickness, also on the optimal compromise between the electrical properties (series resistance) and optical absorption. In addition to the three layers, a layer of Transparent Conducting Oxide (TCO) which acts as an anode (top electrode) and a metallic material as a rear electrode are added to the device due to their differences in work functions. The TCO is deposited on top of the p-layer and has a thickness of around 20 nm. A rear electrode is after the n-layer. The best choice for a TCO is Indium Tin Oxide (ITO) because of its good electrical conductivity and optical transparency, especially in the visible region of the spectrum. For a rear electrode, aluminium (Al) and Ag are the most popular materials used[38, 196].

When ITO was used as a substrate, the p-i-n deposition sequence was used, as shown in Figure 4.4. The thickness for the p and n layer was chosen to be 20 nm, and for the i-layer, it was set at 300 nm. These values were taken from the literature according to the work of Pawlewicz et al., 1978[197].

4.5.1 Fabrication of the p-type a-Si Layer

The p-type layer should be non-absorbing and really thin, this is because the i-layer has to absorb maximum photons transmitted by the p-type layer and this can be seen in the transmission spectra in Figure 4.5. The p-type was the first layer deposited on the conducting side of the ITO. It was sputtered for 2 minutes and 18 seconds by using deposition conditions for process 5 in Table 4.2.

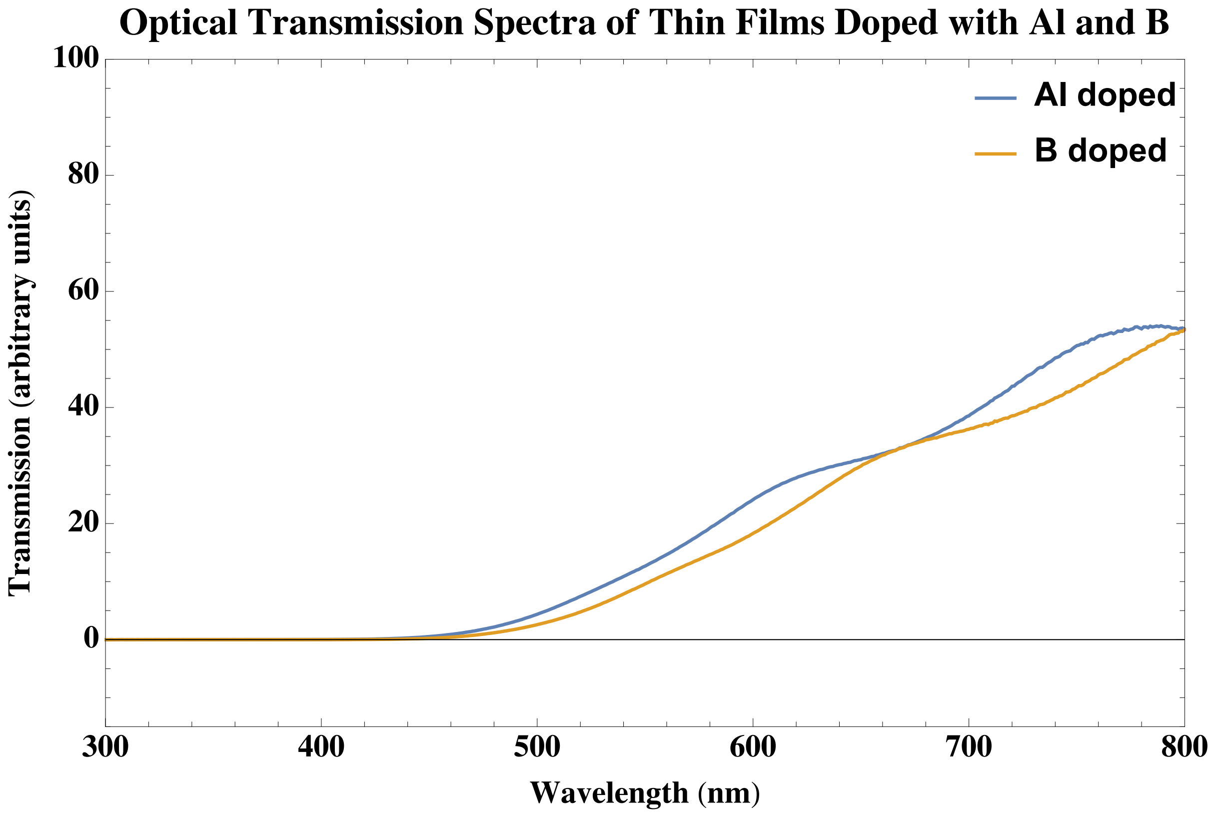

Figure 4.5: An image showing transmission spectra of p-doped layers. The layers were doped with Al and B.

4.5.1.1 P-type doping

The electrical properties of this layer can be manipulated by adding impurities that form a semiconductor with holes as the major carriers. The element implanted in the layer was Al and the Al ions were implanted at a beam energy of 20 keV with a dose of 4×10^{15} $ions/cm^2$ for 2 hours. Boron (B) was also used to form a p-type layer. Boron ions were implanted at a beam energy of 20 keV with a dose of 2.3×10^{14} $ions/cm^2$ for 1 hour and 30 minutes.

4.5.2 Fabrication of the i-type a-Si:H Layer

The i-layer is supposed to be thicker than the two layers, because it should be able to absorb more photons without trading off the electrical properties of the entire device. The i-layer is the second layer deposited after the 20 nm p-layer on the ITO. It was deposited using process 5 conditions in Table 4.2, except this time a gaseous mixture of Ar and H was used. The composition of the H_2 in the mixture was 4% and the mixture of the two gases increases optical absorption in the layer[197, 38]. The time for the deposition was optimized to 34 minutes and 30 seconds to yield 300 nm thin a-Si:H films.

4.5.3 Fabrication of the n-type a-Si Layer

The function of the 20 nm n-layer is to create a built in electric field between the two doped layers due to their differences in chemical potential and allow for the extraction of the charge carriers (electrons and holes). It is also the thinnest layer of the device, so that the unabsorbed photons can be transmitted to the back electrode and be reflected back to the i-layer. The n-type was the third layer deposited on the ITO and it was deposited after the i-layer. It was sputtered for 2 minutes and 18 seconds by using deposition conditions for process 5 in Table 4.2.

4.5.3.1 N-type doping

The element implanted in the layer was phosphorus (P) and the P ions were implanted at a beam energy of 20 keV with the dose of $9 \times 10^{16}\ ions/cm^2$ for 3 hours.

4.5.4 Fabrication of the Metal Contact Layer

The purpose of this layer is two fold; firstly this layer reflects photons that were not absorbed by the i-layer back to the i-layer. Secondly, the metallic layer is used to provide the field needed to collect the electrons. Thus, it functions as a cathode. The materials that are mostly used in the literature are Ag and Al. However Al is preferred over Ag, because Ag has a higher work function than Al and this causes electromigration in the device. The thickness of this layer should be thicker than the n and p-type layers. The thickness of this layer, which is 200 nm, was chosen based on the work of Derkacks et al., 2006[80]. The sputtering conditions were 100 W, Ar gas of 25 sccm. The deposition time for 200 nm was 29 minutes and 15 seconds. These sputtered conditions were based on the work of Alkoy et al., 2005[198].

4.6 Synthesis of Ag and Au NPs

The metal NPs were made using two different PVD processes, which are thermal evaporation and RF Magnetron sputtering. The Ag nanoparticles were sputtered using the conditions shown in Table 4.3. These conditions were selected from the work of previous co-workers Ranganathan et al., 2015[199]. The incorporation of Ag NPs using these conditions in organic PV cells increased the efficiency of the device from 0.5% to 1.4%.

Table 4.3: The Sputtering conditions for the deposition of Ag Nanoparticles

Process	Power (W)	Ar gas (sccm)	Deposition time (s)
1	10	20	10
2	10	20	20
3	10	20	30

The Au NPs on the other hand were produced by thermally evaporating Au pellet on a Mo boat. The conditions for the fabrication of Au NPs are shown in Table 4.4

Table 4.4: Thermal evaporation conditions for the deposition of Au Nanoparticles

Process	Voltage (V)	Current (A)	Deposition time (s)
1	70	200	90
2	70	200	120

4.7 Optical and Morphological Properties of a-Si:H Layers

The optical properties of each layer in the a-Si:H solar cell was analyzed by using a UV-Vis NIR-500 Cary Spectrometer, and the morphological properties were characterized with a Zeiss Sigma Field Emission Scanning Electron Microscopy (SEM). The former was utilized to analyze the absorption and transmission of the each layer in the device including the Ag and Au NPs. From the SEM, morphological information regarding the nanoparticles size, shape and composition were obtained.

4.7.1 UV-Vis Spectroscopy Analysis

The photons incident on any material can be characterized by absorption, reflection and transmission in the UV-Vis spectral region. The amount of light that can be absorbed or scattered by the material is dependent on the material's surface topography and composition. The detection of colours in the sample affects the absorption measurements in the visible range of the spectrum, and this is because of the electronic interband transitions[200]. Transmission should dominate in the two doped layers, absorption should dominate in the i-layer and there should be more reflection in the back rear electrode. All of these processes should occur over wide ranges of wavelengths. The measurements were accomplished by the UV spectroscopy set to measure between 200 - 800 nm. Baseline calibration was carried out for transmission and absorption for 0% and 100% transmission for the double beam method.

4.7.2 SEM Analysis

The chemical or elemental analysis for the SEM sample can be determined by an analytical tool known as Energy Dispersive X-ray Spectroscopy (EDX, EDS, or XEDS). This technique of analysis is dependent on the electron beam's interaction with the sample. This interaction produces the X-ray characteristics of the chemical composition of the sample area that is irradiated. These X-ray characteristics will be shown as a measurement of a unique set of peaks in the X-ray spectrum[201].

4.8 Growth of $ZnO : Tb^{3+}$ Thin Films

ZnO doped with Tb^{3+} was used as a spectral down conversion (DC) layer on the a-Si commercial solar cells. The reason for applying $ZnO : Tb^{3+}$ as a DC layer is because, ZnO is a direct and wider bandgap semiconductor (about 3.37 eV at room temperature)[202]. This makes the ZnO layer to be a suitable material for photonic and optoelectronic applications in the UV-blue spectral range. The bandgap of the ZnO layer can be increased by doping it with one of the rare earth (RE^{3+}) ions. For this project, Tb^{3+} ions were used as a dopant to the ZnO layer. When the layer of $ZnO : Tb^{3+}$ is deposited on the front of the solar cell, this will increase the absorption of photons incident on the device, resulting in increasing the photocurrent of the PV device[203, 204, 205].

The $ZnO : Tb^{3+}$ down conversion layer was deposited on top of the commercial a-Si PV devices by using RF magnetron sputtering. The sputtering conditions used here were based on the work of Otieno et al., 2018[206]. Rutherford Backscattering Spectroscopy (RBS) confirmed that there is a presence of Tb^{3+} in the thin film by using their sputtering conditions. The increased emission of light in the resonance wavelength leads to increased photon intensity to be absorbed by the active layer since absorption in the DC layer means loss of photons to the active layer. The work resulted in the enhancement of the OPV device performance when the $ZnO : Tb^{3+}$ layer was used as a DC layer and as a buffer layer. The $ZnO : Tb^{3+}$ layers were deposited on the a-Si commercial devices at an RF power of 100 W and an Ar gas flow of 13 sccm. The $ZnO : Tb^{3+}$ layers were grown on top of the PV devices for 2 minutes and 5 minutes[131, 206].

4.8.1 Incorporation of Ag and Au NPs in $ZnO : Tb^{3+}$ Layer

The Ag and Au NPs were deposited on the commercial a-Si solar cells with $ZnO : Tb^{3+}$ layers using sputtering conditions in Table 4.3 and Table 4.4. Process 1 in Table 4.3 was applied in the PV cell with $ZnO : Tb^{3+}$ layer deposited for 5 minutes and process 2 in Table 4.4 was applied in the PV cells with $ZnO : Tb^{3+}$ layer deposited for 2 minutes and 5 minutes, respectively.

4.8.2 Annealing of PV Cells with Spectral Layers and NPs

Thin films are amorphous and thus have structural defects that lead to photoluminescence (PL) emission. The presence of these luminescent defects results in the reduction of light emission efficiency. Annealing can reduce the number of defects and thus defect emission in the visible range, and preferentially allow Tb^{3+} emission to contribute to the DC process. ZnO on its own possess a diversity of intrinsic defects which provide visible emission from blue to IR and Tb ions provide strong absorption bands in the UV blue spectral range and a high emission in the green spectral range. In order for the $ZnO : Tb^{3+}$ layer to have greater light emission efficiency, the ratio of the intrinsic and extrinsic defects in the $ZnO : Tb^{3+}$ has to be even[207, 208]. The emission spectrum and the luminescence efficiency of the layer can be manipulated by controlling the defects. This can be achieved by annealing the commercial devices (a-Si) with $ZnO : Tb^{3+}$ layers at certain temperatures and this temperatures must not exceed 500 $^{\circ}C$, as temperatures above 500 $^{\circ}C$ will crystallize the a-Si solar cells[209]. Commercial devices (a-Si) were annealed at a temperature of 150 $^{\circ}C$ for 1 hour with a ramping temperature of 10 $^{\circ}C$/min.

This annealing conditions were also used in the PV cells with $ZnO : Tb^{3+}$ layers and Ag/Au NPs.

4.9 I-V Characterization

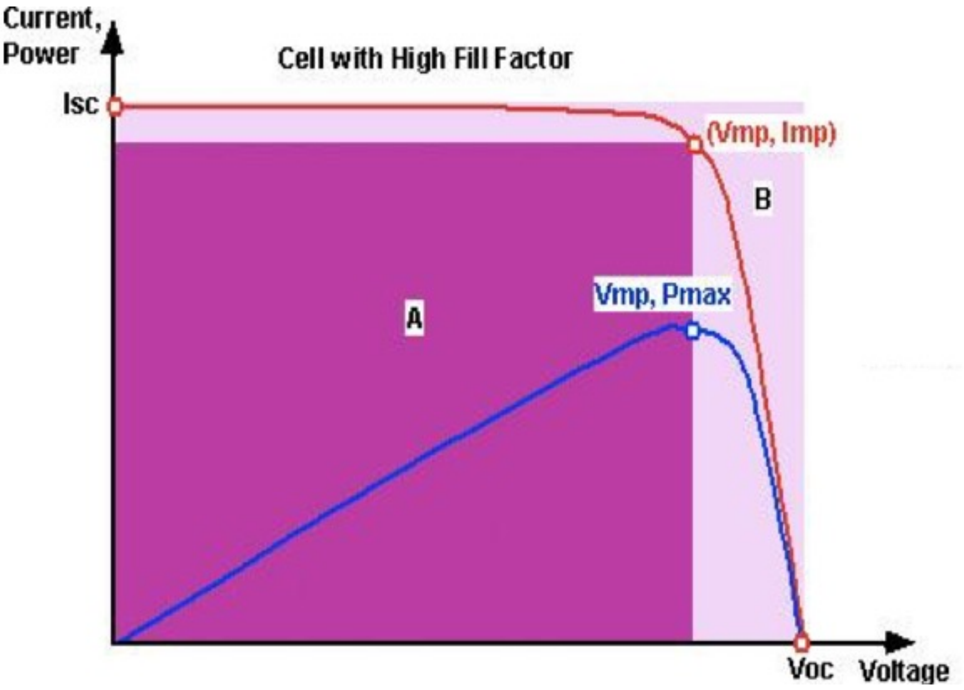

Figure 4.6: An image showing the I-V curve of a solar cell

The current-voltage (I-V) characteristic is an important type of measurement in solar cells, as it gives the electrical properties as a result of the photoresponse of the PV device. The short-circuit current (I_{sc}) and the open-circuit voltage (V_{oc}) are the maximum current and voltage, for a given solar cell as shown in Figure 4.6. Once the I-V curve is obtained, then a lot of important device properties can be calculated including the fill factor (FF) and the efficiency(η). The fill factor is defined as the measurement of how efficient electrons and holes are generated in the device as a function of voltage. The photo-conversion efficiency (η) is the ratio of the power output to the input power measured at a reference standard AM 1.5. FF and η can be mathematically expressed as:

$$FF = \frac{V_{mp} I_{mp}}{I_{oc} I_{sc}} \tag{4.1}$$

and

$$\eta = \frac{P_{out}}{P_{in}} = \frac{(V_{mp})(I_{mp})}{P_{in}} \tag{4.2}$$

V_{mp} and I_{mp} are the voltage and current at maximum power respectively.

Equation (4.2) is basically the ratio between electrical power that is generated by the solar cell vs. the incident light power of the sun[70, 210].

The I-V data is collected by connecting probes to the anode and the cathode of the device or substrate and the voltage will be swept while measuring the current. We used an HP 4141B Source Measuring Unit (SMU) that supplies voltage sourcing and measurement resolution at or lower than 1 mV, also the current sourcing and measurement resolution lower than 1 μA. The SMU is connected to a computer which includes a software known as LabView that captures data. This software outputs a voltage in order to control the amount of current sink and current that can flow in the circuit. Therefore, the I-V curves of the device or sample will be generated in the software by collecting a certain number of points in evenly spaced intervals from the starting voltage at the same time measuring current.

The a-Si commercial solar cells electrical characteristics were also analyzed using dark I-V measurements using the HP 4141B SMU system without the solar simulator. Thus the information regarding the I_{sc} is not provided, but other parameters, such as shunt resistance and series resistance are determined by these measurements. The Mott-Gurney law could be employed to determine the mobility of the charge carriers since in the framework of dark I-V measurements, the charge carriers are injected in the solar cell by an applied electrical field, only.

Chapter 5

5 Results and Discussion

In this chapter, the discussion on the I-V characteristics of the doped Si layers is presented with a determination of the Schottky barrier formed after annealing the doped layers below the recrystallization temperature of a-Si. The optical properties of these layers are presented and analyzed in detail. Additionally, the I-V characteristics of commercial a-Si devices with NPs and spectral conversion layers are analyzed and discussed in detail.

5.1 Schottky Barrier Analysis

The undoped layer of a-Si with a thickness, t of 20 nm was deposited on a glass substrate and contacted using an Ag electrode. Two undoped layers were produced, one of them was implanted with P ions and the other with Al ions. The doped samples were also annealed at 300° C for 20 minutes, because the semiconductor gets damaged by the radiation due to implantation. This damage to the semiconductor is attributed to the energy and the mass of the bombarding ions. After these samples were contacted with an Ag thin film as an electrode, the I-V characteristic curves were measured at room temperature and several parameters were obtained from these plots. The values of the physical constants used to calculate the key parameters of the metal-semiconductor (n and p-type) contacts are listed in Table 5.1:

Table 5.1: Table showing physical constants used to determine key parameters of metal-semiconductor contacts[86].

Constants	Symbol	S.I Units
Richardson Constants for extrinsic Si	A^*	120 A/cm^2K^2
Richardson Constants for electrons in Si	A_n^*	117.6 A/cm^2K^2
Richardson Constants for holed in Si	A_p^*	117.6 A/cm^2K^2
I-V characteristics operating temperature	T	300 K
Electronic charge	e	1.60218×10^{-19} C
Applied voltage	V	0.1 V
Boltzmann constant	k_B	1.38066×10^{-23} J/K
Area of the film	A	0.25 cm^2

5.1.1 I-V Characteristics of the Metal-Semiconductor Contacts

The I-V curves of the n and p-types a-Si in contact with a metal are plotted in Figure 5.1 and 5.2. From the data obtained, important parameters can be extracted, such as the Schottky barrier height (ϕ_B), saturation current density (J_s), barrier width (x), electric field (E), contact (R_c) and sheet (R_s) resistance. The behaviour of the curves reveal a strong doping dependence when dopants such as Al and P are implanted into the a-Si layer, the curves become rectified rather than ohmic as the dopants are added to the thin film a-Si layer. The curves are also temperature dependent.

Note that when the semiconductor is implanted with energetic ions, some of the regions in the semiconductor will be damaged. This damage is due to the energy of and by the mass of the implanted ions. The parameters of the semiconductor, such as carrier lifetime and mobility will be reduced. Thus, results in extended defects during subsequent thermal processing, and they act as scattering centres for the the charge carriers. In order for the semiconductor parameters to be restored and for the implanted ions to be activated, the semiconductor has to be annealed at an appropriate temperature and time[86, 142].

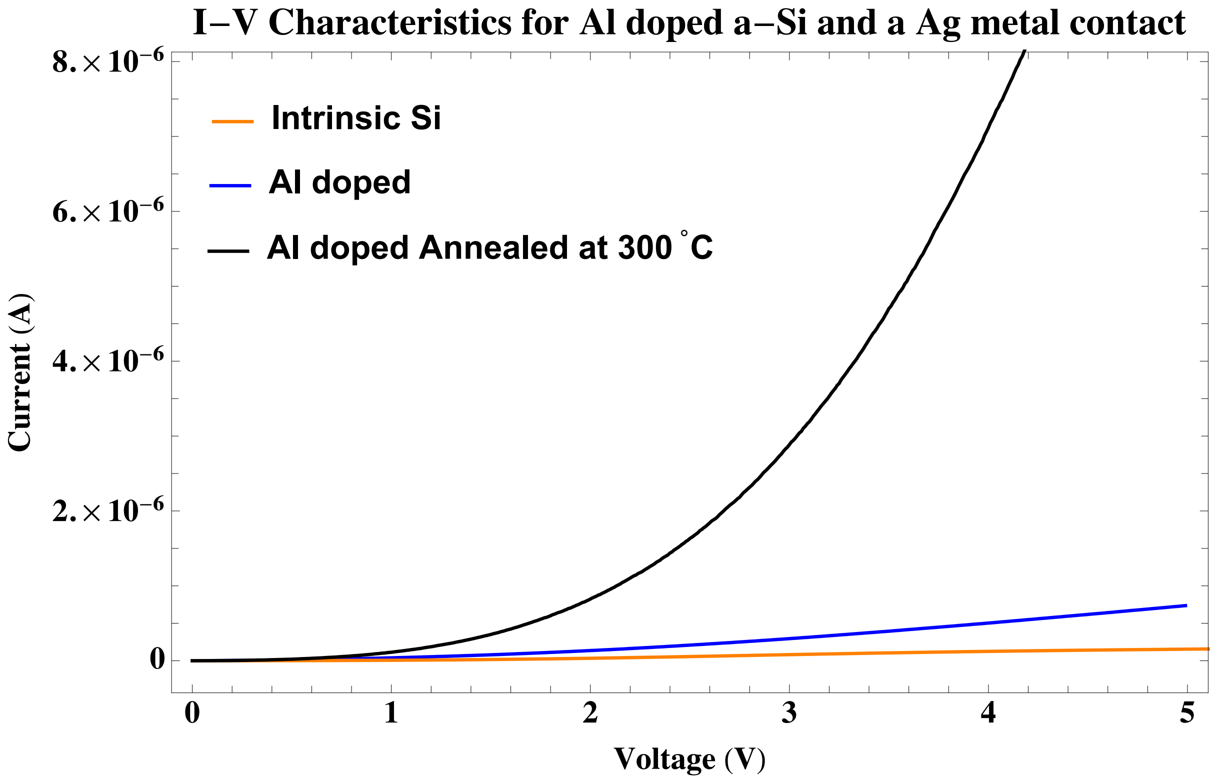

Figure 5.1: I-V characteristics of an undoped, Al doped and annealed Al doped 20 nm a-Si film contacted to an Ag electrode. The Al doped film is annealed at 300 °C for 20 minutes.

Annealing the 20 nm P doped a-Si thin film at 300 °C, the current density remained the same, but the 20 nm a-Si thin film implanted with Al ions current density increased. This is because of the diffusion coefficient (D) of P in a-Si. The diffusion coefficient at 300 °C for P in a-Si is 9.111×10^{-30} cm^2/s with an activation energy (E_a) of 3.29 eV and for Al in a-Si at 300°C is 2.409×10^{-30} cm^2/s and $E_a = 3.47$ eV[211]. The lower diffusion coefficient of Al in a-Si compared to that of P in a-Si at the same temperature, makes the diffusion of P ions travel deeper into the 20 nm a-Si film when they are annealed compared to the implantation of Al ions in a-Si[212]. The addition of impurities into the intrinsic a-Si shows the enhancement of electrical properties in the film. The electrical properties of the doped a-Si thin films further increased when they were annealed at 300 °C, especially the a-Si thin film doped with Al.

The Schottky barrier height in the undoped a-Si layer in Figure 5.1 and 5.2 is high for both holes and electrons compared to the a-Si layers implanted with Al and P ions. The value for the barrier height for the intrinsic a-Si is $\phi_B = (0.78\pm\ 2.6 \times 10^{-2})$ V. The barrier height for the a-Si implanted with P ions (n-type) is $\phi_{Bn} = (0.70\pm\ 2.4 \times 10^{-2})$ V and the a-Si layer implanted with Al ions (p-type) is $\phi_{Bp} = (0.69\pm\ 2.3 \times 10^{-2})$ V. This shows that the barrier height has decreased when the intrinsic a-Si was implanted with Al and P ions, because of the defect levels inside the bandgap of the bulk semiconductor that are being created by the implantation process. The barrier height for electrons decreased from 0.78 V to 0.70 V while for holes, it changed from 0.78 V to 0.69 V. The chemical potential difference ensures that electrons and holes travel to different electrodes, Ag or ITO when dopants are added to the intrinsic

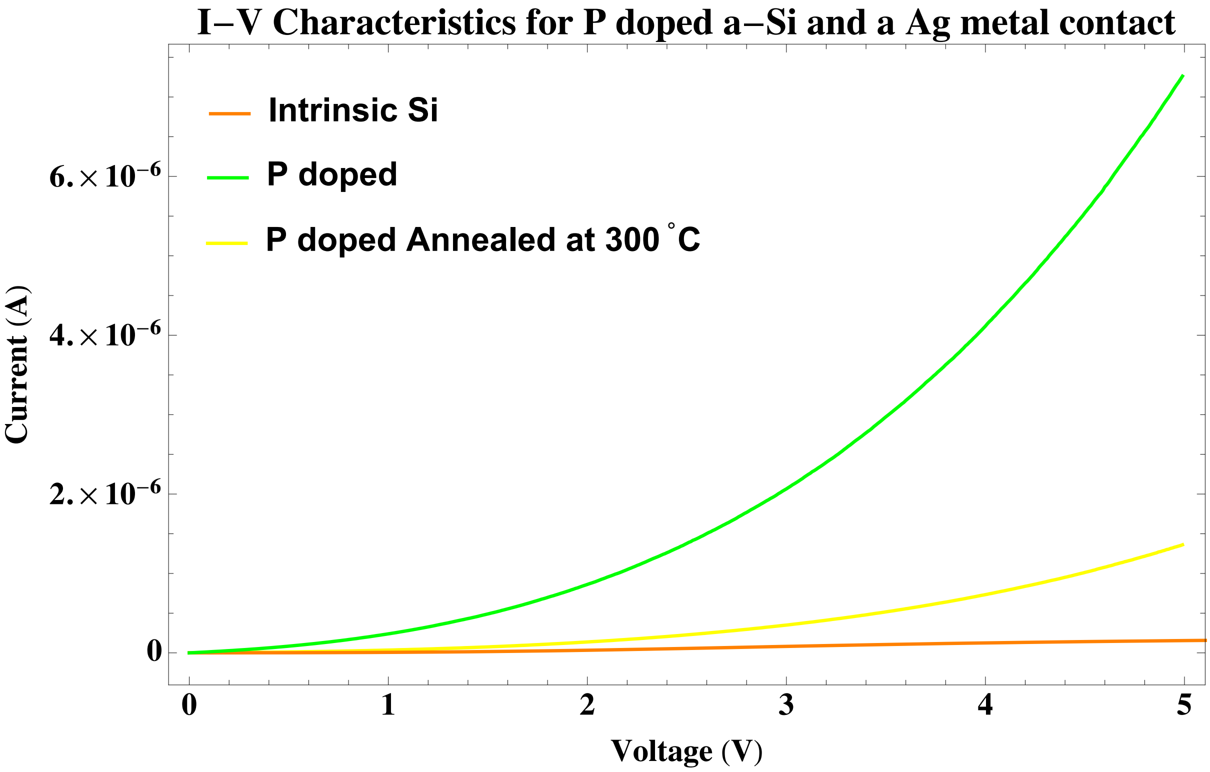

Figure 5.2: I-V characteristics of an undoped, P doped and annealed P doped 20 nm a-Si film contacted to an Ag electrode. The P doped film is annealed at 300 ° for 20 minutes.

a-Si films. This exhibits that the electrons will have to overcome a higher barrier height compared to the holes. The electrons from the Ag metal will interact with the majority carriers in the n-type semiconductor, thus there is a Coulomb repulsion between the electrons from the Ag electrode and the majority carriers in the n-type a-Si film.

The barrier for the majority carriers in the p-type a-Si is less compared to the barrier of the minority carriers, because it is easy for the majority carriers in the p-type to interact with the electrons in the Ag electrode. Annealing both samples at 300 $°C$ for 20 minutes, the barrier height of the p-type a-Si decreased from 0.69 V to 0.62 V. The current density of the n-type a-Si thin film also slightly decreased and because of the exponential form of the I-V characteristics, the barrier height increased from 0.70 V to 0.73 V. From Eq (3.7), $E_g \approx 1.39$ eV $\pm\ 4.7 \times 10^{-2}$ eV and when the samples are annealed, thus $E_g \approx 1.35$ eV $\pm\ 4.6 \times 10^{-2}$ eV. These band gap energies obtained are in agreement with the theoretical value, which is ≈ 1.7 eV[213].

The width of the depletion layer decreases with the increasing concentration of minority or majority carriers. The width also increases with the increasing Schottky barrier height. For the intrinsic a-Si thin film, the width of the depletion layer was $(2.66 \pm 4.5 \times 10^{-2})$ nm and the width decreased for the extrinsic a-Si thin film. The width further decreased from orders of 100 nm to 10^{-2} nm for the film implanted with P ions and annealed. For the p-type a-Si semiconductor, the width decreased from orders of 100 nm to 0.1 nm, even after it was annealed. This shows that the movement of minority and majority carriers is easier when the intrinsic a-Si is doped with Al and P ions. The width of the depletion layer is reduced, making it easier for the carriers to move from the

Table 5.2: Table showing parameters obtained from the Ag metal-semiconductor (n and p-type) contacts for a junction area of 0.25 cm^2

a-Si	J_s	ϕ_B	R_s	R_c	E	x
	$(\mu A/cm^2)$	(V)	$(k\Omega.cm^2)$	$(k\Omega.cm^2)$	(kV/cm)	nm
Undoped Si	0.85	0.78	531	30.3	5.9×10^{-2}	2.66
	$\pm\ 2.7 \times 10^{-2}$	$\pm\ 2.6 \times 10^{-2}$	± 58.6	± 1.01	$\pm\ 9.9 \times 10^{-4}$	$\pm\ 4.5 \times 10^{-2}$
Al doped	29.2	0.69	15.5	0.89	247	5.01×10^{-4}
	± 4.6	$\pm\ 2.3 \times 10^{-2}$	± 1.71	± 0.03	± 93	$\pm\ 8.5 \times 10^{-6}$
Annealed Al doped	5.62	0.62	8.06	0.46	55.1	2.27×10^{-3}
	± 0.31	$\pm\ 2.1 \times 10^{-2}$	± 0.89	$\pm\ 1.53 \times 10^{-2}$	± 9.22	$\pm\ 3.84 \times 10^{-5}$
P doped	29.5	0.70	153	8.75	58.4	2.4×10^{-3}
	± 4.8	$\pm\ 2.4 \times 10^{-2}$	± 16.9	± 0.29	± 9.73	$\pm\ 4.1 \times 10^{-5}$
Annealed P doped	5.47	0.73	82.8	4.72	283	5.17×10^{-4}
	± 0.24	$\pm\ 2.5 \times 10^{-2}$	± 9.13	± 0.16	± 96	$\pm\ 8.5 \times 10^{-6}$

extrinsic semiconductor to the metal and from the metal to the extrinsic semiconductor.

The electric field created between the Ag electrode and the extrinsic a-Si is also dependent on the size of the depletion layer. The electric field for the intrinsic a-Si layer was very low compared to the extrinsic a-Si thin film. The value of the electric field for the intrinsic a-Si was 58.6 V/cm. When it was implanted with P and Al ions, it went up to the orders of $10^4 - 10^5$ V/cm. This increase is due to an application of an external electric field which produces strong conduction in the doped semiconductor. Heavier doping level produces stronger conduction. Therefore, a poorly conducting intrinsic semiconductor has been converted into a good electrical conductor as mentioned in Chapter 3.

The contact resistance, R_c also shows that the low barrier height gives a small R_c. The undoped a-Si film has a very high R_c compared to the ion implanted a-Si thin films even after they were annealed. The contact resistance for the undoped a-Si thin film is (30.3 ± 1.01) $k\Omega.cm^2$, for the n-type and p-type, R_{cn}= (8.75 ± 0.29) $k\Omega.cm^2$ and R_{cp}= (0.89 ± 0.03) $k\Omega.cm^2$, respectively. When the p-type sample was annealed, the contact resistance decreased exponentially and became $(0.46 \pm 1.53 \times 10^{-2})$ $k\Omega.cm^2$. The n-type a-Si thin film increased slightly because of the increased barrier height after annealing, R_{cn}= (4.72 ± 0.16) $k\Omega.cm^2$.

The sheet resistance (R_s) has the same trend as the contact resistance. R_s for the undoped 20 nm a-Si film is (531 ± 58.6) $k\Omega.cm^2$. When the referenced a-Si thin film is doped with P to make an n-type a-Si, $R_{sn} = (153 \pm 16.9)$ $k\Omega.cm^2$ and for the p-type, $R_{sp} = (15.5 \pm 1.71)$ $k\Omega.cm^2$. For the annealed samples, $R_{sn} = (82.8 \pm 9.13)$ $k\Omega.cm^2$ and $R_{sp} = (8.06 \pm 0.889)$ $k\Omega.cm^2$.

5.1.2 Optical Properties of a-Si P-I-N Layers

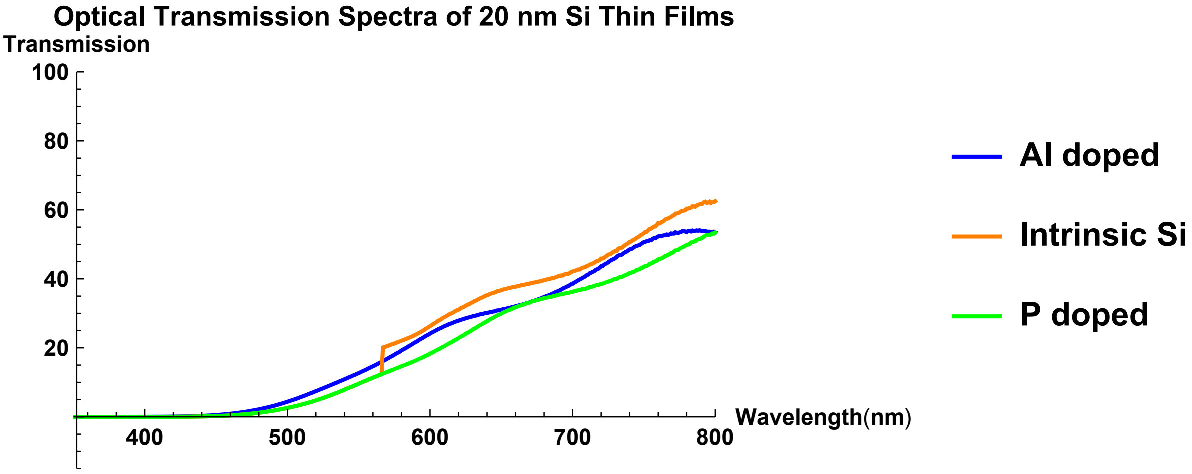

Figure 5.3: UV-Vis spectrometer transmission measurements of the p-i-n layers of a-Si.

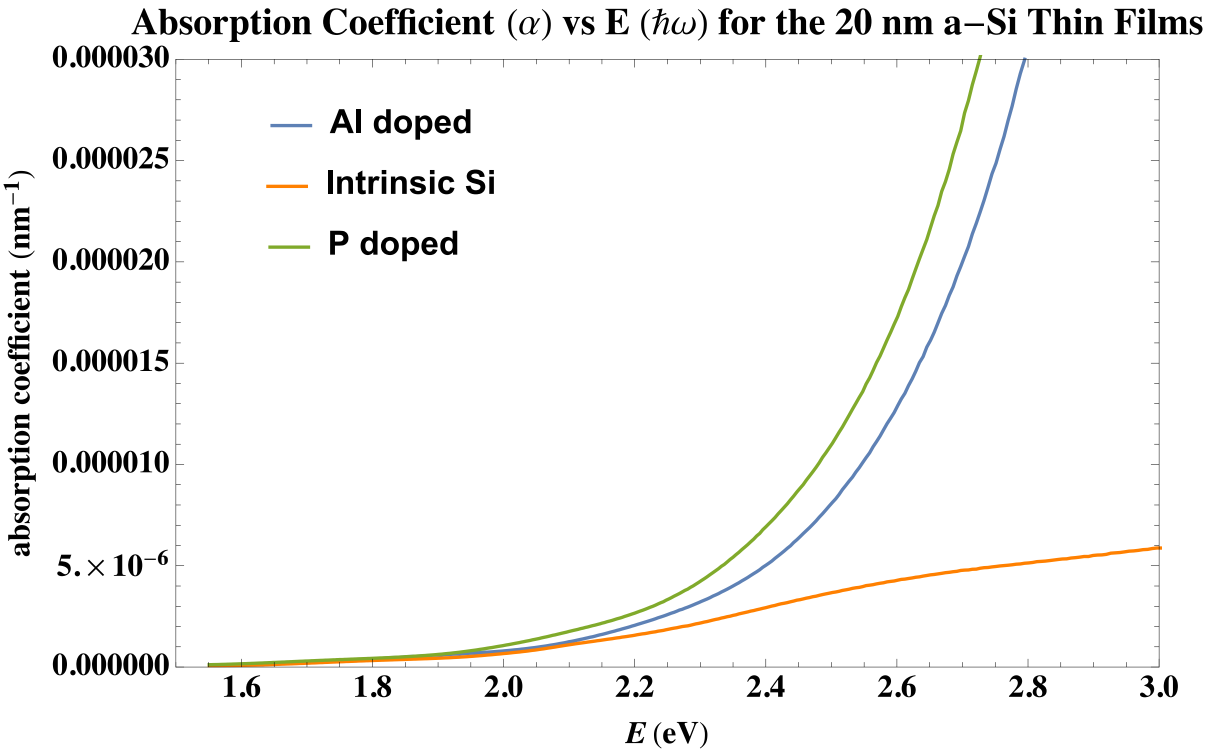

Figure 5.4: Absorption coefficient (α) against the energy.

Figure 5.3 shows transmittance results from the UV-Vis spectrophotometer for three different thin film layers of a-Si. The bandgap energies for p-type , i-layer and n-type are 1.78 eV, 1.53 eV and 1.93 eV, respectively. Thus, these bandgap energies are larger than the bandgap energy of crystalline Si ($\sim$ 1.1 eV). (The energy bandgap values are extrapolated from Figure 5.4, where the curve intersect the x-axis. The absorption coefficient α is plotted against the energy.) The absorption coefficient determines how far the light of a particular wavelength has travelled in the film before it is absorbed by the material. Therefore, the transmission of light reduces as it passes through the thin film. This shows that the bandgap energies are in the visible region of the solar spectrum and these higher energetic photons incident on the solar cell can be absorbed by the i-layer and transmitted by the p and n-type layers of a-Si. Additionally, Figure 5.4 shows that the intrinsic layer of a-Si has a direct transition because the slope of the curve within the linear regime is smaller and this transition rate is determined by Fermi's golden rule.

The i-layer has a smaller bandgap energy (E_{gap}) compared to the doped layers. The bandgap energy of the n-type a-Si layer is greater than the E_{gap} of the p-type layer, thus the p layer has to allow the photons incident on the device to be transmitted into the other layers in the device. The increase in the E_{gap} when adding donor impurities in the intrinsic a-Si film can be due to the Burstein-Moss effect and the adding of acceptor impurities should lower the E_{gap} of the layer. This effect in semiconductor is seen as a shift with increasing doping of the bandgap[214]. The shift emerges because the E_F lies in the conduction band when the film is heavily n-type doped and for p-type doping, it lies in the valence band. The occupied electronic states limit optical and thermal excitation. As a result, the band gaps measured from the start of interband absorption will move to higher energies. The thickness of the layer also plays a major role in the absorbance of photons.

The absorbance in the i-layer can be enhanced by increasing the thickness of the film[215].

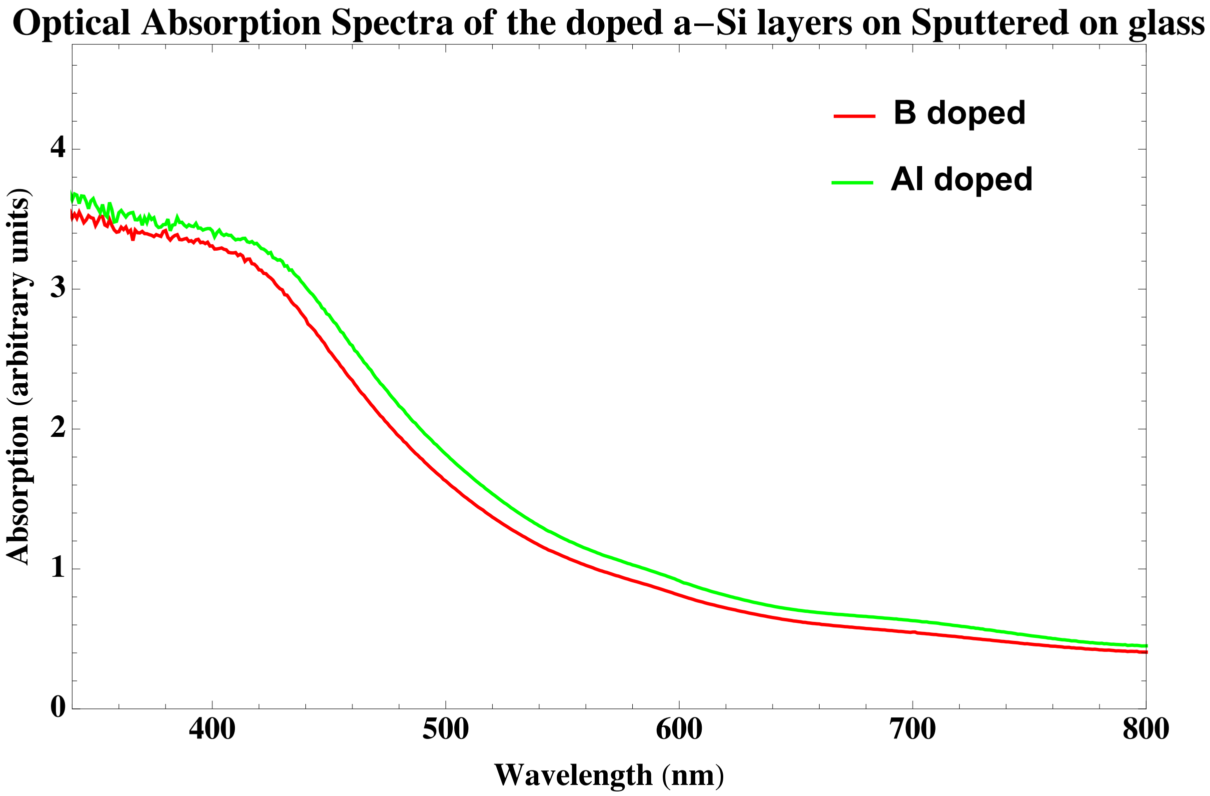

Figure 5.5: Optical absorption spectra of a 20 nm n-type a-Si, 300 nm a-Si:H and 20 nm intrinsic a-Si layers stacked on top of each other by sputtering. The p-type Si is formed from B and Al ions implanted into an intrinsic 20 nm a-Si film.

Figure 5.5 shows the optical characteristics of three different layers deposited on a 300 nm glass substrate. The first layer deposited was the Al doped layer of 20 nm thickness, followed by the i-layer deposited in an Ar and H_2 gaseous mixture. The last layer to be deposited was the i-layer without the H_2 gas of 20 nm thickness. This process was repeated by using B instead of Al as a dopant to form an p-type a-Si.

The optical absorption spectra of these three layers reveals that there is a slight shift of the spectrum compared to the individual layers in Figure 5.3 as more layers are stacked on top each other. The wavelengths absorbed in both figures are in the visible range of the solar spectrum.

5.2 Analysis of the a-Si Commercial Device

5.2.1 I-V Characteristics of Commercial a-Si Solar Cells

The commercial a-Si solar cell was illuminated under AM 1.5 and the I-V characteristics were measured at varying intensities (F) as shown in Figure 5.6. The values of the intensities are presented in Table 5.3.

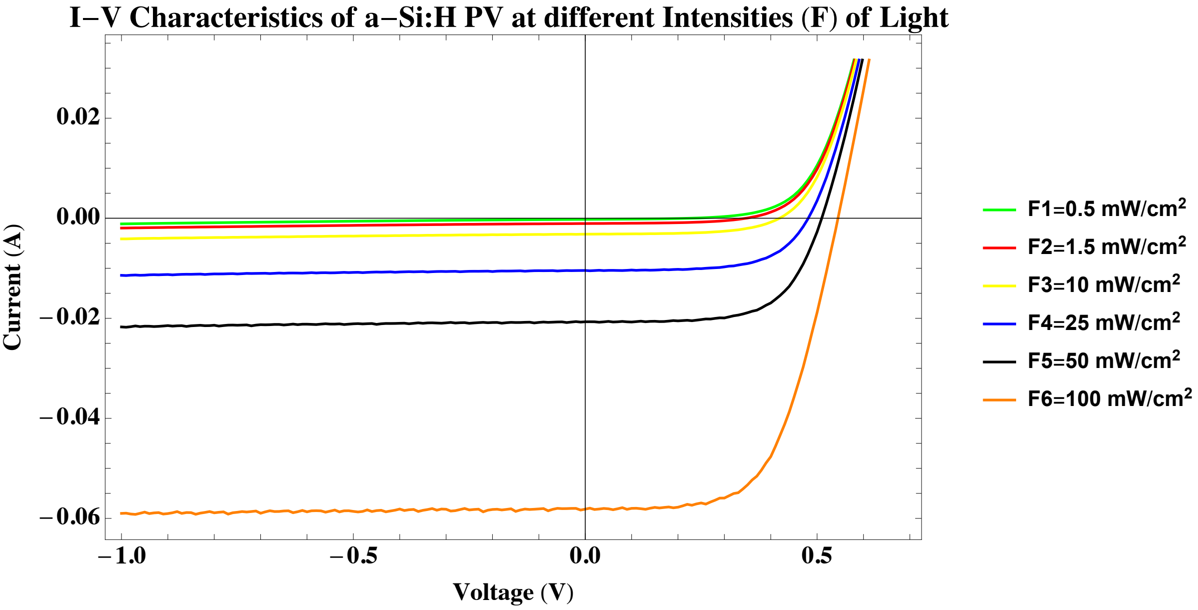

Figure 5.6: I-V characteristics of a commercial a-Si solar cell at different intensities of light.

When the light intensity incident on a solar cell is changed, all parameters of the device such as J_{sc}, V_{oc}, FF, R_{series}, R_{shunt} and PCE changes. These parameters are dependent on the level of light illumination incident on the solar cell. The current increases proportional to light intensity, but if this was the only change, then the efficiency would remain the same. However, V_{oc} increases with the natural logarithm of intensity, as illustrated in Figure 5.7. Table 5.3 shows that the only parameters that decrease as the illumination level of light increases are R_{series} and R_{shunt}. At lower light intensities, R_{shunt} becomes significant because the current and the bias point in the solar cell decrease, bringing the overall resistance of the device closer to R_{shunt}. The two resistances (R_{series} and R_{shunt}) are different, $R_{shunt} >> R_{series}$, and R_{shunt} has a higher value than R_{series}, which is 2 orders of magnitude at low and high intensities. The power loss due to R_{shunt} is caused by the increase in the total current flowing through R_{shunt}. The fill factor slightly increases with low light intensities and this is because of the influence of R_{series}.

The highest light intensity (F6) was used for the I-V characterization of a-Si commercial solar cells, including the devices incorporated with NPs and spectral conversion layers.

Table 5.3: Table showing parameters of commercial a-Si solar cell at different Intensities (F) at a device area of 2.01 cm^2

	$Irradiance$	FF	V_{oc}	J_{sc}	R_{series}	R_{shunt}	PCE
	(W/cm^2)		(V)	(mA/cm^2)	$\Omega.cm^2$	$\Omega.cm^2$	%
F1	5×10^{-4}	0.37	0.22	0.11	845	3926	1.9
F2	1.5×10^{-3}	0.52	0.35	0.53	126	3662	6.3
F3	0.01	0.58	0.42	1.58	39.2	1646	6.4
F4	0.025	0.63	0.48	5.2	12.3	486	6.5
F5	0.05	0.65	0.51	10.3	7.2	461	6.8
F6	0.1	0.60	0.55	28.9	4.51	107	9.5

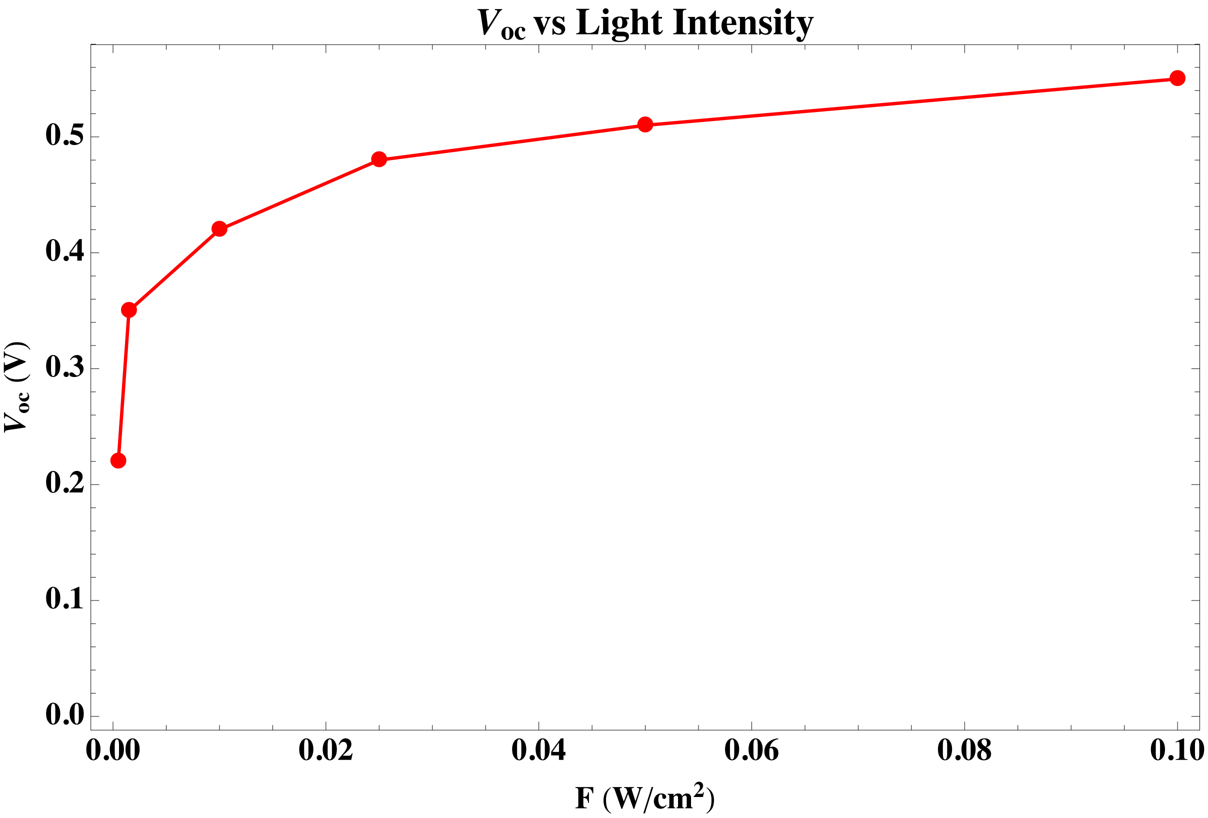

Figure 5.7: Diagram showing open circuit voltage V_{oc} plotted against light intensity F.

The intensity dependence of V_{oc} is much stronger when Schokley-Read-Hall (SRH) recombination is included and the slope of the graph is expected to increase. The change of slope when SRH recombination plays an important role was also noted in a-Si solar cells by Schiff et al., 2003[216]. However, due to the strongly varying density of trapped electrons, the rate of constant for SRH recombination will strongly vary throughout the device, and, consequently, the assumption of generation and recombination cancelling everywhere breaks down.

5.2.2 Morphology of Ag and Au NP's

The Ag and Au NPs were deposited on commercial a-Si PV devices at various deposition times and the Scanning Electron Microscope (SEM) was used to determine the morphology of the NPs in the device. This procedure would also allow for the determination of the size of the NPs, as illustrated in Table 5.4. The size and shape of NPs are determined by using an image processing software known as ImageJ. The software displayed a high surface coverage due to the particles being close to one another. The NPs displayed by the SEM images displayed shapes assumed to be elliptical, spherical and hemispherical. The shape of the NPs were assumed to be spherical for simplicity and the various average size distributions indicated by the surface statistical analysis ranged from 22.3 nm to 142 nm for Au and Ag NPs, as shown in Figures 5.8 - 5.13.

The average sizes of Au and Ag NPs were also different. The reason for this dissimilarity in the two arises from the use of deposition techniques with varying conditions (RF sputtering and thermal evaporation). The deposition rate for the two methods is not the same and it also depends quite strongly on the deposited material. The Au NPs were deposited for a longer time compared to the deposition time of Ag NPs. The deposition time for Au NPs was 90 s and 120 s using thermal evaporation. RF sputtering was used for the deposition of Ag NPs and the deposition times were 10 s, 20 s and 30 s. The average sizes of the Au NPs that were thermally evaporated for 90 s and 120 s are 30.6 nm and 33.8 nm, respectively. The average sizes of Ag NPs RF sputtered for 10 s, 20 s, 30 s turned out to be 32.3 nm, 65.0 nm and 113 nm, respectively. Another factor for the difference in the average sizes of the nanoparticles is the distance between the deposited material and the substrate.

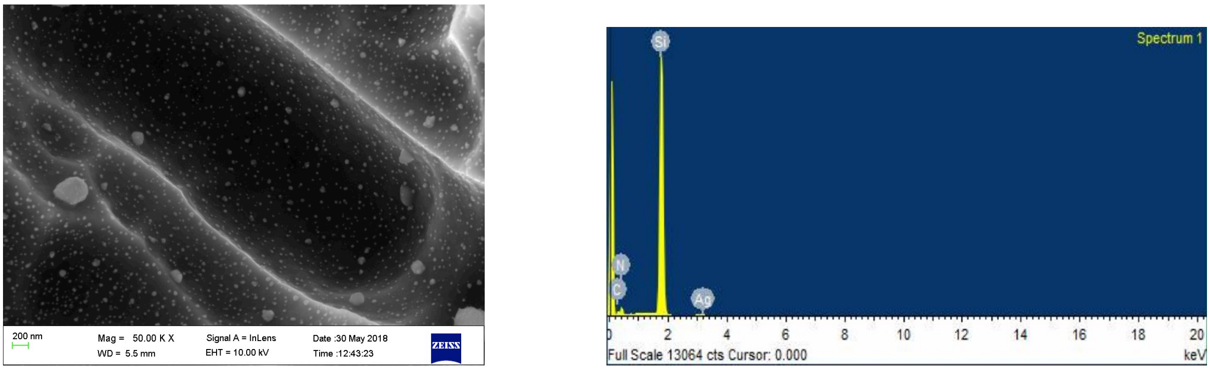

(a) An SEM image showing the NPs of Ag deposited for 10 s.

(b) EDS image of Ag NPs deposited for 10 s.

Figure 5.8: Images of SEM and EDS for Ag NPs deposited for 10 s.

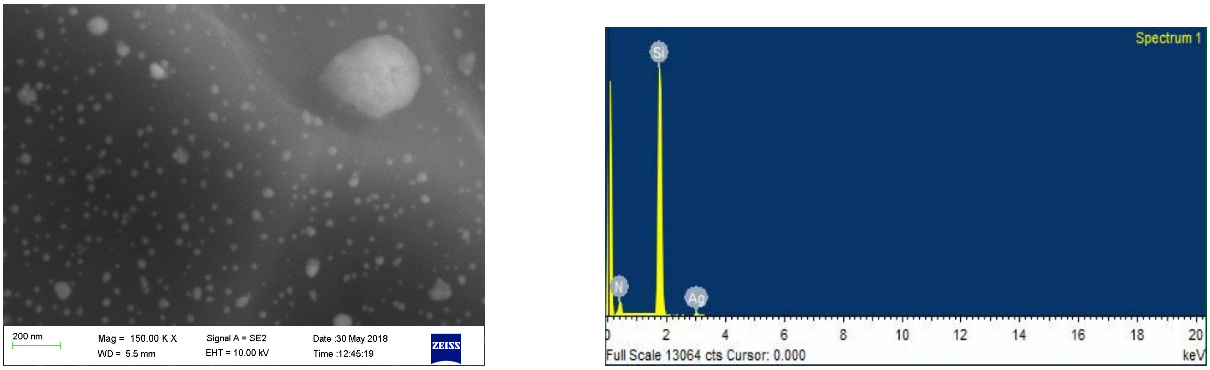

(a) An SEM image showing the NPs of Ag deposited for 20 s.

(b) EDS image of Ag NPs deposited for 20 s.

Figure 5.9: Images of SEM and EDS for Ag NPs deposited for 20 s.

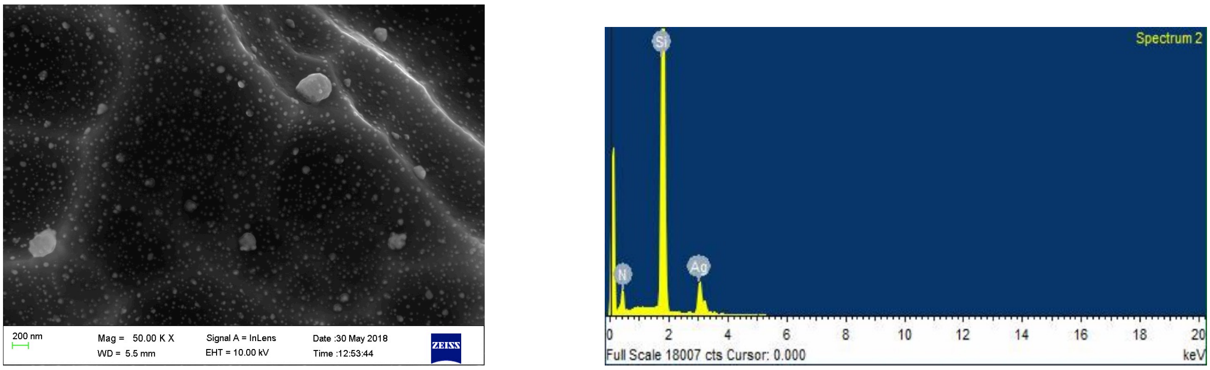

(a) An SEM image showing the NPs of Ag deposited for 30 s.

(b) EDS image of Ag NPs deposited for 30 s.

Figure 5.10: Images of SEM and EDS for Ag NPs deposited for 30 s.

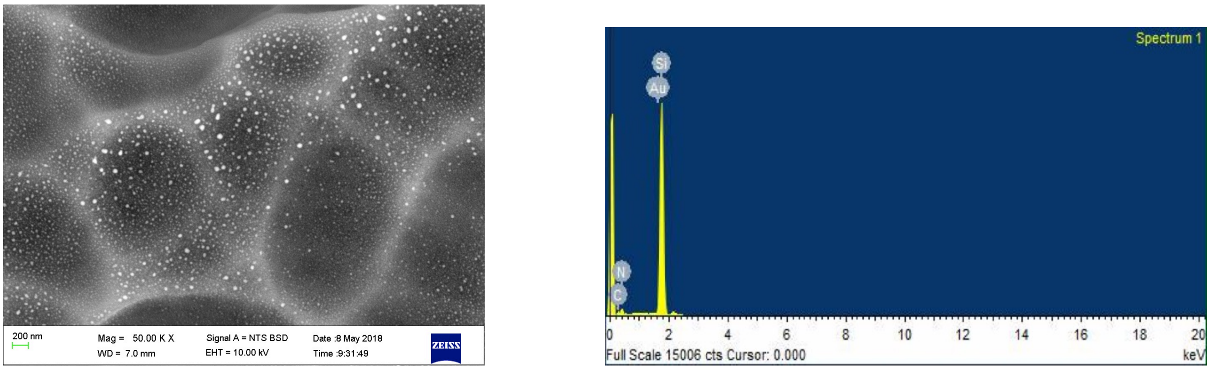

(a) An SEM image showing the NPs of Au deposited for 90 s.

(b) EDS image of Au NPs deposited for 90 s.

Figure 5.11: Images of SEM and EDS for Au NPs deposited for 90 s.

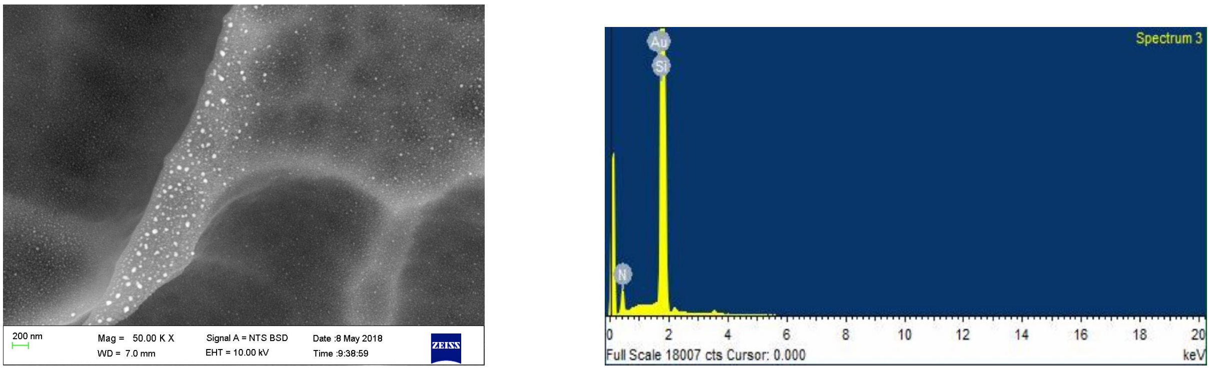

(a) An SEM image showing the NPs of Au deposited for 120 s.

(b) EDS image of Au NPs deposited for 120 s.

Figure 5.12: Images of SEM and EDS for Au NPs deposited for 120 s.

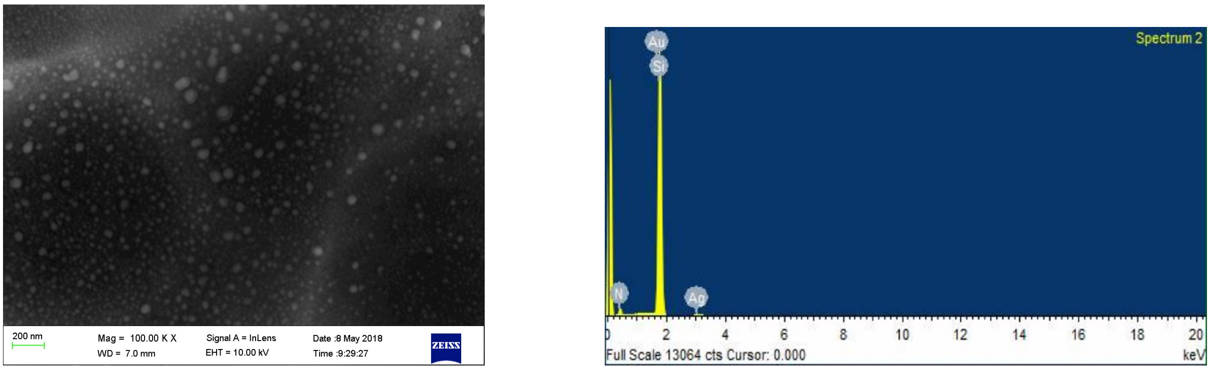

(a) An SEM image showing the NPs of Au deposited for 120 s and Ag deposited for 30 s.

(b) EDS image of Au NPs deposited for 120 s and Ag deposited for 30 s.

Figure 5.13: Images of SEM and EDS for Au NPs deposited for 120 s and Ag deposited for 30 s.

Figures 5.8 - 5.13 display the images of the SEM and the EDS spectrum. The SEM evaluation of the dispersion of Ag and Au NPs revealed the presence of clusters of NPs around the average size of approximately 82 ± 2.93 nm. The arrangement of the NPs indicated that the clusters are held together by weak binding forces. The chemical composition of the NPs (Au and Ag) was confirmed by the EDS spectrum, which detects the NPs deposited on top of the commercial a-Si solar cells.

Figures 5.8 - 5.10 show the SEM images and EDS spectra for RF sputtered Ag NPs at different times on the a-Si commercial PV. The highest peak in the three EDS spectrums is Si and it also shows that there is a presence of Ag NPs corresponding to the lowest peak. The peak for Ag increases in the EDS spectra with increasing deposition time. Figure 5.10b has a higher peak intensity of Ag compared to Figures 5.8b and 5.9b of the EDS spectrum. Sputtering for a longer time increases the Ag peak, as more of Ag NPs are deposited on the a-Si solar cell. Nitrogen and Carbon are other elements confirmed by the EDS spectrum. Carbon only appears in Figure 5.8b for the 10 s deposition of Ag. However, the peak of Carbon in the EDS spectrum is less compared to the Ag and Si peaks. Nitrogen is present in all the three EDS spectrums. The reason for the appearance of these unexpected elements (Carbon and Nitrogen) is possibly due to the sputtering chamber being contaminated. Nitrogen gas is used by the sputtering system for venting and targets containing Carbon may have been used previously by the system.

The thermally evaporated Au NPs are shown in Figures 5.11 - 5.12. The peak of the Au element in the EDS spectrum is slightly lower than the peak of Si when depositing Au NPs for 90 s, as illustrated by Figure 5.11b and the peak of the Au NPs deposited for 120 s is moderately higher than the Si peak of the EDS spectrum. The intensity of the Au and Si peak increases along with the Full Width at Half Maximum (FWHM) with increasing deposition time. This change in peaks is because of the quantity of Au deposited in a specific area of the cell was detected by the SEM. Carbon and Nitrogen are also confirmed by the EDS spectrum for thermally evaporated Au NPs. The occurrence of these elements is the same reason as the sputtered Ag NPs. Figure 5.13 exhibits an SEM image and the EDS spectrum of Ag NPs deposited first by sputtering for 30 s followed by the thermal evaporation of Au NPs for 120 s. The EDS reveals a strong

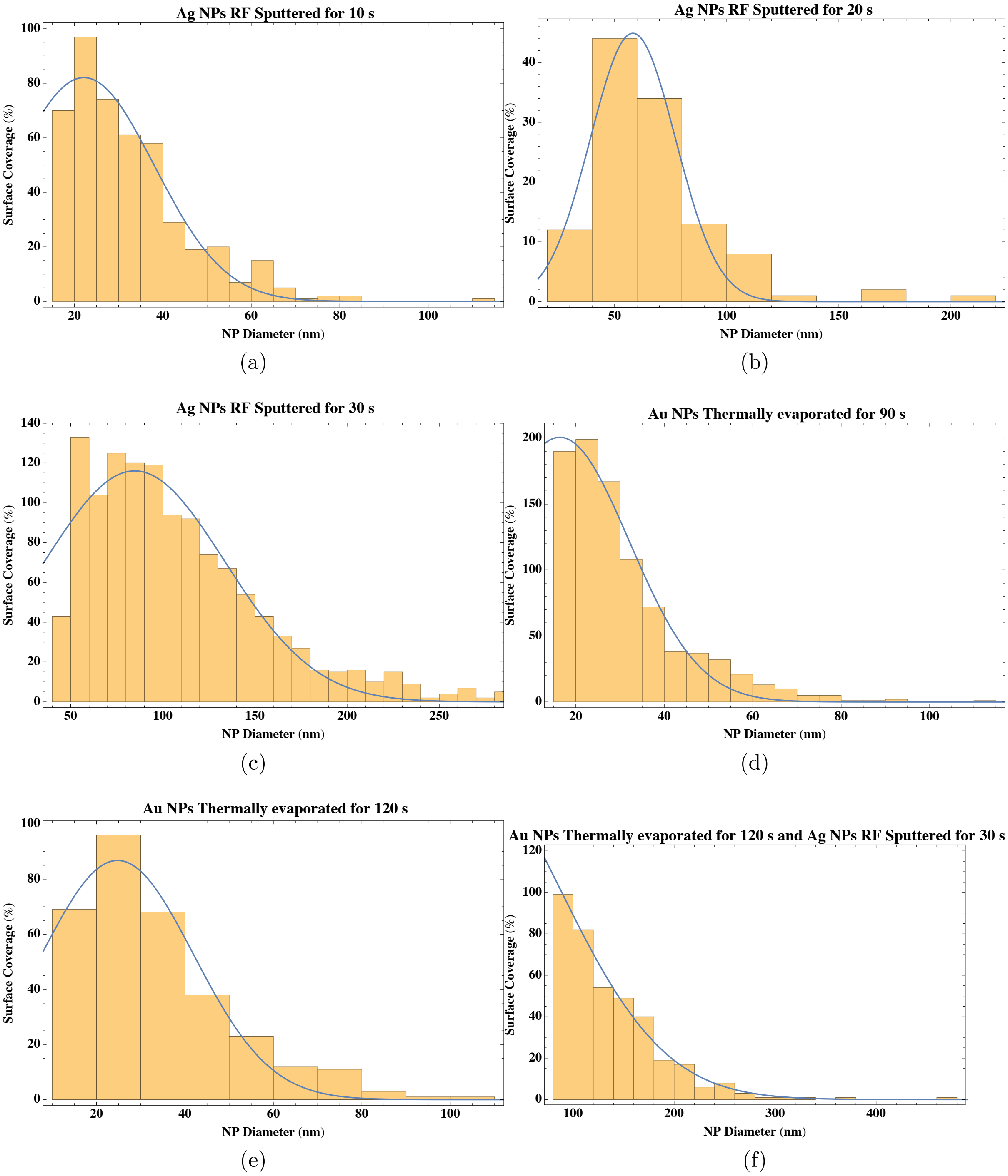

(a) (b) (c) (d) (e) (f)

Figure 5.14: Size distribution of deposited Ag Nanoparticles using RF sputtering and the deposition of Au Nanoparticles using thermal evaporation at different times.

presence of the Au and Ag elements and their peaks are approximately the same as the peaks in Figure 5.10b and 5.12b when the elements are deposited separately on the commercial a-Si solar cells.

The most significant difference in the two deposition methods is the rate at which the materials are deposited on a surface. However, the type of material used can also play an important role in the deposition process. The images of the SEM show that the two materials are dissimilar and that the NPs deposited for a longer time becomes more spherical, more evenly spaced and larger in agreement with the Volmer-Weber growth mode. The SEM images of thermally evaporated Au NPs in Figures 5.11a - 5.12a are brighter than the SEM images of sputtered Ag NPs in Figures 5.8a - 5.10a whereas the SEM image (Figure 5.13a) of the deposition times of Ag and Au NPs is less brighter than the images of the thermally evaporated Au NPs. The reason for the decrease in brightness in Figure 5.13a is because there is a mixture of Au and Ag NPs, and the brightness of Au is affected by Ag plasmon resonance.

5.2.3 Optical Properties of Ag/Au NPs

The NPs were also deposited on glass in order to measure their absorption and transmission. Plasmonic resonance excitation shows strong absorption and scattering of incoming photons resulting in the surface plasmon extinction bands being intensified. This plasmon extinction is dependent on the size and shape of the NPs.

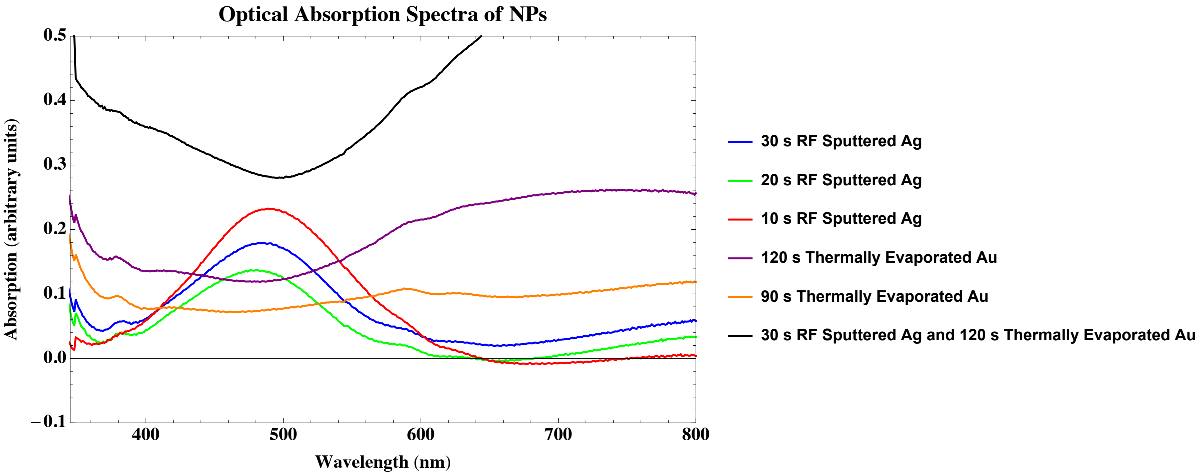

Figure 5.15: Optical absorption spectra of Ag and Au NPs deposited on glass.

Optical properties for the Ag/Au NPs deposited on a glass substrate are shown in Figure 5.15 and it can be observed that the Ag NPs deposited for 10 s absorb more light in the UV region compared to Ag NPs deposited for 20 s and 30 s. The three sputtered Ag NPs absorbs more photons between 460-490 nm of the UV-Vis spectrum. The 10 s sputtered Ag NPs have a higher absorbance than the 20 s and 30 s deposition of Ag NPs because depositing the NPs for a longer time increases the average size of the NPs and larger NPs contributes to scattering and reflection losses. The Au NPs absorption spectra deposited for 120 s is slightly higher than the absorption spectra of Ag NPs deposited for 10 s and the 90 s deposition of Au. Both the Au NPs have a broad LSP resonance and this can be explained in terms of the effects from the LSP multi-pole effects as stated by the Mie theory[217]. The Au NPs deposited for 90 s has less absorption than the Au NPs deposited for 120 s. It is expected for the absorption to decrease as the Au is deposited for a longer time, but Au NPs have an optimum size of 20 - 30 nm[218]. The deposition of Ag NPs for 30 s and the Au NPs for 120 s on glass shows reduction in absorption due to possible reflection losses. This is because the size of these NPs are larger since the Au NPs will increase coverage leading to contact with the Ag NPs deposited initially on the glass substrate. The coalescence of these two types of NPs will increase the surface area of the individual NPs and thus increase the average size of the NPs. The shape of these NPs looks more spherical compared to the shapes of other NPs in the absorption spectra, but this large spherical NPs will scatter light rather than absorbing it.

5.2.4 Efficiency Enhancement of the a-Si Commercial Standard Device

The attempt to increase the efficiency of the commercial a-Si devices was done by depositing only Ag/Au NPs on top of the commercial a-Si device. The Ag NPs were deposited for 10 s , 20 s and 30 s using RF sputtering, and the Au NPs deposited by thermally evaporating Au for 90 s and 120 s on the a-Si solar cells. The Au and Ag NPs were combined by initially depositing Ag NPs for 30 s followed by the deposition of Au NPs for 120 s on the same a-Si device.

The second approach was to deposit only $ZnO:Tb^{3+}$ as a spectral conversion layer using RF magnetron sputtering. The $ZnO:Tb^{3+}$ layer was deposited on top of the a-Si solar cells as a DC layer for 2 minutes and 5 minutes. These deposition times were selected because of the transmission spectra in Figure 5.18. The NPs (Au and Ag) are then deposited on top of the a-Si commercial devices with the $ZnO:Tb^{3+}$ layer. This is done in the $ZnO:Tb^{3+}$/Ag and $ZnO:Tb^{3+}$/Au sequences on top of the a-Si devices. The deposition conditions used for the growth of NPs in front of the $ZnO:Tb^{3+}$ layer are listed on Table 4.3 and Table 4.4. The attempt to further increase the efficiency of the commercial a-Si devices was completed by annealing the a-Si devices with $ZnO:Tb^{3+}$ layer only and the one combined with the NPs.

5.2.4.1 NPs Efficiency Enhancement on Commercial a-Si PVs

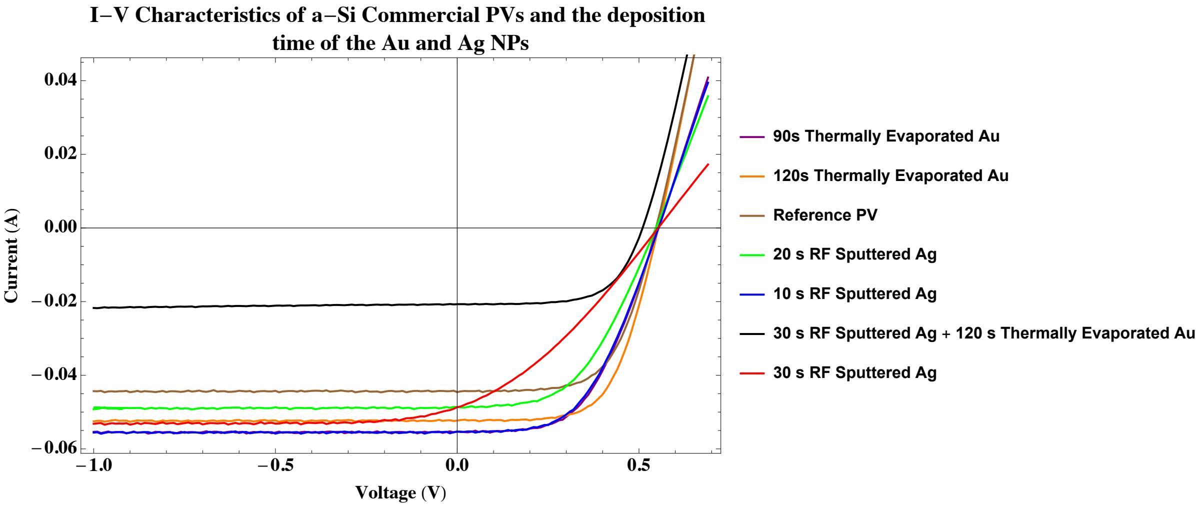

Figure 5.16: I-V characteristics of commercial a-Si solar cells with Ag and Au NPs.

Noble metal NPs absorb light initially through the Surface Plasmon Resonance (SPR) effect. The tuning of the resonance is dependent on the density of the free electrons, their effective masses, shape or size of the NPs. For larger NPs, scattering of light dominates over absorption, thus plasmonic size dependent effects should enhance photocurrent in solar cell devices. The resulting enhancement of photocurrent could lead to efficiency enhancement of the device.

The IV characteristics of the modified a-Si commercial solar cells with Ag/Au NPs are shown by Figure 5.16. When depositing the Ag NPs for 10 s on top of the reference a-Si solar cell, J_{sc} increases from 22.1 mA/cm^2 to 27.5 mA/cm^2. For the a-Si devices deposited with Ag NPs for 20 s and 30 s, J_{sc} decreases from 27.5 mA/cm^2 to 24.2 mA/cm^2 for both devices, but the FF for the 30 s deposition of the Ag NPs is the lowest compared to the 10 s and 20 s deposition times. The FF value for Ag NPs deposited for 30 s is 0.32, for the 20 s one, it is 0.50 and 0.52 for the 10 s deposition time of Ag NPs. The a-Si PV with Au NPs deposited for 120 s increases the J_{sc} to 26.0 mA/cm^2. The commercial a-Si devices with the highest J_{sc} value are supported by Figure 5.15 which shows that Au NPs deposited for 120 s and the Ag NPs deposited for 10 s absorbs more photons compared to other NPs deposited on the a-Si solar cells. The lowest J_{sc} value is observed when the Ag NPs are deposited for 30 s followed by the deposition of Au NPs for 120 s and $J_{sc} = 10.3$ mA/cm^2. This a-Si device with the lowest J_{sc} has the highest $FF = 0.65$ value compared to other a-Si solar cells deposited with NPs including the reference a-Si device. The low J_{sc} value could be attributed to the reflection losses caused by the shape and size of these nanoparticles.

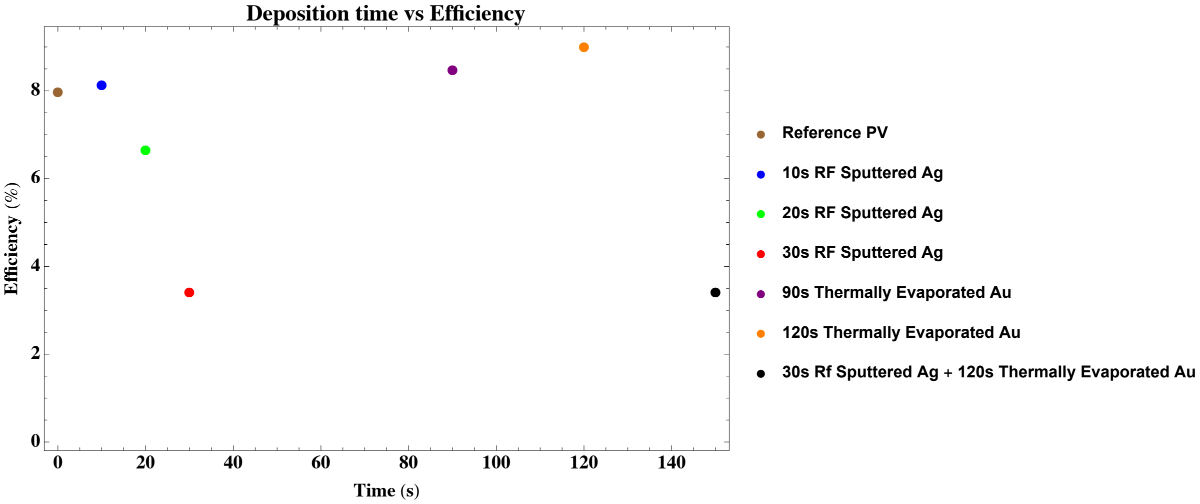

Figure 5.17: Dependence of efficiency on the coverage of Ag/Au NPs.

The variation of the photoconversion efficiency with the deposition time of nobel metal NPs is shown in Figure 5.17. The dependence arises from linear correlation between NP size with the deposition time. Depositing the NPs on the device for a longer time yields larger particles as compared to depositing them for a short time. The efficiency of the a-Si PV cell with Ag NPs deposited for 10 s is greater than the efficiency of the a-Si solar cell deposited with Ag NPs for 20 s and 30 s. The increase in efficiency from a commercial a-Si PV cell without NPs (Ag/Au) to an a-Si solar cell deposited with Ag NPs for 10 s is 0.5%. When the a-Si PV is deposited with Ag NPs for 20 s and 30 s, the efficiency decreases by 0.9% and 3.1%, respectively. The average size of the Ag NPs deposited for 10 s is 32.3 nm and this size is less than the average sizes of the Ag NPs deposited for 20 s and 30 s. The average sizes of the Ag NPs deposited for 20 s and 30 s are 65.0 nm and 113 nm, respectively. When the commercial a-Si solar cell is deposited with Au NPs for 90 s, using a different deposition system (Thermal evaporation) from the one used to deposit Ag NPs (RF Magnetron), the average sizes of the two NPs are slightly the same, but the efficiency is higher for Au NPs than Ag NPs. The performance of the a-Si commercial solar cell with NPs can be attributed to the surface coverage difference and the size distributions of the NPs. The average size of the Au NPs deposited for 90 s is 30.6 nm and efficiency difference between the materials is that Au NPs resonates at a higher frequency compared to Ag NPs. Increasing the deposition time for Au NPs to 120 s also increases the efficiency of the a-Si device, even though the average size of the NPs (33.8 nm) is closer to the average size of the Ag NPs deposited for 10 s. Combining the Au and Ag NPs together by depositing Ag NPs for 30 s first and finally depositing Au NPs for 120 s will decrease the efficiency of the a-Si PV, also increasing the size of the NPs.

Table 5.4 shows the parameters of the reference a-Si solar cell and for that of a-Si solar cells deposited with NPs. The two parameters that affects the overall performance of the a-Si solar cell are known as parasitic resistances and they are the series resistance (R_{series}) and shunt resistance (R_{shunt}). The efficiency in the a-Si PV is decreased by R_{series} which dissipates power through the parasitic resistances. The two resistances are extracted from the IV characteristic curve in Figure 5.16 by taking the inverse slope closer to I_{sc} and V_{oc}, respectively. In the reference device, the value of R_{series} and R_{shunt} have the lowest value compared to the devices with NPs, and they are 5.1 $\Omega.cm^2$ and 48.5 $\Omega.cm^2$, respectively. The two resistances increase in value upon deposition of NPs on the commercial a-Si solar cells with R_{shunt} always higher than R_{series}. It is also observed from Table 5.4 that the R_{series} and R_{shunt} are dependent on the FF value. The decrease in PCE of the entire device is because of the drop in FF, which is attributed to the increase in R_{shunt} and R_{series}. The degradation of PCE is also due to the drop in J_{sc} which is attributed to the optical transmission losses caused by thermalization and the large NPs on the devices, as in the case of the 30 s and 120 s deposition times of Ag and Au NPs, respectively. The increase in the R_{series} is dependent on the conductivity of the acceptor and donor layers of the device. The addition of the NPs on the device (acceptor layer) changes the R_{series}, thus the mobility of the layer affects R_{series} and space charges are generated by the NPs.

Table 5.4: Table showing parameters of plasmon enhanced a-Si commercial PVs.

NPs deposition time	V_{oc}	J_{sc}	FF	NPs size	PCE	R_{series}	R_{shunt}
(s)	(V)	(mA/cm^2)		(nm)	(%)	$(\Omega.cm^2)$	$(\Omega.cm^2)$
0	0.55	22.1	0.62	0	7.5	5.1	48.5
10 (Ag)	0.55	27.5	0.52	32.3	8.0	7.0	68.3
20 (Ag)	0.55	24.2	0.50	65.0	6.6	8.4	311
30 (Ag)	0.55	24.2	0.32	113	4.4	15.8	57.9
90 (Au)	0.55	27.5	0.55	30.6	8.1	6.9	166
120 (Au)	0.55	26.0	0.62	33.8	9.0	6.2	115
30 (Ag)+120 (Au)	0.51	10.3	0.65	137	3.4	7.2	461

5.2.4.2 Optical Properties of $ZnO : Tb^{3+}$ with Au/Ag NPs

The $ZnO : Tb^{3+}$ layers were deposited at different times on a glass substrate using RF magnetron sputtering and the optical transmission of each layer was analyzed.

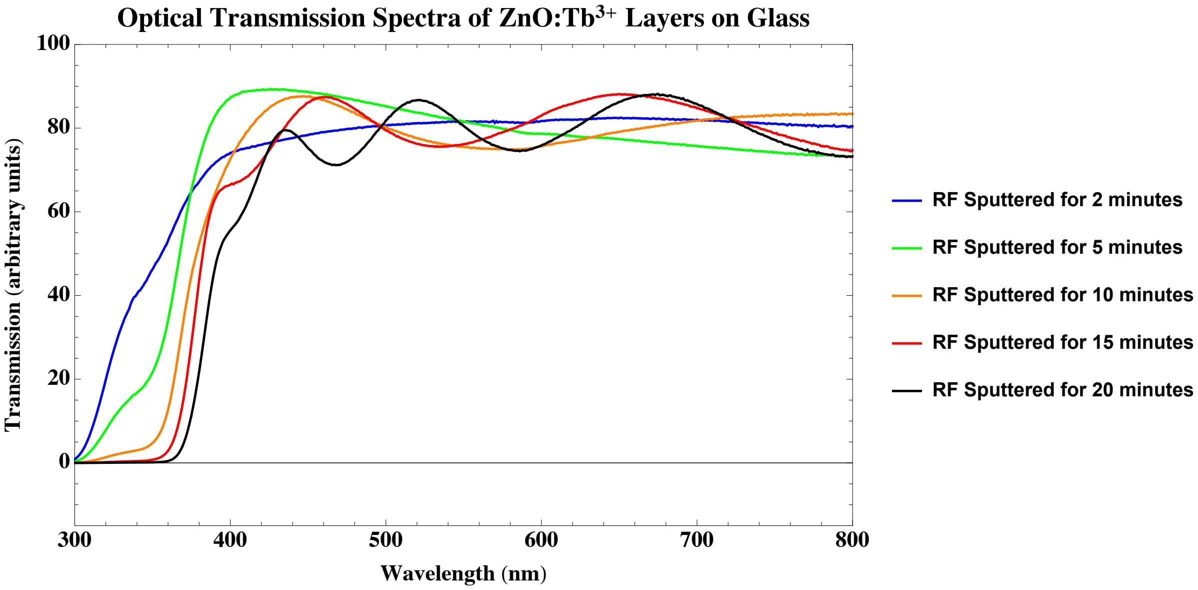

Figure 5.18: Optical transmission spectra of $ZnO : Tb^{3+}$ layers deposited on glass.

The $ZnO : Tb^{3+}$ layers deposited on glass at different times are shown in Figure 5.18 and from this figure it can be seen that the transmission spectra of the layers slightly increases when $ZnO : Tb^{3+}$ is deposited for a longer time. These variations are considered as proof of optical transitions at different peaks of the spectrum for the spectral conversion layers. These direct optical transitions are at 3.28 eV (378 nm) and 3.16 eV (392 nm) for the $ZnO : Tb^{3+}$ layers deposited for 2 minutes and 5 minutes, respectively. The $ZnO : Tb^{3+}$ layer had optical transitions at 1.73 eV (718 nm) and 2.94 eV (422 nm). Thicker $ZnO : Tb^{3+}$ layers show more than one direct optical transition. The $ZnO : Tb^{3+}$ layer deposited for 10 minutes had direct optical transitions at 1.91 eV (648 nm) and 2.59 eV (478 nm). The thickest $ZnO : Tb^{3+}$ layer deposited for 20 minutes had three direct optical transitions at 1.86 eV (667 nm), 2.42 eV (nm) and 2.92 eV (424 nm). The energies in the transmission spectra give the locations of the local minima of the $ZnO : Tb^{3+}$ films in the visible part of the spectrum. The local minima of thicker $ZnO : Tb^{3+}$ layers are deep and sharp, and they correspond to the interference patterns. Depositing $ZnO : Tb^{3+}$ on glass for a longer time results in ZnO and Tb^{3+} atoms being distributed evenly, meaning that there more Tb^{3+} atoms sputtered compared to a shorter deposition time and the optical transitions of $ZnO : Tb^{3+}$ layers deposited are closer to the bandgap value of ZnO, which is 3.3 eV[219]. According to the work of Miller et al, 1974[220], as more Tb^{3+} atoms are deposited, the electronic bands are expected to be of zero slope and they will be parallel at interband points that are symmetrical. As a result, the spectra shown in Figure 5.18 may be due to these transitions at symmetrical interband points located below and above the Fermi level[221].

The Ag/Au NPs were deposited on top of the $ZnO : Tb^{3+}$ layers are shown in Figure 5.19 and their optical absorption spectra is shown below. The Au NPs were deposited for 2 minutes and the Ag NPs were deposited for 10 s.

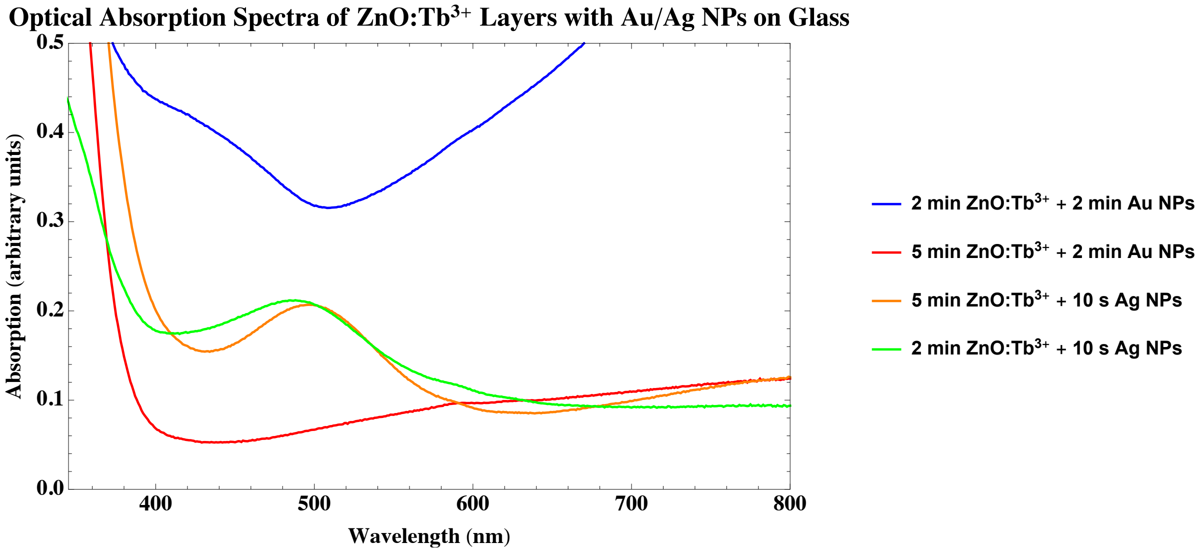

Figure 5.19: Optical absorption spectra of $ZnO : Tb^{3+}$ layers with Ag/Au NPs deposited on glass.

The absorption spectra in Figure 5.19 is compared to the spectra in Figure 5.15. The Au NPs deposited for 120 s and the Ag NPs deposited for 10 s were chosen because they displayed the highest absorption in the spectra in Figure 5.15. The deposition of the Ag/Au NPs on top of the $ZnO : Tb^{3+}$ layer shift the optical transitions to longer wavelengths, but the absorption decreases moderately. The shifts in the absorption spectra of Figure 5.15 and 5.19 are due to the screening of the local fields by the dielectric environment which establishes the charge oscillation by reducing the restoring forces. The NPs in Figure 5.19 exhibit strong dipolar resonances and all the modes from Figure 5.15 are shifted to longer wavelengths[222].

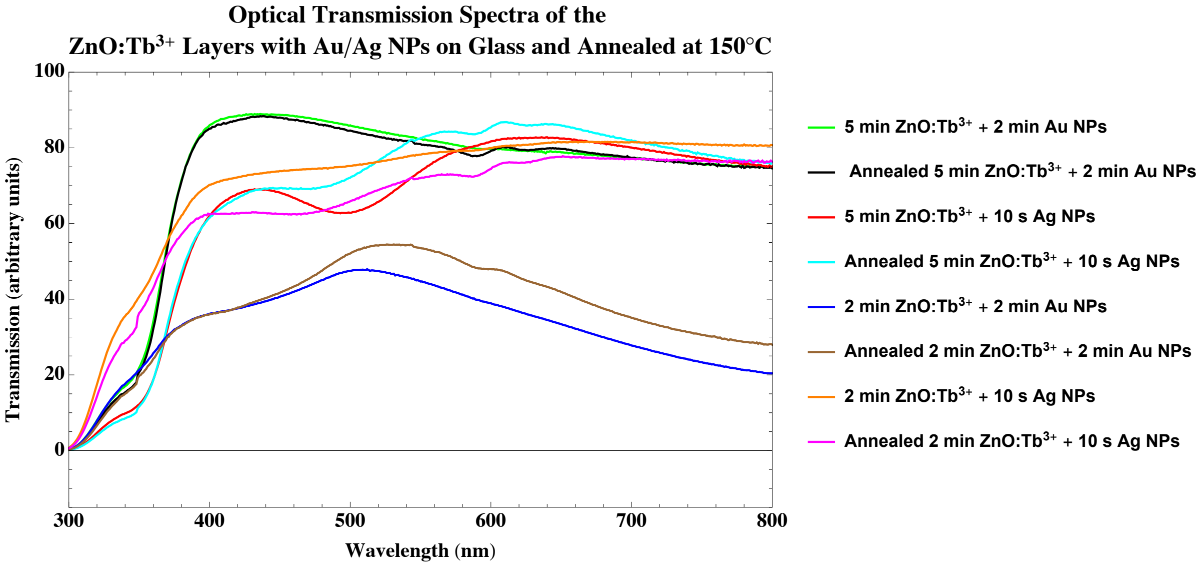

Figure 5.20: Optical transmission spectra of $ZnO : Tb^{3+}$ layers with Ag/Au NPs deposited on glass and they were annealed at 150 $°C$

The transmission spectra in Figure 5.20 shows that when the Au NPs are deposited on the 2 minute sputtered $ZnO : Tb^{3+}$ layer, there is more light transmitted in the UV region of the spectrum, particularly at 598 - 611 nm. There are small sharp peaks at 600 nm for the annealed samples and they could be attributed to the movement of the defects in the ZnO.

5.2.4.3 Efficiency Enhancement by a Spectral Conversion Layer and NPs on the Commercial a-Si PVs

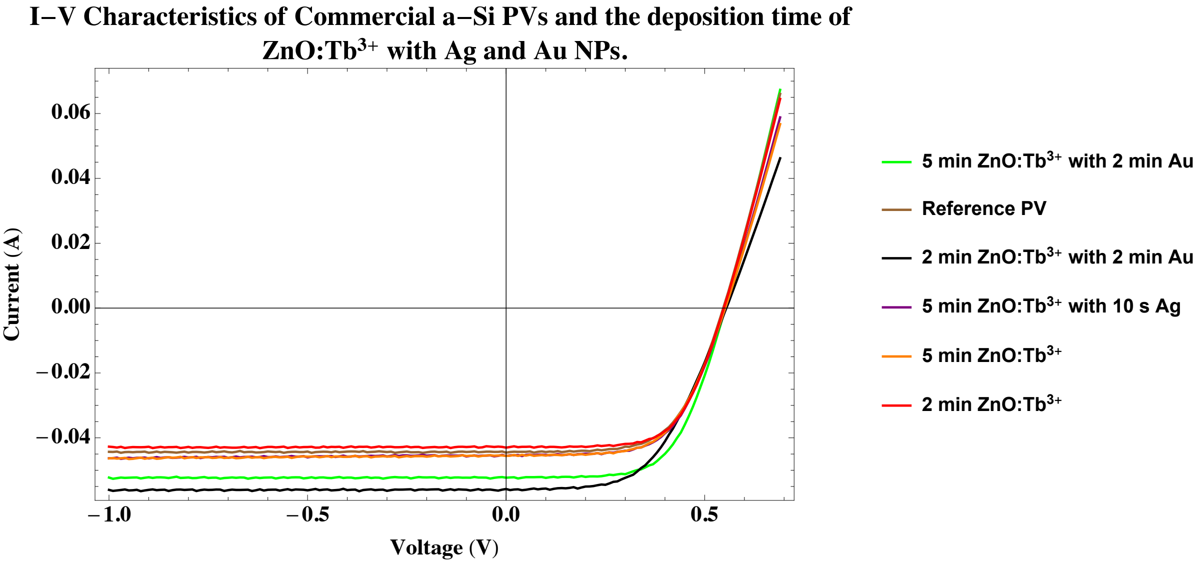

Figure 5.21: I-V characteristics of commercial a-Si solar cells deposited with $ZnO : Tb^{3+}$ and NPs (Au/Ag).

A layer of $ZnO : Tb^{3+}$ on top of a commercial a-Si solar cell increases the efficiency and it is dependent on the deposition time. The $ZnO : Tb^{3+}$ layer deposited for 5 minutes insignificantly increased the efficiency of the device by 0.1% and the layer deposited for 2 minutes did not change the efficiency of the device, it remained the same. The increase to the efficiency in a-Si solar cells is due to more Tb ions being extracted from the target when depositing for a longer time as compared to depositing for a shorter time and this increased the emission intensity from the layer, as shown in Figure 5.18.

Adding NPs on the layer of $ZnO : Tb^{3+}$ to increase photo absorption in the device leads to the enhancement of the efficiency. This is observed in Figure 5.19 and the summarised device performance parameters in Table 5.5. The deposition of Au and Ag NPs increased the efficiency when the NPs were deposited on the commercial a-Si device were chosen based on the optical spectra in Figure 5.15 where Au NPs have $\Delta\eta \sim 1.0\%$ corresponding to an increase by 16%. The efficiency of the commercial a-Si solar cells increased when the NPs were deposited on the layer of $ZnO : Tb^{3+}$. Depositing Ag NPs for 10 s on the $ZnO : Tb^{3+}$ layer sputtered for 5 minutes increased the efficiency of the a-Si device by 0.2% and the evaporation of Au NPs on the 2 minute sputtered layer of $ZnO : Tb^{3+}$ increased the efficiency from 7.5% - 8.5%. Due to the higher efficiency enhancement of the commercial a-Si devices by Au NPs deposited for 2 minutes. Thus, the Au NPs were evaporated for 2 minutes on top of the $ZnO : Tb^{3+}$ layer sputtered for 5 minutes and this further increased the efficiency of the a-Si device by 1.4%, making it closer to the efficiency value of the a-Si device when Au NPs were deposited on the a-Si PV for 2 minutes. Figure 5.21 shows that the $ZnO : Tb^{3+}$ layer deposited for 2

Table 5.5: Table showing parameters of commercial a-Si PVs with $ZnO : Tb^{3+}$ layer and NPs.

Deposition time for		V_{oc}	J_{sc}	FF	PCE	R_{series}	R_{shunt}
$ZnO : Tb^{3+}$ (min)	NPs (s)	(V)	(mA/cm^2)		(%)	$(\Omega.cm^2)$	$(\Omega.cm^2)$
0	0	0.55	22.1	0.62	7.5	5.1	48.5
2	0	0.55	21.4	0.64	7.5	5.1	19.3
5	0	0.55	22.7	0.61	7.6	5.6	133
5	10 (Ag)	0.55	22.7	0.62	7.7	5.4	51.3
2	120 (Au)	0.55	27.7	0.55	8.5	6.3	44.4
5	120 (Au)	0.55	26.0	0.62	8.9	4.7	116

minutes with Au NPs deposited for 2 minutes has the highest current compared to all the other a-Si devices with NPs and spectral conversion layers. Ag absorption is between 460-490 nm, while the bandgap for a-Si varies between 1.8-2 eV, thus this mismatch could lead to low photocurrent for Ag NPs. Also, the increase in the photocurrent for Au NPs deposited for 120 s and subsequently the increase in efficiency is attributed to the matching of LSPR with the bandgap of a-Si.

Kumar et al., 2013[223] reported emission in the ZnO thin films from Zn and O vacancies defect sites when fabricated by RF sputtering. The luminescence from rare earth ions and transition block metal-ions by using sputtering was reported by Tsai et al., 1996[223, 224]. One of the most commonly observed effect in direct sputtering oxides doped with rare earth targets is the deficiency of lighter atoms. This effect can be controlled by performing a post-deposition anneal treatment at higher temperatures in O_2 or air atmosphere. This will make the film to oxidize during treatment and the oxygen deficiency in the deposited thin films will be resolved[225]. The commercial a-Si devices with a spectral layer of $ZnO:Tb^{3+}$ and NPs were annealed in a O_2 atmosphere to remove O vacancies through O compensation. The I-V characteristics for this post deposition treatment are shown below in Figure 5.22.

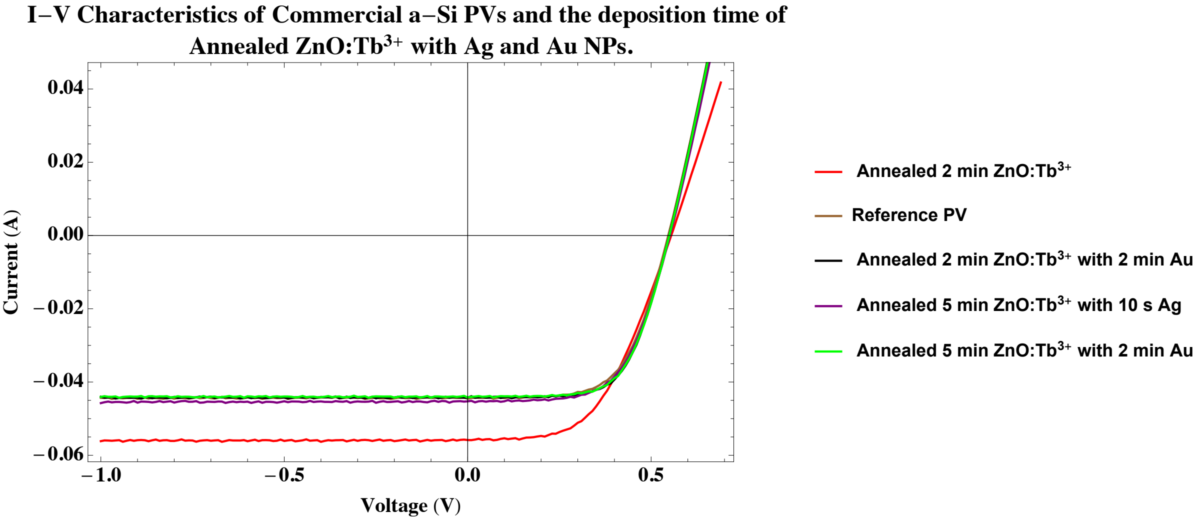

Figure 5.22: I-V characteristics of the annealed commercial a-Si solar cells deposited with $ZnO:Tb^{3+}$ and NPs (Au/Ag). The commercial devices were annealed at a temperature of $150°C$ for 1 hour.

Annealing the a-Si commercial solar cell for 1 hour at 150 $°C$ improved the efficiency of the device with the $ZnO:Tb^{3+}$ deposited for 2 minutes from 7.5% - 8.1%. The efficiency of the a-Si device with the spectral conversion layer sputtered for 5 minutes and the deposition of Ag NPs for 10 s remained the same. The efficiency of the annealed commercial a-Si devices with $ZnO:Tb^{3+}$ layer deposited for 2 minutes and 5 minutes also with the deposition of Au NPs decreased as compared to the efficiency values in Table 5.5. The explanation for the decrease in efficiency in the annealed commercial a-Si devices is due to the temperature used. Otieno et al., 2018[206] reported that post-deposition annealing temperatures at higher annealing temperatures ($600°C$ - $900°C$) for the $ZnO:Tb^{3+}$ layer deposited by RF magnetron sputtering technique

Table 5.6: Table showing parameters of annealed commercial a-Si PVs with $ZnO : Tb^{3+}$ layer and NPs.

Deposition time		V_{oc}	J_{sc}	FF	PCE	R_{series}	R_{shunt}
$ZnO : Tb^{3+}$ (min)	NPs (s)	(V)	(mA/cm^2)		(%)	$(\Omega.cm^2)$	$(\Omega.cm^2)$
0	0	0.55	22.1	0.62	7.5	5.1	48.5
2	0	0.53	27.8	0.53	8.1	6.9	252
5	120 (Au)	0.55	23.4	0.65	8.4	4.6	86.3
5	10 (Ag)	0.55	22.5	0.62	7.7	5.2	72.6
2	120 (Au)	0.55	22.0	0.65	7.8	4.9	44.4

showed increase in the layer's optical and electrical properties, but in our case the annealing temperature is a limiting factor because the temperatures has to be less than 500 $°C$. This is because temperatures above 500 $°C$ will crystallize the a-Si devices with NPs and the $ZnO : Tb^{3+}$ layers.

Figure 5.22 shows that the commercial a-Si solar cell with $ZnO : Tb^{3+}$ layer and Au NPs deposited for 2 minutes leads to the highest photocurrent. This is also supported by the parameters in Table 5.6 by showing the decrease in R_{series} which indicates exceptional improvement in the entire device. The current for the other devices with NPs and spectral conversion layers is more or less the same after annealing. This could be attributed to the increase in R_{series} in these devices, which can also be caused by thermalization.

5.2.4.4 Dark I-V Charactsteristics

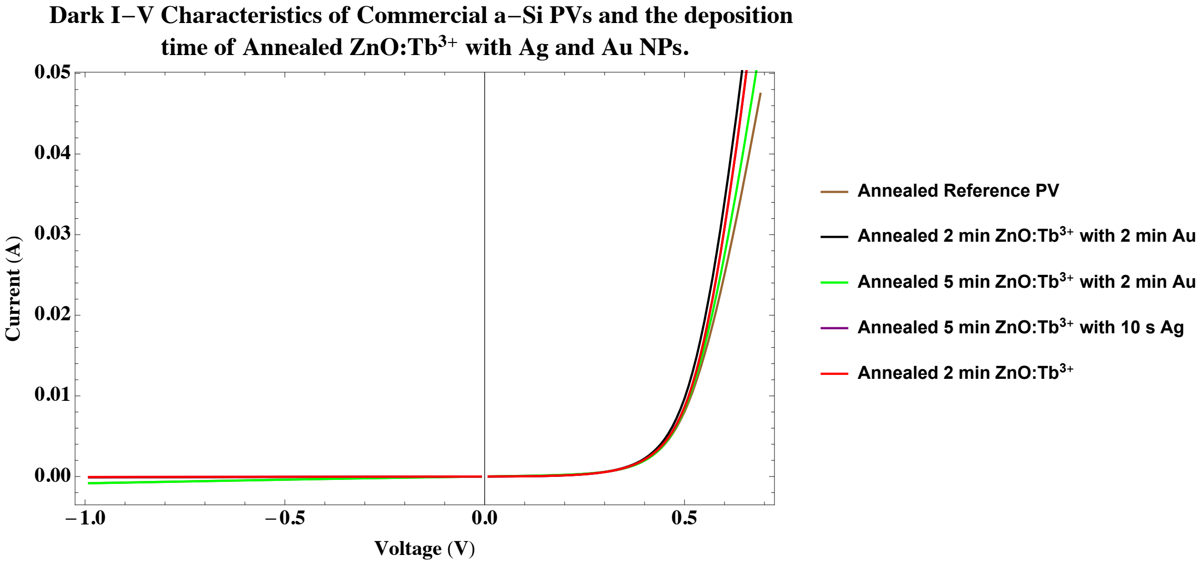

(a) Dark I-V characteristics of annealed commercial a-Si PVs with NPs and a $ZnO : Tb^{3+}$ layer.

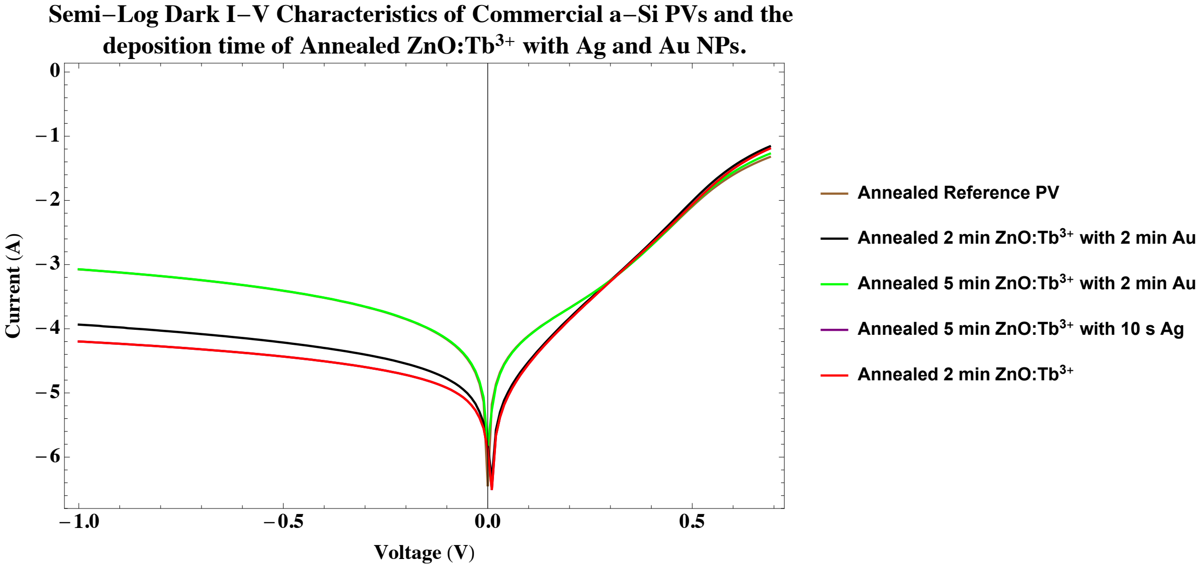

(b) Semi-log dark I-V characteristics of annealed commercial a-Si PVs with NPs and a $ZnO : Tb^{3+}$ layer.

Figure 5.23: (a) Shows dark I-V characteristics of a-Si devices incorporated with NPs and a $ZnO : Tb^{3+}$ layer annealed at 150 $°C$ while (b) is a semi-log plot of the I-V characteristics in the dark.

The annealed commercial a-Si solar cells with $ZnO : Tb^{3+}$ layer and NPs were measured in the dark, as presented in Figure 5.23. The dark current semi-log plot in Figure 5.23b shows higher reverse saturation current indicating that the $ZnO : Tb^{3+}$ layer and NPs (Au and Ag) incorporated in the commercial a-Si solar cells significantly introduced surface recombination centers, resulting to excessive high leakage current density[226]. This is supported by the decrease in value of R_{shunt} when the $ZnO : Tb^{3+}$ layer and NPs are added in the a-Si device. It can be seen from Figure 5.23 (b) that the reverse saturation current is not high and in the forward bias , three regions are observed, the ohmic region (at $V \rightarrow 0$) and the two non-linear regions, where $J \propto V^n$, where n is an integer.

Chapter 6

6 Conclusions and Recommendations

6.1 Conclusion

The research reported in this dissertation focused on the fabrication of layer components of plasmon enhanced a-Si:H solar cells on top of the ITO coated glass and increasing the efficiency of commercial a-Si solar cells using plasmonic NPs and a spectral conversion layer. The a-Si:H PV layers (p-i-n), NPs and the $ZnO : Tb^{3+}$ layer were grown by using a physical vapour technique. The NPs and the spectral conversion layers were incorporated on commercial a-Si devices. The fabrication of the PVs had an initial focus on the electrical characteristics of Schottky barrier contacts using mainly I-V characteristics. The I-V characteristic of a diode was used to extract the barrier height, contact resistance, sheet resistance and the electric field between the three individual fundamental layers (p-i-n) of a-Si:H PV in contact with a metal. The Schottky barrier heights obtained from the I-V curves are in agreement with the theoretical values from Ashcroft et al., 1976[142]. The theoretical values that were calculated by Ashcroft et al., 1976 [142] for the Schottky barrier heights of n-type silicon are between the values of 0.70 - 0.80 V and for the p-type, they are between 0.50 - 0.65 V. These values also depend on the type of metal used as the electrode. The values of the size of the depletion layer and the electric field are also in agreement with the theoretical values from Ashcroft et al., 1976[142] and Sze et al., 2006[86]. The theoretical values obtained by Ashcroft et al., 1976[142] and Sze et al., 2006[86] for the width of the depletion layer is of the range $10^{-6} - 10^{-4}\ cm$, and the for the electric field it ranges from $10^4 - 10^5\ V/cm$. The contact resistance is also dependent on the barrier height. The contact resistance is small for low barrier heights, which means that there will be less resistance for the electrons to move from the metal to the semiconductor. The electric field and the size of the depletion layer increases when adding dopants to intrinsic a-Si. Thus, the n and p doped layers were prepared for the fabrication of p-i-n a-Si:H solar cell to optimize the sizes of the different layers.

The size of the NPs used to improve the efficiencies of the commercial a-Si solar cells was found to be dependent on the deposition time. The plasmonic resonance for Ag and Au NPs absorption spans from 400 nm to 800 nm. Au NPs have exhibited better plasmonic response than Ag NPs as the resonance band matches the bandgap of the commercial a-Si solar cell investigated. $ZnO : Tb^{3+}$ layers increases the efficiency of the commercial a-Si devices and when the NPs (Au and Ag) are added to the layer, the efficiency of the a-Si device increases even further. Annealed commercial a-Si devices with a spectral conversion layer and NPs showed decreased efficiency of the a-Si device, but an annealed a-Si device with only the spectral conversion layer showed increased efficiency compared with the ones with just the NPs. These findings indicate a very complex interplay between absorption and photon conversion in the vicinity of the plasmonic nanoparticles, which has to be explored in much more detail to drastically improve the efficiency of the type of solar cells examined in this study.

6.2 Future Work

During the course of this project, several new ideas emerged to increase the efficiency of the fabricated and the commercial a-Si devices. These ideas includes the modification of the active layer in the device and a better control over the incoming solar photons. The following ideas that should be investigated in the future are:

- Embedding NPs on top of the i-layer and the n-layer.
- Depositing an intrinsic layer of 300 nm of thickness between the n-type and p-type layers.
- Spectral conversion using ZnO layers doped with either Eu^{3+} and Nd^{3+} ions on top of the commercial a-Si solar cells.
- Adding Ag and Au NPs at various layers of the fabricated a-Si:H device.
- Annealing of the ZnO:RE layers at temperatures higher than $150°C$, but less than $500\ °C$.
- Fabrication of the entire a-Si:H solar cell using P or using Sb dopants supplied through diffusion driven processes.
- A Transmission Electron Microscope (TEM) with a higher resolution will be used to distinguish between single particles and clumps of particles.

References

[1] M. Asif and T. Muneer, "Energy supply, its demand and security issues for developed and emerging economies," *Renewable and Sustainable Energy Reviews*, vol. 11, no. 7, pp. 1388–1413, 2007.

[2] S. Ahmed, M. Islam, M. Karim, and N. Karim, "Exploitation of renewable energy for sustainable development and overcoming power crisis in bangladesh," *Renewable Energy*, vol. 72, pp. 223–235, 2014.

[3] A. Amevi, "Performance analysis of particle swarm optimization approach for optimizing electricity cost from a hybrid solar, wind and hydropower plant," *International Journal of Renewable Energy Research (IJRER)*, vol. 6, no. 1, pp. 323–334, 2016.

[4] R. Pelc and R. Fujita, "Renewable energy from the ocean," *Marine Policy*, vol. 26, no. 6, pp. 471–479, 2002.

[5] N. Wang and V. Dalal, "Improving stability of amorphous silicon using chemical annealing with helium," *Journal of Non-Crystalline Solids*, vol. 352, no. 9, pp. 1937–1940, 2006.

[6] M. Aresta, A. Dibenedetto, and A. Angelini, "Catalysis for the valorization of exhaust carbon: from co2 to chemicals, materials, and fuels. technological use of co2," *Chemical Reviews*, vol. 114, no. 3, pp. 1709–1742, 2013.

[7] E. Klugmann-Radziemska, "Environmental impacts of renewable energy technologies," *International Proceedings of Chemical, Biological and Environmental Engineering (IPCBEE)*, vol. 69, pp. 104–108, 2014.

[8] J. Carabe and J. Gandia, "Thin-film-silicon solar cells," *Opto-Electronics Review*, vol. 12, no. 1, pp. 1–6, 2004.

[9] H. Möller, *Semiconductors for solar cells.* Artech House Publishers, 1993.

[10] A. Kuhlmann, "The second most abundant element in the earth's crust," *Journal of Management*, vol. 15, no. 7, pp. 502–505, 1963.

[11] A. Feltrin and A. Freundlich, "Material considerations for terawatt level deployment of photovoltaics," *Renewable Energy*, vol. 33, no. 2, pp. 180–185, 2008.

[12] G. Conibeer, M. Green, R. Corkish, Y. Cho, E. Cho, C. Jiang, T. Fangsuwannarak, E. Pink, Y. Huang, and T. Puzzer, "Silicon nanostructures for third generation photovoltaic solar cells," *Thin Solid Films*, vol. 511, pp. 654–662, 2006.

[13] H. Seidel, L. Csepregi, A. Heuberger, and H. Baumgärtel, "Anisotropic etching of crystalline silicon in alkaline solutions i. orientation dependence and behavior of passivation layers," *Journal of the Electrochemical Society*, vol. 137, no. 11, pp. 3612–3626, 1990.

[14] E. Yablonovitch, D. Allara, C. Chang, T. Gmitter, and T. Bright, "Unusually low surface-recombination velocity on silicon and germanium surfaces," *Physical Review Letters*, vol. 57, no. 2, p. 249, 1986.

[15] W. Kern, "The evolution of silicon wafer cleaning technology," *Journal of the Electrochemical Society*, vol. 137, no. 6, pp. 1887–1892, 1990.

[16] A. McEvoy, T. Markvart, L. Castañer, T. Markvart, and L. Castaner, *Practical handbook of photovoltaics: fundamentals and applications.* Elsevier, 2003.

[17] P. Sánchez, O. Lorenzo, A. Menéndez, J. Menéndez, D. Gomez, R. Pereiro, and B. Fernández, "Characterization of doped amorphous silicon thin films through the investigation of dopant elements by glow discharge spectrometry: A correlation of conductivity and bandgap energy measurements," *International journal of molecular sciences*, vol. 12, no. 4, pp. 2200–2215, 2011.

[18] L. Mercaldo, M. Addonizio, M. Della Noce, P. Veneri, A. Scognamiglio, and C. Privato, "Thin film silicon photovoltaics: architectural perspectives and technological issues," *Applied Energy*, vol. 86, no. 10, pp. 1836–1844, 2009.

[19] L. Froideval, *A study of solar radiation pressure acting on GPS satellites.* PhD thesis, 2009.

[20] F. Alharbi, J. Bass, A. Salhi, A. Alyamani, H. Kim, and R. Miller, "Abundant non-toxic materials for thin film solar cells: Alternative to conventional materials," *Renewable Energy*, vol. 36, no. 10, pp. 2753–2758, 2011.

[21] N. Haegel, R. Margolis, T. Buonassisi, D. Feldman, A. Froitzheim, R. Garabedian, M. Green, S. Glunz, H. Henning, B. Holder, *et al.*, "Terawatt-scale photovoltaics: Trajectories and challenges," *Science*, vol. 356, no. 6334, pp. 141–143, 2017.

[22] C. Archer and M. Jacobson, "Supplying baseload power and reducing transmission requirements by interconnecting wind farms," *Journal of Applied Meteorology and Climatology*, vol. 46, no. 11, pp. 1701–1717, 2007.

[23] J. Houghton, *Climate change 1995: The science of climate change: contribution of working group I to the second assessment report of the Intergovernmental Panel on Climate Change*, vol. 2. Cambridge University Press, 1996.

[24] J. Nelson, *The physics of solar cells.* World Scientific Publishing Co Inc, 2003.

[25] J. Bao, *A study of a Fe_2O_3 thin films for the oxygen evolution reaction in water photolysis.* PhD thesis, 2010.

[26] A. Falk, C. Durschner, and K. Remmers, *Photovoltaics for professionals: solar electric systems marketing, design and installation.* Routledge, 2013.

[27] A. Al-Mebir, *Effect of In Situ Thermal Annealing Process on Structural, Optical and Electrical Properties of CdS\CdTe Thin-Film Solar Cells Fabricated by Pulsed Laser Deposition.* PhD thesis, University of Kansas, 2015.

[28] W. Adams and R. Day, "V. the action of light on selenium," *Proceedings of the Royal Society of London*, vol. 25, no. 171-178, pp. 113–117, 1877.

[29] C. Fritts, "On a new form of selenium cell, and some electrical discoveries made by its use," *American Journal of Science*, no. 156, pp. 465–472, 1883.

[30] L. Grondahl, "The copper-cuprous-oxide rectifier and photoelectric cell," *Reviews of Modern Physics*, vol. 5, no. 2, p. 141, 1933.

[31] Y. Yu, J. Liu, H. Wang, and M. Liu, "Assess the potential of solar irrigation systems for sustaining pasture lands in arid regions–a case study in northwestern china," *Applied Energy*, vol. 88, no. 9, pp. 3176–3182, 2011.

[32] J. Carlé and F. Krebs, "Technological status of organic photovoltaics (opv)," *Solar Energy Materials and Solar Cells*, vol. 119, pp. 309–310, 2013.

[33] A. Bagher, M. A. Vahid, and M. Mohsen, "Types of solar cells and application," *American Journal of Optics and Photonics*, vol. 3, no. 5, pp. 94–113, 2015.

[34] T. Tromholt, M. Madsen, J. Carlé, M. Helgesen, and F. Krebs, "Photochemical stability of conjugated polymers, electron acceptors and blends for polymer solar cells resolved in terms of film thickness and absorbance," *Journal of Materials Chemistry*, vol. 22, no. 15, pp. 7592–7601, 2012.

[35] R. Messenger and A. Abtahi, *Photovoltaic systems engineering.* CRC press, 2017.

[36] Y. Hamakawa, *Thin-film solar cells: next generation photovoltaics and its applications*, vol. 13. Springer Science & Business Media, 2013.

[37] A. Yella, H. Lee, H. Tsao, C. Yi, A. K. Chandiran, M. Nazeeruddin, E. Diau, C. Yeh, S. Zakeeruddin, and M. Grätzel, "Porphyrin-sensitized solar cells with cobalt (ii/iii)–based redox electrolyte exceed 12 percent efficiency," *Science*, vol. 334, no. 6056, pp. 629–634, 2011.

[38] L. Pericherla, *Designing of Amorphous Silicon Solar Cells for Optimal Photovoltaic Performance.* PhD thesis, Charles Darwin University at Casuarina, 2013.

[39] J. Perlin, *From space to earth: the story of solar electricity.* Earthscan, 1999.

[40] C. Xue and X. Sun, "Design for amorphous silicon solar cells," vol. 750, no. 2, pp. 961–964, 2013.

[41] X. Deng and E. Schiff, "Amorphous silicon based solar cells," *Solar Energy Materials and Solar Cells*, vol. 78, no. 1, pp. 567–595, 2003.

[42] W. Qarony, M. Hossain, M. Hossain, M. Uddin, A. Haque, A. Saad, and Y. Tsang, "Efficient amorphous silicon solar cells: characterization, optimization, and optical loss analysis," *Results in Physics*, vol. 7, pp. 4287–4293, 2017.

[43] D. Zhou, *Light-trapping enhancement in thin film solar cells with photonic crystals.* PhD thesis, 2008.

[44] S. Ahn, S. Lee, and H. Lee, "Toward commercialization of triple-junction thin-film silicon solar panel with¿ 12% efficiency," in *27th European Photovoltaic Solar Energy Conference*, 2012.

[45] M. Green, "Photovoltaic principles," *Physica E: Low-dimensional Systems and Nanostructures*, vol. 14, no. 1, pp. 11–17, 2002.

[46] B. Parida, S. Iniyan, and R. Goic, “A review of solar photovoltaic technologies,” *Renewable and Sustainable Energy Reviews*, vol. 15, no. 3, pp. 1625–1636, 2011.

[47] L. Allen, “Electronegativity is the average one-electron energy of the valence-shell electrons in ground-state free atoms,” *Journal of the American Chemical Society*, vol. 111, no. 25, pp. 9003–9014, 1989.

[48] R. Bube and A. Fahrenbruch, “Fundamentals of solar cells,” *Academic Press, London, New York*, p. 425, 1983.

[49] S. Wenham, *Applied photovoltaics.* Routledge, 2012.

[50] P. Chen, D. Zhao, D. Jiang, H. Long, M. Li, J. Yang, J. Zhu, Z. Liu, X. Li, W. Liu, *et al.*, “Electroluminescence property improvement by adjusting quantum wells’ position relative to p-doped region in ingan/gan multiple-quantum-well light emitting diodes,” *AIP Advances*, vol. 7, no. 3, p. 035103, 2017.

[51] U. Würfel, A. Cuevas, and P. Würfel, “Charge carrier separation in solar cells,” *IEEE Journal of Photovoltaics*, vol. 5, no. 1, pp. 461–469, 2015.

[52] K. Vivek and G. Agrawal, “Organic solar cells: Principles mechanism and recent developments,” *Hypothesis*, vol. 17, p. 18, 2014.

[53] G. Calogero, A. Bartolotta, G. Di Marco, A. Di Carlo, and F. Bonaccorso, “Vegetable-based dye-sensitized solar cells,” *Chemical Society Reviews*, vol. 44, no. 10, pp. 3244–3294, 2015.

[54] N. Mayimele, “Approaches to enhance optical absorption and efficiency of photovoltaic device,” Master’s thesis, University of the Witwatersrand, 2017.

[55] H. Spanggaard and F. Krebs, “A brief history of the development of organic and polymeric photovoltaics,” *Solar Energy Materials and Solar Cells*, vol. 83, no. 2, pp. 125–146, 2004.

[56] H. Hoppe and N. Sariciftci, “Organic solar cells: An overview,” *Journal of Materials Research*, vol. 19, no. 7, pp. 1924–1945, 2004.

[57] R. Chiechi, R. Havenith, J. Hummelen, L. Koster, and M. Loi, “Modern plastic solar cells: materials, mechanisms and modeling,” *Materials Today*, vol. 16, no. 7, pp. 281–289, 2013.

[58] H. Bässler and A. Köhler, “Charge transport in organic semiconductors,” in *Unimolecular and Supramolecular Electronics I*, pp. 1–65, Springer, 2011.

[59] X. Zhu, Q. Yang, and M. Muntwiler, “Charge-transfer excitons at organic semiconductor surfaces and interfaces,” *Accounts of Chemical Research*, vol. 42, no. 11, pp. 1779–1787, 2009.

[60] G. Wetzelaer and P. Blom, “Diffusion-driven currents in organic-semiconductor diodes,” *NPG Asia Materials*, vol. 6, no. 7, p. e110, 2014.

[61] A. Baumann, T. Savenije, D. Murthy, M. Heeney, V. Dyakonov, and C. Deibel, “Influence of phase segregation on recombination dynamics in organic bulk-heterojunction solar cells,” *Advanced Functional Materials*, vol. 21, no. 9, pp. 1687–1692, 2011.

[62] E. Verploegen, R. Mondal, C. Bettinger, S. Sok, M. Toney, and Z. Bao, “Effects of thermal annealing upon the morphology of polymer–fullerene blends,” *Advanced Functional Materials*, vol. 20, no. 20, pp. 3519–3529, 2010.

[63] A. Goetzberger, J. Luther, and G. Willeke, “Solar cells: past, present, future,” *Solar Energy Materials and Solar Cells*, vol. 74, no. 1, pp. 1–11, 2002.

[64] J. Maier, *Physical chemistry of ionic materials: ions and electrons in solids*. John Wiley & Sons, 2004.

[65] B. Shklovskii and A. Efros, *Electronic properties of doped semiconductors*, vol. 45. Springer Science & Business Media, 2013.

[66] S. Pantelides, “The electronic structure of impurities and other point defects in semiconductors,” *Reviews of Modern Physics*, vol. 50, no. 4, p. 797, 1978.

[67] L. Costa, F. Silva, and C. Comin, “An early model of transistors,” *arXiv preprint arXiv:1701.02269*, 2017.

[68] A. Shah, P. Torres, R. Tscharner, N. Wyrsch, and H. Keppner, “Photovoltaic technology: the case for thin-film solar cells,” *Science*, vol. 285, no. 5428, pp. 692–698, 1999.

[69] P. Hersch and K. Zweibel, “Basic photovoltaic principles and methods,” tech. rep., Solar Energy Research Inst., Golden, CO (USA), 1982.

[70] B. Modtland, *Improving the light-induced degradation of hydrogenated amorphous silicon solar cells using fabrication at elevated temperatures and low pressure*. PhD thesis, Iowa State University, 2013.

[71] T. Razykov, C. Ferekides, D. Morel, E. Stefanakos, H. Ullal, and H. Upadhyaya, “Solar photovoltaic electricity: Current status and future prospects,” *Solar Energy*, vol. 85, no. 8, pp. 1580–1608, 2011.

[72] A. Madan and M. Shaw, *The physics and applications of amorphous semiconductors*. Elsevier, 2012.

[73] M. Keevers and M. Green, “Efficiency improvements of silicon solar cells by the impurity photovoltaic effect,” *Journal of Applied Physics*, vol. 75, no. 8, pp. 4022–4031, 1994.

[74] J. Bisquert, D. Cahen, G. Hodes, S. Rühle, and A. Zaban, “Physical chemical principles of photovoltaic conversion with nanoparticulate, mesoporous dye-sensitized solar cells,” *The Journal of Physical Chemistry B*, vol. 108, no. 24, pp. 8106–8118, 2004.

[75] V. Ferry, J. Munday, and H. Atwater, “Design considerations for plasmonic photovoltaics,” *Advanced Materials*, vol. 22, no. 43, pp. 4794–4808, 2010.

[76] N. Asim, K. Sopian, S. Ahmadi, K. Saeedfar, M. Alghoul, O. Saadatian, and S. Zaidi, “A review on the role of materials science in solar cells,” *Renewable and Sustainable Energy Reviews*, vol. 16, no. 8, pp. 5834–5847, 2012.

[77] W. Hou and S. Cronin, “A review of surface plasmon resonance-enhanced photocatalysis,” *Advanced Functional Materials*, vol. 23, no. 13, pp. 1612–1619, 2013.

[78] W. Ye, R. Long, H. Huang, and Y. Xiong, “Plasmonic nanostructures in solar energy conversion,” *Journal of Materials Chemistry C*, vol. 5, no. 5, pp. 1008–1021, 2017.

[79] L. Novotny, B. Hecht, and D. Pohl, “Interference of locally excited surface plasmons,” *Journal of Applied Physics*, vol. 81, no. 4, pp. 1798–1806, 1997.

[80] D. Derkacs, S. Lim, P. Matheu, W. Mar, and E. Yu, “Improved performance of amorphous silicon solar cells via scattering from surface plasmon polaritons in nearby metallic nanoparticles,” *Applied Physics Letters*, vol. 89, no. 9, p. 093103, 2006.

[81] S. Lim, W. Mar, P. Matheu, D. Derkacs, and E. Yu, “Photocurrent spectroscopy of optical absorption enhancement in silicon photodiodes via scattering from surface plasmon polaritons in gold nanoparticles,” *Journal of Applied Physics*, vol. 101, no. 10, p. 104309, 2007.

[82] V. Ferry, M. Verschuuren, H. Li, E. Verhagen, R. Walters, R. Schropp, H. Atwater, and A. Polman, “Light trapping in ultrathin plasmonic solar cells,” *Optics Express*, vol. 18, no. 102, pp. A237–A245, 2010.

[83] H. Atwater and A. Polman, “Plasmonics for improved photovoltaic devices,” *Nature Materials*, vol. 9, no. 3, pp. 205–213, 2010.

[84] A. Ghahremani and A. Fathy, “High efficiency thin-film amorphous silicon solar cells,” *Energy Science & Engineering*, vol. 4, no. 5, pp. 334–343, 2016.

[85] M. Gracia, F. Rojas, and G. Gordillo, “Morphological and optical characterization of sno2: F thin films deposited by spray pyrolysis,” in *20th European Photovoltaic Solar Energy Conference*, pp. 6–10, 2005.

[86] S. Sze and K. Ng, *Physics of semiconductor devices.* John wiley & Sons, 2006.

[87] D. Neamen, *Semiconductor physics and devices*, vol. 3. McGraw-Hill New York, 1997.

[88] O. Madelung, *Semiconductors: data handbook.* Springer Science & Business Media, 2012.

[89] R. Santbergen, R. Liang, and M. Zeman, “A-si: H solar cells with embedded silver nanoparticles,” in *Photovoltaic Specialists Conference (PVSC), 2010 35th IEEE*, pp. 000748–000753, IEEE, 2010.

[90] A. Aden and M. Kerker, “Scattering of electromagnetic waves from two concentric spheres,” *Journal of Applied Physics*, vol. 22, no. 10, pp. 1242–1246, 1951.

[91] H. van de Hulst, *Light Scattering by Small Particles.* Courier Corporation, 2012.

[92] M. van Dijk, A. Tchebotareva, M. Orrit, M. Lippitz, S. Berciaud, D. Lasne, L. Cognet, and B. Lounis, "Absorption and scattering microscopy of single metal nanoparticles," *Physical Chemistry Chemical Physics*, vol. 8, no. 30, pp. 3486–3495, 2006.

[93] A. Ghahremani and A. Fathy, "Strategies for designing high efficient thin-film amorphous silicon solar cells," in *Photovoltaic Specialist Conference (PVSC), 2015 IEEE 42nd*, pp. 1–4, IEEE, 2015.

[94] T. Aaltonen, M. Alnes, O. Nilsen, L. Costelle, and H. Fjellvåg, "Lanthanum titanate and lithium lanthanum titanate thin films grown by atomic layer deposition," *Journal of Materials Chemistry*, vol. 20, no. 14, pp. 2877–2881, 2010.

[95] W. Van Sark, A. Meijerink, and R. Schropp, "Solar spectrum conversion for photovoltaics using nanoparticles," in *Third Generation Photovoltaics*, InTech, 2012.

[96] M. Alkiswani, "Spectrum conversion in solar cells industry: Novel model concept and steps towards commercialization," Master's thesis, Halmstad University, Sweden, 2015.

[97] F. Auzel, "Upconversion and anti-stokes processes with f and d ions in solids," *Chemical Reviews*, vol. 104, no. 1, pp. 139–174, 2004.

[98] L. Aarts, *Downconversion for solar cells with lanthanide ion couples.* PhD thesis, Utrecht University, 2009.

[99] N. Bloembergen, "Solid state infrared quantum counters," *Physical Review Letters*, vol. 2, no. 3, p. 84, 1959.

[100] V. Saxena, "Phosphors for solar-cells-tb-doped lanthanum fluoride and th-doped calcium tungstate," *Indian Journal of Pure & Applied Physics*, vol. 21, no. 5, pp. 306–307, 1983.

[101] J. Goldschmidt, S. Fischer, B. Herter, B. Fröhlich, K. Krämer, B. Richards, A. Ivaturi, S. MacDougall, J. Hueso, E. Favilla, *et al.*, "Record efficient upconverter solar cell devices," in *29th Eur. PV Sol. Energy Conf. Exhib., Amsterdam, The Netherlands*, 2014.

[102] W. van Sark, J. de Wild, J. Rath, A. Meijerink, and R. Schropp, "Upconversion in solar cells," *Nanoscale Research Letters*, vol. 8, no. 1, p. 81, 2013.

[103] A. Shalav, B. Richards, T. Trupke, K. Krämer, and H. Güdel, "Application of $NaYF_4 : Er^{3+}$ up-converting phosphors for enhanced near-infrared silicon solar cell response," *Applied Physics Letters*, vol. 86, no. 1, p. 013505, 2005.

[104] X. Liang, X. Huang, and Q. Zhang, "$Gd_2(MoO_4)_3 : Er^{3+}$ nanophosphors for an enhancement of silicon solar-cell near-infrared response," *Journal of Fluorescence*, vol. 19, no. 2, pp. 285–289, 2009.

[105] F. Lahoz, "Ho^{3+} doped nanophase glass ceramics for efficiency enhancement in silicon solar cells," *Optics Letters*, vol. 33, no. 24, pp. 2982–2984, 2008.

[106] B. Van Der Ende, L. Aarts, and A. Meijerink, “Lanthanide ions as spectral converters for solar cells,” *Physical Chemistry Chemical Physics*, vol. 11, no. 47, pp. 11081–11095, 2009.

[107] Y. Shang, S. Hao, C. Yang, and G. Chen, “Enhancing solar cell efficiency using photon upconversion materials,” *Nanomaterials*, vol. 5, no. 4, pp. 1782–1809, 2015.

[108] P. Gibart, F. Auzel, J. Guillaume, and K. Zahraman, “Below band-gap ir response of substrate-free gaas solar cells using two-photon up-conversion,” *Japanese Journal of Applied Physics*, vol. 35, no. 8R, p. 4401, 1996.

[109] J. De Wild, A. Meijerink, J. Rath, W. Van Sark, and R. Schropp, “Towards upconversion for amorphous silicon solar cells,” *Solar Energy Materials and Solar Cells*, vol. 94, no. 11, pp. 1919–1922, 2010.

[110] M. Liu, Y. Lu, Z. Xie, and G. Chow, “Enhancing near-infrared solar cell response using upconverting transparentceramics,” *Solar Energy Materials and Solar Cells*, vol. 95, no. 2, pp. 800–803, 2011.

[111] J. De Wild, T. Duindam, J. K. Rath, A. Meijerink, W. Van Sark, and R. Schropp, “Increased upconversion response in a-Si: H solar cells with broad-band light,” *IEEE Journal of Photovoltaics*, vol. 3, no. 1, pp. 17–21, 2013.

[112] J. Jakutis, L. Gomes, C. Amancio, L. Kassab, J. Martinelli, and N. Wetter, “Increased Er^{3+} upconversion in tellurite fibers and glasses by co-doping with Yb^{3+},” *Optical Materials*, vol. 33, no. 1, pp. 107–111, 2010.

[113] J. de Wild, J. Rath, A. Meijerink, W. Van Sark, and R. Schropp, “Enhanced near-infrared response of a-si: H solar cells with $\beta - NaYF_4 : Yb^{3+}(18\%), Er^{3+}(2\%)$ upconversion phosphors,” *Solar Energy Materials and Solar Cells*, vol. 94, no. 12, pp. 2395–2398, 2010.

[114] F. Yang, C. Liu, D. Wei, Y. Chen, J. Lu, and S. Yang, “$Er^{3+} - Yb^{3+}$ co-doped $TeO_2 - PbF_2$ oxyhalide tellurite glasses for amorphous silicon solar cells,” *Optical Materials*, vol. 36, no. 6, pp. 1040–1043, 2014.

[115] C. Joshi and S. Rai, “Structural, thermal, and optical properties of Pr^{3+}/Yb^{3+} co-doped oxyhalide tellurite glasses and its nano-crystalline parts,” *Solid State Sciences*, vol. 14, no. 8, pp. 997–1003, 2012.

[116] J. Suyver, A. Aebischer, D. Biner, P. Gerner, J. Grimm, S. Heer, K. Krämer, C. Reinhard, and H. Güdel, “Novel materials doped with trivalent lanthanides and transition metal ions showing near-infrared to visible photon upconversion,” *Optical Materials*, vol. 27, no. 6, pp. 1111–1130, 2005.

[117] M. Malinowski, M. Joubert, and B. Jacquier, “Infrared to blue up-conversion in Pr^{3+} doped YAG and $LiYF_4$ crystals,” *Journal of Luminescence*, vol. 60, pp. 179–182, 1994.

[118] O. Wenger, D. Gamelin, H. Güdel, A. Butashin, and A. Kaminskii, “Site-selective yellow to violet and near-infrared to green upconversion in $BaLu_2F_8 : Nd^{3+}$,” *Physical Review B*, vol. 61, no. 24, p. 16530, 2000.

[119] M. Wermuth, T. Riedener, and H. Güdel, "Spectroscopy and upconversion mechanisms of $CsCdBr_3 : Dy^{3+}$," *Physical Review B*, vol. 57, no. 8, p. 4369, 1998.

[120] M. Pollnau, D. Gamelin, S. Lüthi, H. Güdel, and M. Hehlen, "Power dependence of upconversion luminescence in lanthanide and transition-metal-ion systems," *Physical Review B*, vol. 61, no. 5, p. 3337, 2000.

[121] O. Savchuk, "Experimental techniques," *Development of new materials and techniques for luminescence nanothermometry and photothermal conversion*, p. 59.

[122] M. Joubert, S. Guy, S. Cuerq, and P. Tanner, "Room temperature blue upconverted luminescence via photon avalanche pumping in $Cs_2NaGdCL_6 : Tm^{3+}$," *Journal of Luminescence*, vol. 75, no. 4, pp. 287–293, 1997.

[123] B. Henderson and G. Imbusch, *Optical spectroscopy of inorganic solids*, vol. 44. Oxford University Press, 2006.

[124] J. Vuojola and T. Soukka, "Luminescent lanthanide reporters: new concepts for use in bioanalytical applications," *Methods and applications in fluorescence*, vol. 2, no. 1, p. 012001, 2014.

[125] D. Verma, T. Saetre, and O. Midtgård, "Review on up/down conversion materials for solar cell application," in *Photovoltaic Specialists Conference (PVSC), 2012 38th IEEE*, pp. 002608–002613, IEEE, 2012.

[126] D. Dexter, "Possibility of luminescent quantum yields greater than unity," *Physical Review*, vol. 108, no. 3, p. 630, 1957.

[127] W. Piper, J. DeLuca, and F. Ham, "Cascade fluorescent decay in Pr^{3+} doped fluorides: Achievement of a quantum yield greater than unity for emission of visible light," *Journal of Luminescence*, vol. 8, no. 4, pp. 344–348, 1974.

[128] J. Sommerdijk, A. Bril, and A. De Jager, "Two photon luminescence with ultraviolet excitation of trivalent praseodymium," *Journal of Luminescence*, vol. 8, no. 4, pp. 341–343, 1974.

[129] T. Trupke, M. Green, and P. Würfel, "Improving solar cell efficiencies by down-conversion of high-energy photons," *Journal of Applied Physics*, vol. 92, no. 3, pp. 1668–1674, 2002.

[130] P. Vergeer, T. Vlugt, M. Kox, M. Den Hertog, J. Van der Eerden, and A. Meijerink, "Quantum cutting by cooperative energy transfer in $Yb(YPO_4) : Tb^{3+}$," *Physical Review B*, vol. 71, no. 1, p. 014119, 2005.

[131] B. Richards, "Luminescent layers for enhanced silicon solar cell performance: Down-conversion," *Solar energy materials and solar cells*, vol. 90, no. 9, pp. 1189–1207, 2006.

[132] F. Braun, "Ferdinand braun, pogg. ann., vol. 153, p. 556, 1874," *Pogg. Ann.*, vol. 153, p. 556, 1874.

[133] Y. Bai, H. Huang, C. Wang, R. Long, and Y. Xiong, "Engineering the surface charge states of nanostructures for enhanced catalytic performance," *Materials Chemistry Frontiers*, vol. 1, no. 10, pp. 1951–1964, 2017.

[134] W. Schottky, "Halbleitertheorie der sperrschicht," *Naturwissenschaften*, vol. 26, no. 52, pp. 843–843, 1938.

[135] K. Brennan, *Introduction to semiconductor devices: for computing and telecommunications applications.* Cambridge University Press, 2005.

[136] O. Isabella, A. Smets, K. Jäger, M. Zeman, and R. van Swaaij, "Solar energy: The physics and engineering of photovoltaic conversion, technologies and systems," *UIT Cambridge Limited*, 2016.

[137] B. Streetman and S. Banerjee, *Solid State Electronic Devices: Global Edition.* Pearson education, 2016.

[138] B. Pellegrini, "A detailed analysis of the metal-semiconductor contact," *Solid-State Electronics*, vol. 17, no. 3, pp. 217–237, 1974.

[139] M. Brezeanu, *Diamond Schottky barrier diodes.* PhD thesis, University of Cambridge, 2008.

[140] E. Macabebe and E. Van Dyk, "Parameter extraction from dark current-voltage characteristics of solar cells," *South African Journal of Science*, vol. 104, no. 9-10, pp. 401–404, 2008.

[141] H. Bethe, "Theory of the boundary layer of crystal rectifiers," in *Semiconductor Devices: Pioneering Papers*, pp. 387–399, World Scientific, 1991.

[142] N. W. Ashcroft and N. Mermin, "Solid state physics," *Saunders College Publishing, Orlando, Florida,*, 1976.

[143] M. V. Fischetti, "Monte carlo simulation of transport in technologically significant semiconductors of the diamond and zinc-blende structures. i. homogeneous transport," *IEEE Transactions on Electron Devices*, vol. 38, no. 3, pp. 634–649, 1991.

[144] K. K. Ng, "A survey of semiconductor devices," *IEEE Transactions on Electron Devices*, vol. 43, no. 10, pp. 1760–1766, 1996.

[145] O. Philips'Gloeilampenfabrieken, "A method of measuring specific resistivity and hall effect of discs of arbitrary shape," *Philips Res. Rep*, vol. 13, no. 1, pp. 1–9, 1958.

[146] C. Chen, A. de Castro, and Y. Shen, "Surface-enhanced second-harmonic generation," *Physical Review Letters*, vol. 46, no. 2, p. 145, 1981.

[147] G. Hornyak, C. Patrissi, and C. Martin, "Fabrication, characterization, and optical properties of gold nanoparticle/porous alumina composites: The nonscattering maxwell- garnett limit," *The Journal of Physical Chemistry B*, vol. 101, no. 9, pp. 1548–1555, 1997.

[148] A. Camacho, "Focusing nanoplasmonics," *J. Nano Sc. Tech*, vol. 3, pp. 10–17, 2015.

[149] W. Erwin, H. Zarick, E. Talbert, and R. Bardhan, "Light trapping in mesoporous solar cells with plasmonic nanostructures," *Energy & Environmental Science*, vol. 9, no. 5, pp. 1577–1601, 2016.

[150] M. Brongersma and P. Kik, *Surface plasmon nanophotonics.* Springer, 2007.

[151] K. Chang, "Tiny is beautiful, translating "nano" into practical," *The New York Times*, vol. 22, 2005.

[152] J. Lee and P. Peumans, "The origin of enhanced optical absorption in solar cells with metal nanoparticles embedded in the active layer," *Optics Express*, vol. 18, no. 10, pp. 10078–10087, 2010.

[153] L. Novotny and B. Hecht, *Principles of nano-optics.* Cambridge university press, 2012.

[154] J. Zhang, L. Zhang, and W. Xu, "Surface plasmon polaritons: physics and applications," *Journal of Physics D: Applied Physics*, vol. 45, no. 11, p. 113001, 2012.

[155] S. Maier, *Plasmonics: fundamentals and applications.* Springer Science & Business Media, 2007.

[156] C. Bohren and D. Huffman, *Absorption and scattering of light by small particles.* John Wiley & Sons, 2008.

[157] A. Pennanen, "Enhancing silicon solar cell efficiency with metal nanoparticles," Master's thesis, University of jyvaskyla in Finland, 2009.

[158] A. Zayats, I. Smolyaninov, and A. Maradudin, "Nano-optics of surface plasmon polaritons," *Physics Reports*, vol. 408, no. 3-4, pp. 131–314, 2005.

[159] S. Rahman, I. Chowdhury, S. Siddha, M. Hasan, *et al.*, *Localized surface plasmon resonance in bimetallic core-shell nanoparticles.* PhD thesis, BRAC University, 2016.

[160] J. Jackson, "Classical electrodynamics (wiley, new york)(1998)," *Google Scholar*, p. 78.

[161] A. Pinchuk, G. Von Plessen, and U. Kreibig, "Influence of interband electronic transitions on the optical absorption in metallic nanoparticles," *Journal of Physics D: Applied Physics*, vol. 37, no. 22, p. 3133, 2004.

[162] S. Bilankohi, "Optical scattering and absorption characteristics of silver and silica/silver core/shell nanoparticles," *Oriental Journal of Chemistry*, vol. 31, no. 4, pp. 2259–2263, 2015.

[163] W. Murray and W. Barnes, "Plasmonic materials," *Advanced Materials*, vol. 19, no. 22, pp. 3771–3782, 2007.

[164] V. Jacobsen, P. Stoller, C. Brunner, V. Vogel, and V. Sandoghdar, "Interferometric optical detection and tracking of very small gold nanoparticles at a water-glass interface," *Optics Express*, vol. 14, no. 1, pp. 405–414, 2006.

[165] H. Toma, V. Zamarion, S. Toma, and K. Araki, "The coordination chemistry at gold nanoparticles," *Journal of the Brazilian Chemical Society*, vol. 21, no. 7, pp. 1158–1176, 2010.

[166] E. Prodan, C. Radloff, N. Halas, and P. Nordlander, "A hybridization model for the plasmon response of complex nanostructures," *Science*, vol. 302, no. 5644, pp. 419–422, 2003.

[167] M. Rycenga, M. Langille, M. Personick, T. Ozel, and C. Mirkin, "Chemically isolating hot spots on concave nanocubes," *Nano Letters*, vol. 12, no. 12, pp. 6218–6222, 2012.

[168] M. Ngom, *Novel Approach to the Study of Surface Plasmon Resonance and Field Enhancement Properties of Noble Metal Nanostructures.* PhD thesis, University of Michigan, 2009.

[169] S. Pillai, K. Catchpole, T. Trupke, and M. Green, "Surface plasmon enhanced silicon solar cells," *Journal of Applied Physics*, vol. 101, no. 9, p. 093105, 2007.

[170] K. Baba, T. Okuno, and M. Miyagi, "Silver-gold compound metal island films prepared by using a two-step evaporation method," *Applied Physics Letters*, vol. 62, no. 5, pp. 437–439, 1993.

[171] D. Sigle, E. Perkins, J. Baumberg, and S. Mahajan, "Reproducible deep-uv serrs on aluminum nanovoids," *The Journal of Physical Chemistry Letters*, vol. 4, no. 9, pp. 1449–1452, 2013.

[172] T. Ding, D. Sigle, L. Herrmann, D. Wolverson, and J. Baumberg, "Nanoimprint lithography of al nanovoids for deep-uv sers," *ACS Applied Materials & Interfaces*, vol. 6, no. 20, pp. 17358–17363, 2014.

[173] Y. Akimov and W. Koh, "Resonant and nonresonant plasmonic nanoparticle enhancement for thin-film silicon solar cells," *Nanotechnology*, vol. 21, no. 23, p. 235201, 2010.

[174] H. Rigneault, J. Lourtioz, C. Delalande, and A. Levenson, *Nanophotonics*, vol. 102. John Wiley & Sons, 2010.

[175] H. Fischer and O. J. Martin, "Engineering the optical response of plasmonic nanoantennas," *Optics Express*, vol. 16, no. 12, pp. 9144–9154, 2008.

[176] S. Pillai and M. Green, "Plasmonics for photovoltaic applications," *Solar Energy Materials and Solar Cells*, vol. 94, no. 9, pp. 1481–1486, 2010.

[177] N. Burford, *Plasmonic nanostructures for the absorption enhancement of silicon solar cells.* PhD thesis, University of Arkansas in Fayetteville, 2013.

[178] J. Mertz, "Radiative absorption, fluorescence, and scattering of a classical dipole near a lossless interface: a unified description," *JOSA B*, vol. 17, no. 11, pp. 1906–1913, 2000.

[179] N. King, M. Knight, N. Large, A. Goodman, P. Nordlander, and N. Halas, "Orienting nanoantennas in three dimensions to control light scattering across a dielectric interface," *Nano Letters*, vol. 13, no. 12, pp. 5997–6001, 2013.

[180] T. Carl, *Engineering Electromagnetic Fields and Waves.* New York: Wiley, 1988.

[181] T. White and K. Catchpole, "Plasmon-enhanced internal photoemission for photovoltaics: theoretical efficiency limits," *Applied Physics Letters*, vol. 101, no. 7, p. 073905, 2012.

[182] F. Barrere, P. Layrolle, C. Van Blitterswijk, and K. De Groot, "Biomimetic calcium phosphate coatings on Ti_6Al_4V: a crystal growth study of octacalcium phosphate and inhibition by Mg^{2+} and HCO^{3-}," *Bone*, vol. 25, no. 2, pp. 107S–111S, 1999.

[183] T. Voutsas, H. Nishiki, M. Atkinson, J. Hartzell, and Y. Nakata, "Sputtering technology of si films for low-temperature poly-si tfts," *SHARP Technical Journal*, vol. 80, pp. 36–42, 2001.

[184] J. Roth, *Industrial Plasma Engineering: Volume 2-Applications to Nonthermal Plasma Processing*, vol. 2. CRC press, 2001.

[185] P. Hargis Jr, K. Greenberg, P. Miller, J. Gerardo, J. Torczynski, M. Riley, G. Hebner, J. Roberts, J. Olthoff, J. Whetstone, *et al.*, "The gaseous electronics conference radio-frequency reference cell: A defined parallel-plate radio-frequency system for experimental and theoretical studies of plasma-processing discharges," *Review of Scientific Instruments*, vol. 65, no. 1, pp. 140–154, 1994.

[186] B. Jagannathan, W. Anderson, and J. Coleman, "Amorphous silicon/p-type crystalline silicon heterojunction solar cells," *Solar Energy Materials and Solar Cells*, vol. 46, no. 4, pp. 289–310, 1997.

[187] R. Perea Causín, "Hole-selective contacts by rf magnetron sputtering for silicon heterojunction solar cell structures," B.S. thesis, Universitat Politècnica de Catalunya, 2017.

[188] M. Donald and A. William, *Handbook of physical vapor deposition (PVD) processing.* Noyes Publications, USA, Westwood, NJ, 1998.

[189] D. Mattox, "Physical vapor deposition (pvd) processes," *Metal Finishing*, vol. 100, pp. 394–408, 2002.

[190] W. Kern, *Thin film processes II*, vol. 2. Academic press, 2012.

[191] T. Leigh, *Optical properties of metal nanoparticles and their influence on silicon solar cells.* PhD thesis, PhD thesis, University of Southamptom, 2009.

[192] M. Ohring, *Materials science of thin films.* Elsevier, 2001.

[193] J. Ziegler, M. Ziegler, and J. Biersack, "Srim–the stopping and range of ions in matter (2010)," *Nuclear Instruments and Methods in Physics Research Section B: Beam Interactions with Materials and Atoms*, vol. 268, no. 11-12, pp. 1818–1823, 2010.

[194] K. Katkhouda, G. Feistritzer, P. Buechel, and T. Geppert, "Overcoming the damage of passivation layers caused by dc-sputtered metals," in *Proc. 27th Eur. Photovolt. Sol. Energy Conf.*, pp. 1747–1750, 2012.

[195] C. Zhang, M. Meier, A. Lambertz, V. Smirnov, B. Holländer, A. Gordijn, and T. Merdzhanova, "Optical and electrical effects of p-type μc-$SiO_x : H$ in thin-film silicon solar cells on various front textures," *International Journal of Photoenergy*, vol. 2014, no. FZJ-2014-02831, pp. 1–10, 2014.

[196] T. Anderson, M. Faryad, T. Mackay, and A. Lakhtakia, "Towards numerical simulation of nonhomogeneous thin-film silicon solar cells," in *Physics, Simulation, and Photonic Engineering of Photovoltaic Devices III*, vol. 8981, p. 898115, International Society for Optics and Photonics, 2014.

[197] W. Pawlewicz, "Influence of deposition conditions on sputter-deposited amorphous silicon," *Journal of Applied Physics*, vol. 49, no. 11, pp. 5595–5601, 1978.

[198] E. Alkoy and P. Kelly, "The structure and properties of copper oxide and copper aluminium oxide coatings prepared by pulsed magnetron sputtering of powder targets," *Vacuum*, vol. 79, no. 3-4, pp. 221–230, 2005.

[199] K. Ranganathan, D. Wamwangi, and N. Coville, "Plasmonic ag nanoparticle interlayers for organic photovoltaic cells: An investigation of dielectric properties and light trapping," *Solar Energy*, vol. 118, pp. 256–266, 2015.

[200] N. Moonen and F. Diederich, "Limitations on the use of uv/vis spectroscopy for the evaluation of conjugation effectiveness," *Organic & Biomolecular Chemistry*, vol. 2, no. 16, pp. 2263–2266, 2004.

[201] M. Toney, J. Howard, J. Richer, G. Borges, J. Gordon, O. Melroy, D. Wiesler, D. Yee, and L. Sorensen, "Distribution of water molecules at Ag (111)/electrolyte interface as studied with surface $X-ray$ scattering," *Surface Science*, vol. 335, pp. 326–332, 1995.

[202] Ü. Özgür, Y. Alivov, C. Liu, A. Teke, M. Reshchikov, S. Doğan, V. Avrutin, S. Cho, and H. Morkoç, "A comprehensive review of ZnO materials and devices," *Journal of Applied Physics*, vol. 98, no. 4, p. 11, 2005.

[203] R. Narayanan, M. Deepa, A. Srivastava, and S. Shivaprasad, "Efficient plasmonic dye-sensitized solar cells with fluorescent au-encapsulated c-dots," *ChemPhysChem*, vol. 15, no. 6, pp. 1106–1115, 2014.

[204] N. Awang, M. Aziz, and A. Yusoff, "Preparation and characterization of single and binary metal oxide based on zinc oxide for solar cell application," *Solid State Science and Technology*, vol. 17, no. 2, pp. 103–115, 2009.

[205] A. Rogachev, A. Semchemko, V. Gaishun, E. Rusu, V. Ursaki, N. Curmei, and V. Zalamai, "Morphology, optical and luminescence properties of ZnO layers doped with Al or Ag and co-doped with rare earth ions," *Romanian Journal of Physics*, vol. 62, no. 9-10, 2017.

[206] F. Otieno, M. Airo, R. Erasmus, D. Billing, A. Quandt, and D. Wamwangi, "Effect of thermal treatment on $ZnO : Tb^{3+}$ nano-crystalline thin films and application for spectral conversion in inverted organic solar cells," *RSC Advances*, vol. 8, no. 51, pp. 29274–29282, 2018.

[207] F. Steudel, S. Loos, B. Ahrens, and S. Schweizer, "Trivalent rare-earth ions as photon down-shifter for photovoltaic applications," in *Photonics for Solar Energy Systems V*, vol. 9140, p. 91400I, International Society for Optics and Photonics, 2014.

[208] S. Ji, L. Yin, G. Liu, L. Zhang, and C. Ye, "Synthesis of rare earth ions-doped ZnO nanostructures with efficient host- guest energy transfer," *The Journal of Physical Chemistry C*, vol. 113, no. 37, pp. 16439–16444, 2009.

[209] A. Djurišić and Y. Leung, "Optical properties of zno nanostructures," *Small*, vol. 2, no. 8-9, pp. 944–961, 2006.

[210] M. Green, *Third generation photovoltaics.* Springer, 2006.

[211] D. Fisher, "Diffusion in silicon," *Trans Tech publications*, vol. 241, pp. p2–3, 2005.

[212] P. M. Fahey, P. Griffin, and J. Plummer, "Point defects and dopant diffusion in silicon," *Reviews of Modern Physics*, vol. 61, no. 2, p. 289, 1989.

[213] G. Harris, G. Kelner, and M. Shur, "9.1 ohmic contacts to sic," *Properties of Silicon Carbide*, no. 13, 1995.

[214] M. Feneberg, S. Osterburg, K. Lange, C. Lidig, B. Garke, R. Goldhahn, E. Richter, C. Netzel, M. Neumann, N. Esser, *et al.*, "Band gap renormalization and burstein-moss effect in silicon-and germanium-doped wurtzite gan up to 10 20 cm- 3," *Physical Review B*, vol. 90, no. 7, p. 075203, 2014.

[215] C. Nave, *The doping of semiconductors.* PhD thesis, Georgia State University. NP, 2012.

[216] E. A. Schiff, "Low-mobility solar cells: a device physics primer with application to amorphous silicon," *Solar Energy Materials and Solar Cells*, vol. 78, no. 1-4, pp. 567–595, 2003.

[217] P. Cheng, D. Li, and D. Yang, "Effect of rapid thermal processing on surface plasmon resonance of Ag island films," *Optoelectronics and Advanced Materials-Rapid Communications*, vol. 5, no. 3-4, pp. 455–458, 2011.

[218] S. Hong and X. Li, "Optimal size of gold nanoparticles for surface-enhanced raman spectroscopy under different conditions," *Journal of Nanomaterials*, vol. 2013, p. 49, 2013.

[219] A. Janotti and C. Van de Walle, "Fundamentals of zinc oxide as a semiconductor," *Reports on Progress in Physics*, vol. 72, no. 12, p. 126501, 2009.

[220] D. Lang, "Fast capacitance transient appartus: Application to ZnO and O centers in GaP p-n junctions," *Journal of Applied Physics*, vol. 45, no. 7, pp. 3014–3022, 1974.

[221] A. Apostolov, K. Grozdev, V. Shopov, and I. Velichkov, “Direct optical transitions in the transmission spectra of terbium films,” *Journal of Physics F: Metal Physics*, vol. 11, no. 11, p. L269, 1981.

[222] M. Pelton and G. Bryant, *Introduction to metal-nanoparticle plasmonics*, vol. 5. John Wiley & Sons, 2013.

[223] V. Kumar, F. Singh, O. Ntwaeaborwa, and H. Swart, “Effect of Br^{+6} ions on the structural, morphological and luminescent properties of ZnO/Si thin films,” *Applied Surface Science*, vol. 279, pp. 472–478, 2013.

[224] C. Tsai, D. Chuu, G. Chen, and S. Yang, “Studies of grain size effects in rf sputtered cds thin films,” *Journal of Applied Physics*, vol. 79, no. 12, pp. 9105–9109, 1996.

[225] M. De Jong, “Deposition of luminescent thin films for solar energy applications,” Master’s thesis, Technische Universiteit Delft in Netherlands, 2015.

[226] W. Yoon, K. Jung, J. Liu, T. Duraisamy, R. Revur, F. Teixeira, S. Sengupta, and P. Berger, “Plasmon-enhanced optical absorption and photocurrent in organic bulk heterojunction photovoltaic devices using self-assembled layer of silver nanoparticles,” *Solar Energy Materials and Solar Cells*, vol. 94, no. 2, pp. 128–132, 2010.